UC Berkeley
UC Berkeley Electronic Theses and Dissertations

Title

Spatiotemporal dynamics of carbon dioxide and methane fluxes from agricultural and restored wetlands in the California Delta

Permalink

https://escholarship.org/uc/item/8857w19f

Author

Hatala, Jaclyn

Publication Date

2013

Peer reviewed|Thesis/dissertation

eScholarship.org Powered by the California Digital Library
University of California

Spatiotemporal dynamics of carbon dioxide and methane fluxes from agricultural and restored wetlands in the California Delta

by

Jaclyn Anne Hatala

A dissertation submitted in partial satisfaction of the

requirements for the degree of

Doctor of Philosophy

in

Environmental Science, Policy, and Management

in the

Graduate Division

of the

University of California, Berkeley

Committee in charge:
Professor Dennis Baldocchi, Chair
Professor Whendee Silver
Professor Sally Thompson

Spring 2013

Spatiotemporal dynamics of carbon dioxide and methane fluxes from agricultural and restored wetlands in the California Delta

Copyright 2013

by

Jaclyn Anne Hatala

Abstract

Spatiotemporal dynamics of carbon dioxide and methane fluxes from agricultural and restored wetlands in the California Delta

by

Jaclyn Anne Hatala

Doctor of Philosophy in Environmental Science, Policy, and Management

University of California, Berkeley

Professor Dennis Baldocchi, Chair

The Sacramento-San Joaquin Delta in California was drained for agriculture and human settlement over a century ago, resulting in extreme rates of soil subsidence and release of CO_2 to the atmosphere from peat oxidation. Because of this century-long ecosystem carbon imbalance where heterotrophic respiration exceeded net primary productivity, most of the land surface in the Delta is now up to 8 meters below sea level. To potentially reverse this trend of chronic carbon loss from Delta ecosystems, land managers have begun converting drained lands back to flooded ecosystems, but at the cost of increased production of CH_4, a much more potent greenhouse gas than CO_2.

To evaluate the impacts of inundation on the biosphere-atmophere exchange of CO_2 and CH_4 in the Delta, I first measured and analyzed net fluxes of CO_2 and CH_4 for two continuous years with the eddy covariance technique in a drained peatland pasture and a recently re-flooded rice paddy. This analysis demonstrated that the drained pasture was a consistent large source of CO_2 and small source of CH_4, whereas the rice paddy was a mild sink for CO_2 and a mild source of CH_4. However more importantly, this first analysis revealed nuanced complexities for measuring and interpreting patterns in CO_2 and CH_4 fluxes through time and space.

CO_2 and CH_4 fluxes are inextricably linked in flooded ecosystems, as plant carbon serves as the primary substrate for the production of CH_4 and wetland plants also provide the primary transport pathway of CH_4 flux to the atmosphere. At the spatially homogeneous rice paddy during the summer growing season, I investigated rapid temporal coupling between CO_2 and CH_4 fluxes. Through wavelet Granger-causality analysis, I demonstrated that daily fluctuations in growing season gross

ecosystem productivity (photosynthesis) exert a stronger control than temperature on the diurnal pattern in CH_4 flux from rice.

At a spatially heterogeneous restored wetland site, I analyzed the spatial coupling between net CO_2 and CH_4 fluxes by characterizing two-dimensional patterns of emergent vegetation within eddy covariance flux footprints. I combined net CO_2 and CH_4 fluxes from three eddy flux towers with high-resolution remote sensing imagery classified for emergent vegetation and an analytical 2-D flux footprint model to assess the impact of vegetation fractal pattern and abundance on the measured flux. Both emergent vegetation abundance and fractal complexity are important metrics for constraining variability within CO_2 and CH_4 flux in this complex landscape.

Scaling between carbon flux measurements at individual sites and regional scales depends on the connection to remote sensing metrics that can be broadly applied. In the final chapter of this dissertation, I analyzed a long term dataset of hyperspectral ground reflectance measurements collected within the flux tower footprints of three structurally similar yet functionally diverse ecosystems: an annual grassland, a degraded pepperweed pasture, and a rice paddy. The normalized difference vegetation index (NDVI) was highly correlated with landscape-scale photosynthesis across all sites, however this work also revealed new potential spectral indices with high correlation to both net and partitioned CO_2 fluxes.

This analysis within this dissertation serves as a framework for considering the impacts of temporal and spatial heterogeneity on measured landscape-scale fluxes of CO_2 and CH_4. Scaling measurements through time and space is especially critical for interpreting fluxes of trace gases with a high degree of temporal heterogeneity, like CH_4 and N_2O, from landscapes that have a high degree of spatial heterogeneity, like wetlands. This work articulates a strong mechanistic connection between CO_2 and CH_4 fluxes in wetland ecosystems, and provides important management considerations for implementing and monitoring inundated land-use conversion as an effective carbon management strategy in the California Delta.

For E.H.(H.)M.

Table of Contents

List of Figures

List of Tables

Acknowledgements

I extend many thanks to Professor Dennis Baldocchi, my Ph.D. advisor, whose enthusiasm, creativity, and intelligence have been an inspiring force throughout the past four years. In particular, Dennis cultivated a productive and positive environment for research and collaboration in the Biomet lab. Within the Biomet lab, Joe Verfaillie deserves special recognition for his work and assistance. Not only was Joe essential for assembling and maintaining the instruments that collected nearly all of the data within this dissertation, but also through his patience and knack for explaining complex concepts I gained a wealth of knowledge about instrument programming and methodology. I am also very grateful for the many inspiring collaborations that I've had with my labmates in the Biomet lab, including Martin Beland, Matteo Detto, Melanie Hahn, Sara Knox, Hideki Kobayashi, Laurie Koteen, Siyan Ma, Oliver Sonnentag, Naama Raz-Yaseef, Ben Runkle, Youngryel Ryu (my inspiring big brother), Rodrigo Vargas, and Sebastian Wolf. And my Dissertation Committee members, Professor Whendee Silver and Professor Sally Thompson provided important advice and constructive feedback that improved the quality of this dissertation work.

I am thankful for the support and encouragement from my parents in pursuing my Ph.D. studies, and from my brother, also soon-to-be Dr. Hatala, for his emotional and intellectual support ever since the hours and days we'd spend searching the woods behind our house for new additions to our homely but extensive rock collection. Dr. Liz Moran, the first woman I ever met who had a Ph.D., was an especially strong inspiration to pursue environmental science after my particularly tough freshman year in college, and I am truly grateful for her mentorship. And to my best friend and in a few weeks, husband, Erich Matthes, I extend all the thanks in the universe for his limitless support, encouragement, good humor, and meticulous wordsmithing advice.

Lastly, I appreciate the support of the UC Berkeley Department of Environmental Science, Policy, and Management, particularly during my first year of the Ph.D. program, and thanks to the National Science Foundation Graduate Research Fellowship Program, which generously supported my Ph.D. studies and dissertation research from 2010-2013 through grant number DGE 1106400. Portions of this dissertation, with permission, have been reprinted from *Agriculture, Ecosystems, and Environment* and *Geophysical Research Letters*, and I thank the Elsevier and Wiley publishing companies for that permission.

Chapter 1: Introduction

'Land then, is not merely soil;
It is a fountain of energy flowing through a circuit of soils, plants, and animals.'
-- Aldo Leopold, *A Sand County Almanac* [1949]

Although invisible to the unaided eye, microorganisms in soil are the gatekeepers to the carbon balance of the Sacramento-San Joaquin Delta; they have the power to alter entire landscapes through their individually tiny, but collectively massive, metabolic rates. The balance between plant carbon uptake and microbial respiration governs long-term ecosystem carbon accumulation; if microbial respiration exceeds plant carbon uptake, the ecosystem is a net source of carbon to the atmosphere, but if plant carbon uptake outpaces microbial respiration the ecosystem is a net carbon sink. In flooded conditions, where the presence of water physically inhibits the diffusion of oxygen from the atmosphere to the soil, peat soil rich in plant organic matter accumulates since without oxygen, aerobic microorganisms cannot effectively decompose plant matter. This results in a long-term net carbon gain for the ecosystem. The tidal wetlands of the Sacramento-San Joaquin Delta in California began growing 6700 years ago as plant community expansion kept pace with sea level rise from the melting glaciers at the beginning of the Holocene and microbial respiration remained low under flooded conditions. After thousands of years of sea level rise, plant expansion, and resulting organic matter accumulation, the Sacramento-San Joaquin Delta developed a layer of peat soil up to 15 meters thick (Drexler et al. 2009a).

Wide-scale drainage of the Delta for agriculture at the end of the nineteenth century turned the most extensive stretch of wetlands on the Pacific coast into a series of islands with some of the most productive farmland in California. Today the islands are better described as saucers or bowls, where the rich organic matter in the exposed soil has been speedily consumed by aerobic microorganisms and respired back to the atmosphere as carbon dioxide over the past century. As a result of this persistent carbon imbalance where respiration exceeded carbon inputs by plants, the land surface in the Delta is now up to 8m below sea level (Drexler et al. 2009b).

Land managers now recognize that the continued practice of drained agriculture in the Delta is unsustainable and there is growing interest in converting drained lands

back to flooded conditions, into either agricultural wetlands like rice or restored wetlands. Like humans, most microorganisms that live in aerobic conditions consume plant-derived complex carbon molecules and respire carbon dioxide, which subsequently diffuses from the soil to the atmosphere. However, microbial respiration pathways in oxygen-depleted soils are more complicated. A wide range of microorganisms have evolved to utilize terminal electron acceptors other than oxygen to derive energy, and while most of these pathways still produce carbon dioxide as their metabolic end-product, a specialized group of microbes called methanogens respire methane rather than carbon dioxide. While converting lands back to flooded conditions helps to stem the loss of soil carbon as carbon dioxide, it also creates ideal conditions for the production of methane, a greenhouse gas 25 times more powerful than carbon dioxide on a 100-year timescale (Forster et al. 2007).

The second chapter of this dissertation evaluated the annual trade-offs between CO_2 uptake by plants, CO_2 release by ecosystem respiration, and net CH_4 emissions from methanogenic organisms in a drained peatland pasture and a flooded rice paddy recently converted from a corn field. The goal of this work was to analyze the carbon greenhouse gas trade-offs of land-use conversion from a drained pasture to a flooded rice paddy. To achieve this goal, I studied two years of simultaneous and direct measurements of landscape-scale CO_2 and CH_4 fluxes collected with eddy flux towers at the two sites. Through examining the seasonal and interannual patterns in CO_2 and CH_4 flux, I determined that ecosystem respiration consistently outpaced CO_2 uptake by photosynthesis at the drained peatland. This carbon imbalance made the site a large source of CO_2 the atmosphere but only a small CH_4 source due to drained conditions. At the rice paddy, CO_2 uptake by the high photosynthetic capacity of the rice plants exceeded ecosystem respiration, but the harvest of rice biomass at the end of the growing season prevented most of this carbon gain from abating soil subsidence. The rice paddy was also a relatively low source of CH_4 to the atmosphere in this study.

While this second chapter provided a baseline analysis of the net CO_2 and CH_4 from two key current and future ecosystems in the California Delta, it also highlighted important considerations of temporal and spatial heterogeneity in landscape-scale CO_2 and CH_4 fluxes that I investigated in the following three chapters. In the third chapter, I focused on temporal heterogeneity in the CO_2 and CH_4 fluxes at the spatially homogeneous rice paddy. Using time series analysis techniques of wavelet Granger-causality analysis, I tested the hypothesis that the diurnal pattern in gross ecosystem productivity stimulates a diurnal pattern in CH_4 flux. This work concluded that while gross ecosystem productivity is the most important short-term control on CH_4 flux to the atmosphere at the rice paddy, soil temperature is an important long-term control.

In the fourth chapter, I assessed the impact of spatial heterogeneity on measured CO_2 and CH_4 fluxes at a recently restored wetland site in the California Delta. The restored wetland was converted from a drained pasture by flooding in 2010, and since then has developed into a complex network of plant patches and open water surfaces. Over the course of the summer growing season in 2012, I measured CO_2 and CH_4 fluxes with eddy flux towers at three locations in the restored wetland. I used these flux data to drive a 2-D footprint model to determine the spatial origin of each measured flux, and then combined the modeled footprints with classified satellite imagery to calculate the fraction of emergent vegetation and fractal complexity of vegetation patches within each flux footprint. By analyzing these data over the course of the growing season, I was able to derive relationships with the daily maxima and minima of the CO_2 and CH_4 flux values. While the maximum CH_4 flux and minimum CO_2 flux (maximum CO_2 uptake) were well correlated with the fraction of emergent vegetation and fractal complexity of the footprint, the maximum CO_2 flux was better explained by variation in air temperature. This analysis shed light on important spatial considerations for engineering restored wetlands for maximal CO_2 uptake and minimal CH_4 release in the California Delta.

While eddy flux measurements can yield important insights into controls on CO_2 flux within and among sites, bridging to larger and more continuous spatial scales relies on connections between CO_2 flux and remotely sensed data. In the fifth chapter of this dissertation, I analyzed a long-term (2006-2012) dataset of near-surface hyperspectral reflectance measurements collected within the flux footprints of three structurally similar, yet functionally diverse California ecosystems: a semi-arid annual grassland, the drained peatland pasture, and the rice paddy. This analysis tested the ability of hyperspectral canopy reflectance to capture trends in net and partitioned CO_2 fluxes (ecosystem photosynthesis and respiration), as well as other important measures of productivity including leaf area index and foliar nitrogen content. This work confirmed that the commonly used normalized difference vegetation index (NDVI) well captured trends in ecosystem productivity and CO_2 uptake across all three sites. I also investigated the potential for new reflectance indices across the 400-900nm range that better captured variability in landscape-scale measures of ecosystem metabolism, and found good evidence for a reflectance index highly correlated with foliar nitrogen content across all three sites.

Measuring the net budgets of CO_2 and CH_4 flux at individual sites involves careful measurement and meticulous data analysis from eddy flux towers, but detangling controls on CO_2 flux and especially CH_4 flux from complex landscapes increasingly requires a suite of interdisciplinary tools. This dissertation works towards that goal by combing eddy flux measurements with novel time series and spatial

analysis techniques, environmental modeling, and satellite imagery analysis to better understand the connection between CO_2 and CH_4 fluxes in flooded ecosystems. The results of this dissertation have important management implications for land managers and policy makers considering inundated carbon management in the California Delta. However this work also highlights important challenges and new tools for the next generation of biometeorologists making novel continuous measurements of CH_4 from complex landscapes where fluxes are variable in both time and space. While this dissertation yields important management insights for the California Delta, it also provides a framework for temporal and spatial analysis that can help detangle variability in measured CH_4 fluxes from complex ecosystems.

Chapter 2: Greenhouse gas (CO_2, CH_4, H_2O) fluxes from drained and flooded agricultural peatlands in the Sacramento-San Joaquin Delta[1]

2.1 Abstract

The Sacramento-San Joaquin Delta in California was drained and converted to agriculture more than a century ago, and since then has experienced extreme rates of soil subsidence from peat oxidation. To reverse subsidence and capture carbon there is increasing interest in converting drained agricultural land-use types to flooded conditions. Rice agriculture is proposed as a flooded land-use type with CO_2 sequestration potential for this region. We conducted two years of simultaneous eddy covariance measurements at a conventional drained and grazed degraded peatland and a newly converted rice paddy to evaluate the impact of drained to flooded land-use change on CO_2, CH_4, and evaporation fluxes.

We found that the grazed degraded peatland emitted 175-299g-C $m^{-2}yr^{-1}$ as CO_2 and 3.3g-C $m^{-2}yr^{-1}$ as CH_4, while the rice paddy sequestered 84-283g-C $m^{-2}yr^{-1}$ of CO_2 from the atmosphere and released 2.5-6.6g-C $m^{-2}yr^{-1}$ as CH_4. The rice paddy evaporated 45-95% more water than the grazed degraded peatland. Annual net photosynthesis was similar between sites, but flooding at the rice paddy inhibited ecosystem respiration, making it a net CO_2 sink. The rice paddy had reduced rates of soil subsidence due to oxidation compared with the drained peatland, but did not completely reverse subsidence.

2.2 Introduction

Draining peatlands for agricultural cultivation results in some of the fastest rates and largest magnitudes of carbon loss attributable to land-use change. Nevertheless, peatland drainage is practiced around the world due to the high economic benefit of fertile soil. As a direct consequence of anthropogenic manipulation for agriculture and settlement, much of the land within the world's largest river deltas is sinking due to soil loss and compaction following drainage (Syvitski et al. 2009). Large river basins such as the Changjiang (China), Mississippi (USA), and Ganges-Brahmaputra (India,

[1] This chapter is reprinted, with permission, from the original journal article: Hatala, J. A., M. Detto, O. Sonnentag, S. J. Deverel, J. Verfaillie, D. D. Baldocchi. 2012. Greenhouse gas (CO_2, CH_4, H_2O) fluxes from drained and flooded agricultural peatlands in the Sacramento-San Joaquin Delta. *Agriculture, Ecosystems & Environment* 150: 1-18.

Bangladesh) are now identified as "natural recorders" of upstream land-use decisions (Bianchi and Allison 2009), as around the world the demand for agricultural production has made croplands and pastures one of the largest terrestrial biomes (Ramankutty et al. 2008). Land-use conversion from natural ecosystems to agricultural production has consequences for global biogeochemical cycling and climate through changes to carbon dynamics and the energy exchange between the land and atmosphere (Foley et al. 2005).

The Sacramento-San Joaquin Delta (hereafter, the Delta) in California is yet another example of a delta peatland that has undergone rapid environmental change, with irreversible alteration of the carbon cycle due to drainage, conversion to agriculture, and subsequently large rates of soil subsidence (Weir 1950, Armentano 1980, Deverel and Leighton 2010). The pre-reclamation Delta peatlands encompassed an area about 2,125 km^2 inland of San Francisco Bay (Thompson 1957) that existed as a network of saltwater and freshwater marshes for nearly 7000 years following the last Holocene glaciation (Shlemon and Begg 1975, Drexler et al. 2009a). High rates of primary productivity, low rates of decomposition, and gradual sea-level rise during the Delta's long period of inundation formed a layer of peat soil over 15m thick (Shlemon and Begg 1975, Drexler et al. 2007). However, the Delta islands were drained during the latter half of the 19^{th} century and beginning of the 20^{th} century, dramatically reversing the rate of carbon accumulation (Thompson 1957, Canuel et al. 2009). Drainage of the Delta created a network of "islands" that maintain an artificially low water table through an extensive and fragile 1700km levee system and continual island drainage (Mount and Twiss 2005). Agricultural cultivation since drainage has resulted in extreme rates of soil subsidence due to peat compaction and oxidation, and the land surface of Delta islands are now on average 5-8m below sea level (Drexler et al. 2009b, Deverel and Leighton 2010). The total amount of carbon lost from the Delta since drainage has been estimated at 0.5 petagrams of CO_2 (Crooks 2009), and Deverel and Leighton (2010) estimated that annual median CO_2 loss from Delta islands is about 17,000 g-C ha^{-1}.

Decreasing the rate of peat oxidation in the Delta is the key to slowing soil subsidence and turning drained Delta ecosystems from net carbon sources to sinks. Choosing management practices that preserve soil carbon, especially for non-growing season fluxes, has been shown to effectively decrease the net emission of CO_2 from agricultural ecosystems (Miller et al. 2000, Smith et al. 2007, Miller et al. 2008, Jans et al. 2010). The conversion from conventional drained agriculture to flooded systems like rice paddies has been identified as a potential management intervention for the Delta that could inhibit further peat oxidation (Lund et al. 2007). Miller et al. (2000) demonstrated that wetlands flooded from early spring through midsummer resulted in a net carbon gain. Rice growers use a similar water management practice, flooding rice

fields during the warmest months when soil oxidation rates, so rice is hypothesized to be a viable crop for stopping subsidence. The flooded status of rice paddy soils impedes peat oxidation by physically limiting the transport of oxygen into the soil profile, a requirement for most microbial metabolisms. Thus, rates of ecosystem respiration are significantly lower in rice paddies than in other agricultural systems (Eugster et al. 2010). Previous work has indicated that raising the water table in peat soils can significantly decrease CO_2 production and even reverse net ecosystem carbon loss (Hendriks et al. 2007, Waddington et al. 2010, Worrall et al. 2010).

However, managing land for CO_2 capture is likely to change the fluxes of other greenhouse gases from the ecosystem, in addition to altering the energy balance of the landscape (Pielke et al. 2002). While there is good evidence that flooding for rice will help to stop the net loss of CO_2 from peat oxidation, the conversion from drained to flooded soils creates ideal conditions for the anaerobic microbial production of CH_4, a greenhouse gas with 25 times the radiative forcing capacity of CO_2 over a 100-year time frame (Forster et al. 2007). In addition to potentially increasing CH_4 emissions, the conversion from drained to flooded conditions within the Delta's Mediterranean climate might also increase evaporation, as free standing water is more directly exposed to the atmosphere. Increased loss of water flowing through the Delta could create further tension within California's long-standing water wars, as the Delta is the nexus of drinking water distribution for 23 million Californians and nearly all the state's irrigation water (Schwarzenegger 2008). However, conversion of Delta islands to rice might limit future subsidence and reduce the rate of increasing levee fragility by reducing the hydraulic gradient from channels onto islands and stopping or reducing ever-increasing hydraulic forces on levees due to subsidence. To address the short-term consequences and trade-offs of conversion from drained to flooded agriculture on carbon, water, and energy exchange, this study examined differences in continuous CO_2 and CH_4 fluxes as well as the evaporation and the energy balance between a drained and grazed degraded peatland and a recently-converted flooded rice paddy in the Delta over two years (Figure 2.1).

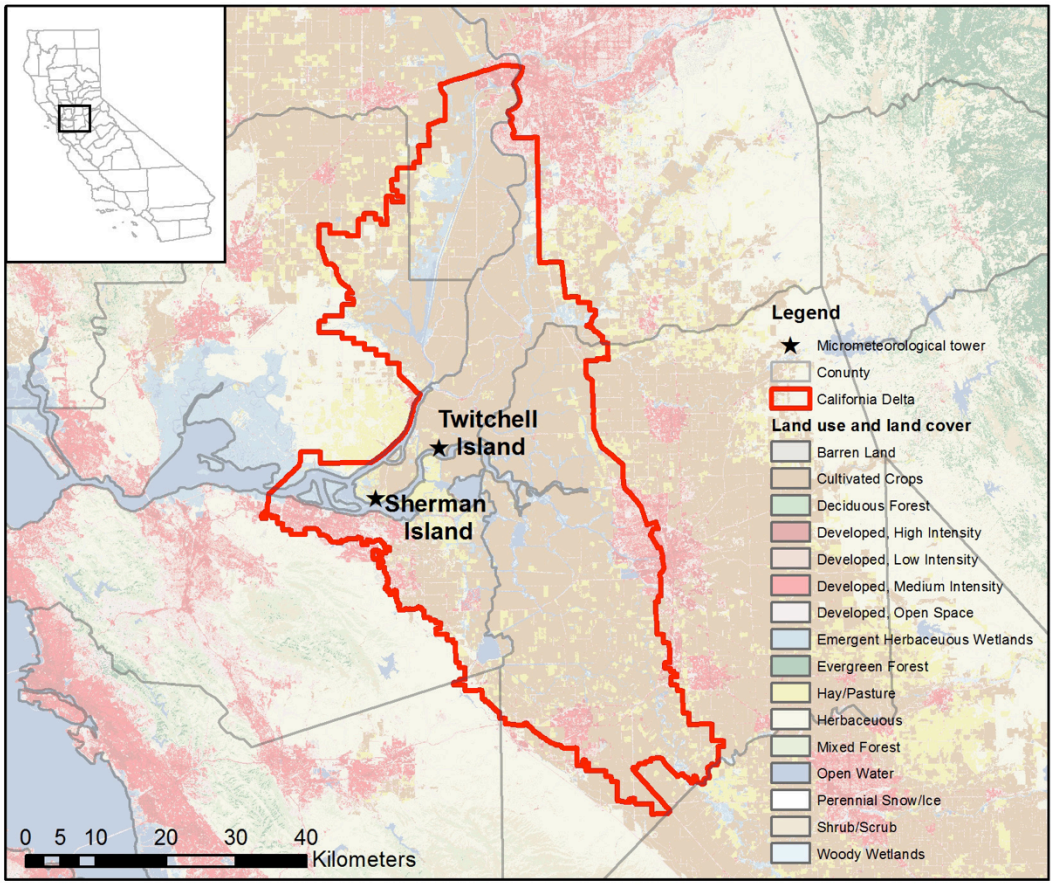

Source: National Land Cover Database 2001; UTM Zone 10, NAD 1983

Figure 2.1: Location of Delta Sites. The grazed degraded peatland and rice paddy are located in the Sacramento-San Joaquin Delta, inland of San Francisco Bay. Fluctuations in climate are nearly identical between sites, due to their close proximity (about 10km). Pasture and cultivated crops are the dominant land-use types within the extent of the Delta.

From April 2009 – April 2011, we measured the fluxes of CO_2, CH_4, H_2O, and energy at the drained and grazed degraded peatland and flooded rice paddy using the eddy covariance method (Baldocchi et al. 1988), and aggregated these fluxes over two years to calculate net annual budgets for April 2009-April 2010 and April 2010-April 2011. We measured the terrestrial carbon balance in the Delta as the net budgets of CO_2 (net ecosystem exchange; NEE) and CH_4 flux. CO_2 is captured by plants through photosynthesis (ecosystem photosynthesis; P_{eco}) and represents a sink from the atmosphere, and CO_2 is produced by plant and microbial respiration (ecosystem respiration; R_{eco}) and represents a source to the atmosphere. P_{eco} is expressed as negative and R_{eco} as positive, so that negative NEE respresents net CO_2 uptake and positive NEE represents net CO_2 release. CH_4 is produced as the metabolic end-product of a small group of *Archaea* that exist only in anaerobic conditions, such as flooded soils and ruminant digestive tracts, and this production acts as a source to the atmosphere (Conrad 2007). In vegetated rice paddies, most CH_4 is transported from the soil where it

is produced, through the porous aerenchyma tissue of rice plant to the atmosphere, and most methane is transported by diffusion and ebullition (bubbling) in during the winter months when the rice paddy is fallow (Holzapfel-Pschorn et al. 1986, Schutz et al. 1989b). At the grazed degraded peatland, CH_4 is produced within flooded drainage ditches and in zone of saturation in the soil profile (Teh et al. 2011). CH_4 is consumed in the aerobic zone in soils at both sites through the cosmopolitan metabolic pathway of a group of organisms called methanotrophs, which convert CH_4 into CO_2. Although methanotrophs are not a strong sink of atmospheric CH_4, they can consume 48-78% of methane produced at lower depths in upland soils (Teh et al. 2005) and 20-60% of CH_4 produced in rice paddy soils (Tyler et al. 1997) as CH_4 diffuses from the anaerobic zone where it is produced upward through the soil and water profile. The method used to partition NEE into sinks by ecosystem photosynthesis (P_{eco}) and sources through ecosystem respiration (R_{eco}) cannot likewise partition soil CH_4 fluxes into CH_4 production (methanogenesis) and CH_4 consumption (methanotrophy).

The first goal in our analysis was to compare carbon capture in the rice paddy with the drained grazed peatland on an annual timescale. We hypothesized that the grazed degraded peatland would be a larger net source of carbon than the rice paddy, as we expected the drained peat soil at the grazed peatland to have higher rates of R_{eco} and lower rates of P_{eco} than the flooded and productive rice paddy. We also considered the measured CH_4 emissions from each site as carbon losses for this net carbon balance calculation, and excepted CH_4 flux from the rice paddy to exceed that from the drained and grazed peatland since the CH_4 produced in the drained soil has a much larger opportunity to be oxidized by microbes into CO_2 as it diffuses through the aerated soil zone to the atmosphere. As we expected the drained peatland to be a larger source of carbon from the ecosystem, we hypothesized that it would have larger rates of subsidence due to soil oxidation than the flooded rice paddy.

Our second goal was to quantify the effects of land-use conversion from drained to flooded soils on the CH_4 budget since it has a higher radiative forcing than CO_2, which can alter the greenhouse gas radiative forcing budget of the ecosystem. Since the flooded paddy soil creates ideal anaerobic conditions for CH_4 production and incorporates fresh biomass into the soil each year through the residual straw left on the field after harvest, we expected the net budget of CH_4 at the rice paddy to exceed that of the grazed degraded peatland (Cicerone et al. 1992). Using the CO_2-equilvalent conversion factor for CH_4 of 25, the hypothesized higher rate of CH_4 production at the rice paddy could transform the ecosystem into a net positive greenhouse gas forcing budget even though it might be a net sink for CO_2 (Forster et al. 2007).

The final goal of our work was to analyze differences between the evaporation

budgets at the two sites. We expected that evaporation would be higher at the rice paddy than the grazed degraded peatland since the water surface at the rice paddy is directly exposed to the atmosphere for much of the year. However, we considered that it was possible that evaporation from the grass canopy and shallow water table at the grazed degraded peatland during the winter might exceed that from the fallow but flooded rice paddy due to the higher canopy conductance of rough vegetation when compared with a flat water surface. Together, these hypotheses provide important information about the short-term impacts and significant environmental trade-offs of land-use change from drained to flooded ecosystems in the Delta on greenhouse gas, water, and energy exchange. Quantifying the magnitude and pattern of CO_2, CH_4, water, and energy fluxes from these two agricultural land-use types is essential for understanding the impacts of drained to flooded land-use conversion in the Delta. Through this framework, we evaluated the ability of the rice paddy to act as a land management opportunity for creating a sustainable Delta where farmers can maintain their livelihoods and transform Delta agriculture from a net carbon source to a carbon sink and stop subsidence. In addition to providing fundamental information about greenhouse gas fluxes in the Delta, this analysis also provides the data and metrics necessary to lay the groundwork for greenhouse gas accounting protocols and verification.

2.3 Methods

2.3.1 Study sites

Our two study sites are a drained and grazed degraded peatland on Sherman Island, CA (latitude: 38.0367°N; longitude: 121.7540°W; elevation: 4m below sea level) and a rice paddy on Twitchell Island, CA (latitude: 38.1087°N, longitude: 121.6530°W; elevation: 4.5m below sea level) (Figure 2.1). Both sites are within the Sacramento-San Joaquin Delta approximately 100km inland from the Pacific Ocean and they experience a Mediterranean climate, with hot, dry summers, and cool, wet winters. At the Anitoch climate station (10km southwest of Sherman Island) the 50-year mean air temperature (1949-1999) is 15.1°C and the mean annual precipitation is 335mm. The water table at the grazed degraded peatland is regulated to 50-80cm below the surface for the entire year. The water level at the rice paddy is maintained about 5-10cm above the soil surface for most of the year, but it is drained twice annually: about 45 days before the start of the growing season for cultivation and planting, and for about 55 days at the end of the growing season for harvest.

The Sherman Island grazed degraded peatland site is covered by two invasive

plants: mouse barley (*Hordeum murinum* L.) a C_3 grass that dominates the canopy December-April, and pepperweed (*Lepidium latifolium* L.) a perennial plant that dominates the canopy April-October. The effects of management decisions on plant canopy dynamics and carbon fluxes at the Sherman Island grazed degraded peatland during 2007-2009 are discussed at length in Sonnentag *et al.* (2011a). The grazed degraded peatland (~0.9km × ~0.4km) is fenced and grazed year-round by approximately 100 cattle (about 1.1 animal/acre), which has been the typical land use at the site for at least the past 20 years. During the summer months, the cattle aggregate in the far end of the field opposite the eddy covariance tower during the day, but the cattle pass by the tower frequently at evening and during winter months. Consequently, their presence can have a large impact on the methane and to a lesser extent, carbon dioxide, fluxes at the site (Detto et al. 2010, Baldocchi et al. 2012).

The Twitchell Island rice paddy is a pilot project administered by the California Department of Water Resources (CADWR). The land was converted from traditional corn and alfalfa agriculture to rice (*Oryza sativa*) in 2009 to assess the feasibility of growing rice in the Delta. Before 1990, rice was not farmed in the Delta. Since then, development of new varietals that can withstand the cool nighttime growing season temperatures has made rice agriculture feasible in this region. Currently there are about 2000 hectares of rice farmed in the Delta. The field where the eddy covariance tower is located is approximately 0.55km x 0.7km. The rice variety M104 (a cold-weather cultivar) was planted April 15 in 2009, and M206 (also a cold weather cultivar) was planted on April 16 in 2010. Rice was harvested October 22-25 in 2009 and October 28-29 in 2010. The field was fertilized with 30-0-20 ammonium sulfate fertilizer on May 27-28 in 2009, and on June 5-7 in 2010 at a rate of 68kg/acre. In both 2009 and 2010 before planting, the drained rice fields were treated with herbicide (1.5mg/L Bispyribac sodium and 2.5mg/L Pendimethalin) and in 2010 the rice paddy was treated with additional herbicide the first week in June (3.65g/acre Regiment, 324g/acre Prowl, 32g/acre SYL-TAC, 324g/acre UN-32, and 4.1g/acre Sandea) to remove a weed infestation that preceded rice growth. After harvest of the rice grains, the remaining plant residue was left on top of the soil in both 2009 and 2010, and the field was re-flooded for the winter months to provide habitat for migrating birds. During the flooded winter months, no plants grew within the field.

Each site is situated on degraded peat soil where the top-most layer is silt loam, overlaying a deep peat layer. At each site, we calculated soil bulk density gravimetrically by collecting samples within an aluminum collar (5cm tall by 5cm in diameter) at depths from 0-75cm within the soil profile, drying, and then weighing each sample. After measurement for bulk density, we measured the percent carbon content and the carbon to nitrogen ratio of each sample by grinding the dried soil samples and

analyzing them on a Shimadzu Elemental Analyzer. Soil parameters for both sites are outlined in Table 1. At both sites, the bulk density of the upper layer is higher and the carbon content is lower than the deeper soils layers, which generally contain more undegraded peat soil.

Site	Layer (cm below surface)	Soil type	Bulk density (g/cm^3)	Carbon content (%)	C:N
Grazed peatland	0-60	Degraded peat silt loam	1.08	7.5	13.9
Grazed peatland	60-75	Partially undegraded peat silt loam	0.95	15	15.6
Rice paddy	0-30	Tilled degraded peat silt loam	0.65	15	14.1
Rice paddy	30-45	Untilled partially undegraded peat silt loam	0.57	31	15.6

Table 2.1 Soil properties in the pasture and rice paddy. Soil properties were measured at each field site. At both sites, the top layer has a higher bulk density and lower carbon content than the deeper layer, which contains partially undegraded peat soils. The soil parameters at the rice paddy were measured after one year of rice cultivation in the springtime while the field was drained, but before the field was planted or fertilized.

2.3.2 Micrometeorological measurements

Micrometeorological instruments were deployed at each site to accompany flux measurements made by the eddy covariance instruments. At each site, air temperature and relative humidity were measured with an aspirated and shielded thermistor and capacitance sensor (HMP45C; Vaisala, Vantaa, Finland). Precipitation was measured at both sites with a tipping rain bucket (TE525; Texas Electronics Inc., Dallas, TX, USA) and water table depth was measured with a pressure transducer (PDCR 1830; GE Druck, Billerica, MA, USA) located within a well at each site. Soil temperatures were measured at 2, 4, 8, 16, and 32cm below the surface in three replicate profiles at each site with copper constantan thermocouples and the average of the three replicates at each

depth was computed and used for analysis.

Net radiation (R_{net}) was measured at the grazed degraded peatland with a four-component net radiometer (CNR1; Kipp and Zonen, Delft, Netherlands) on a 2m boom from the tower oriented toward the south. R_{net} at the rice paddy was measured with a two-component net radiometer (NRLite; Kipp and Zonen, Delft, Netherlands) on a 6m boom oriented to the west. At both sites, incoming and outgoing photosynthetically active radiation was measured with quantum sensors as photosynthetic photon flux density (PAR-LITE; Kipp and Zonen, Delft, Netherlands). Ground heat flux was recorded by three replicate ground heat flux plates (HFP01; Huskeflux Thermal Sensors, Delft, Netherlands) buried 1cm under the soil surface, and the average of the three replicates was used for analysis. All micrometeorological measurements were sampled every 5 seconds, and the 30 minute mean values were stored on a CR10X datalogger (Campbell Scientific, Logan, UT, USA) at each site.

2.3.3 Eddy covariance measurements

The fluxes of CO_2, CH_4, H_2O, and energy were measured at each site with the eddy covariance (EC) method (Baldocchi et al. 1988). Briefly, the EC method calculates fluxes of a scalar of interest (for example, CO_2) by simultaneously measuring turbulent fluctuations in vertical wind and the scalar, and then computing the covariance between the two. We measured the covariance between turbulence and the scalar at 10Hz intervals (every 0.1 seconds), and then computed fluxes as the average of the 10Hz covariances over a thirty minute interval. This sampling rate and averaging interval allowed for a 5Hz cut-off for the cospectra between turbulence and the scalar of interest, which was determined to be adequate for accurate eddy covariance measurements at these sites (Detto et al. 2011). The EC instrumentation used to calculate fluxes was mounted on a tower 3.15m high at the grazed degraded peatland and on a tower 3.05m high at the rice paddy. The prevailing wind direction at both sites is strongly from the west, as the sites are located within an inverted delta landform where winds from the Pacific Ocean are forced to travel inland through the Carquinez Strait, a narrow gap in the mountains of California's Coastal Range.

An almost identical set of EC instrumentation was deployed at each site. Each tower measured fluctuations in longitudinal, lateral, and horizontal wind directions (u, v, w; m/s) and the speed of sound with a sonic anemometer (Gill WindMaster Pro; Gill Instruments Ltd, Lymington, Hampshire, England). Fluctuations in CO_2 and H_2O density (ϱ_{CO2}, ϱ_{H2O}) were measured with an open-path infrared gas analyzer (LI-7500; LI-COR Biogeosciences, Lincoln NE, USA) and fluctuations in CH4 density (ϱ_{CH4}) were measured with a closed-path, tunable diode laser fast methane sensor (FMA, Los Gatos Research, CA, USA). The sonic anemometer readings and ϱ_{CO2}, ϱ_{H2O}, and ϱ_{CH4} densities

were recorded at each site at 10Hz intervals with a Campbell CR1000 datalogger (Campbell Scientific, Logan, UT, USA).

The FMA sensor requires an external pump to operate. At the grazed degraded peatland site, which had access to an AC power line, we deployed a scroll pump (BOC ESDP 30A, Edwards, Tewksbury, MA, USA) requiring 770 W of power and providing a flow rate of about 40 L min^{-1} at the FMA cell pressure (19kPa). At the rice paddy, which requires a generator for electrical production, we deployed a diaphragm pump (N940.5APE-B, KNF Neuberger, Trenton, NJ, USA) requiring 240W operating at 12 L min^{-1} at the FMA cell pressure in order to reduce power consumption. Extensive field testing was conducted to evaluate the performance of the FMA sensor at both sites (Detto et al. 2010).

Using standard eddy covariance techniques, we analyzed the 10Hz data recorded for u, v, w, T_{sonic}, ϱ_{CO2}, ϱ_{H2O} and ϱ_{CH4} to calculate half-hourly fluxes of sensible heat (H; W m^{-2}), CO_2 (NEE; μmol m^{-2} s^{-1}), H_2O (evaporation, latent energy (LE); mm m^{-2} s^{-1}) and CH_4 (nmol m^{-2} s^{-1}) after applying a series of corrections using in-house software (Detto et al. 2010). In this software, the first data filter removed artificial spikes (values greater than six standard deviations of the mean within a one-minute window) and diagnostic instrument values that corresponded with bad readings, which were mostly correlated with rain or fog events. For each half-hour block of 10Hz values that passed the first data filter, a coordinate rotation was applied to align the x-axis of the sonic anemometer to the mean wind direction by aligning the mean vertical and lateral velocities to zero. Within each half-hour block of fluxes, air density fluctuations effects were removed by the Webb-Pearman-Leuning correction (Webb et al. 1980, Detto and Katul 2007). Fluctuations in T_{sonic} were calculated from fluctuations in the speed of sound after correction for crosswind and humidity effects (Schotanus et al. 1983, Kaimal and Gaynor 1991). After applying the coordinate rotation and correcting for density fluctuations, we applied cospectral corrections following methods developed within Detto *et al*. (2011). The cospectral corrections are performed on the closed-path CH_4 fluxes to account for tube attenuation, the residence time in the cell, as well as sensor separation for CH_4, CO_2, and H_2O fluxes (Detto et al. 2011). After computing the fluxes, we filtered flux values with anomalously high and low friction velocity (u_*>1.2m/s and $|\overline{uw}|$<0.02) to constrain our analysis to periods where the air near the sensors was well-mixed, which removed 6% of possible 30-minute rice fluxes in 2009-2010 and 7% in 2010-2011 and 9% of possible 30-minute drained degraded pasture fluxes in 2009-2010 and 8% of drained degraded pasture fluxes in 2010-2011.

We assessed the random instrumental noise in each half-hour flux value using a bootstrapping technique. The bootstrap technique evaluated the covariance between w

and the scalar of interest (T_{sonic}, ϱ_{CO2}, ϱ_{H2O} or ϱ_{CH4}) on 100 bootstrapped samples taken with replacement from the actual distribution of 10Hz values for w and the scalar for each half-hour. We then computed the standard deviation of calculated fluxes across the bootstrapped covariances. Resulting fluxes from wind directions outside of the footprint of the target land-use type (160-210° for both the grazed degraded peatland and the rice paddy) were filtered from the dataset and excluded from this analysis.

At the Sherman Island grazed degraded peatland, we conducted extra processing using higher-order statistics to filter out half-hour CO_2 and CH_4 fluxes when the cattle were in the footprint of the EC tower, as their presence dramatically alters the fluxes of CH_4, and to a lesser extent, CO_2 (Detto et al. 2010, Baldocchi et al. 2012). Since cattle emit amounts of CH_4 that are orders of magnitude higher than the average soil flux at the drained grazed degraded peatland, their presence impacts the half-hour flux interval by creating a probability distribution function of 10Hz ϱ_{CH4} values that is markedly different from that of the background soil flux. The presence of cattle in the flux footprint creates a probability distribution of ϱ_{CH4} and ϱ_{CO2} that is skewed (3rd order statistical moment) and more outlier-prone (kurtosis, 4th order statistical moment) than the background ecosystem values. Furthermore, cattle leaving or entering the flux footprint is expected to create first and second-order unstationarity within the half-hour interval, which means that the mean ϱ_{CH4} and its variance are not constant throughout the half-hour interval, but instead trends upward or downward with the movement of cattle. Since skewness of the normal distribution is zero, kurtosis of the normal is 3, and stationarity requires that the deviation from the long-term mean at a lagged point is zero, we can define periods when cows are likely within the field by the following criteria:

$$1. \quad \left|Skewness(\overline{w'\rho'_{CH4}})\right| > 3$$

$$2. \quad Kurtosis(\overline{w'\rho'_{CH4}}) > 10$$

$$3. \quad \left|1 - \frac{\overline{(w'\rho'_{CH4})_{15min}}}{\overline{(w'\rho'_{CH4})}}\right| > 10$$

where $(w'\rho'_{CH4})$ is the covariance between the 10Hz values of w and ϱ_{CH4}, and in the third criterion, $\overline{(w'\rho'_{CH4})_{15min}}$ is the mean covariance between w and ϱ_{CH4} over a 15-minute time interval and $\overline{(w'\rho'_{CH4})}$ is the mean covariance over the entire half-hour interval. We adopted the same filtering criteria to the ϱ_{CO2} data to also remove periods heavily influenced by cattle at the drained peatland. We evaluated the accuracy of this statistical classification of fluxes at the grazed degraded peatland by comparing them to digital images of the tower footprint. A webcam (DCS-900; D-Link Corporation, Taipei, Taiwan) was installed on the EC tower, and a digital photograph was taken every half

hour during daylight, at a lag that corresponded to the middle of the half hour interval used in the eddy covariance processing (Baldocchi et al. 2012). In 2009-2010 at the degraded pasture 21% of possible 30-minute fluxes were removed from the analysis by the cattle filter and 17% of possible fluxes were removed in the 2010-2011 year. Through this analysis it was determined that this statistical filter accurately eliminated fluxes heavily impacted by cattle metabolism.

2.3.4 Gap-filling, CO_2 partitioning, & integrating annual budgets

Using the half-hourly fluxes derived from eddy covariance, we computed the net annual budgets for evaporation, NEE, CH_4, and partitioned ecosystem photosynthesis (CO_2 uptake; P_{eco}) and ecosystem respiration (CO_2 release; R_{eco}) by gap-filling and subsequent integration. To gap-fill missing half-hourly fluxes, we used the artificial neural network (ANN) technique standardized within the international Fluxnet project, with meteorological variables driving the fitting (Papale and Valentini 2003, Papale et al. 2006). While this technique has been used extensively for gap-filling H_2O and CO_2 fluxes, the ANN technique has not been applied to CH_4 fluxes, likely due to the limited studies of CH_4 fluxes using the eddy covariance technique (although Rinne *et al*. (2007) gap-filled an annual CH_4 budgets using meteorological drivers). For the purposes of this study, we only gap-filled the non-cow CH_4 flux for the grazed degraded peatland site, whereas at the rice paddy we gap-filled all data. At the drained degraded pasture gap-filled data comprised 38% of the 2009-2011 dataset and 32% of the 2010-2011 dataset, and at the rice paddy gap-filled data are 21% of the 2009-2010 dataset and 18% of the 2010-2011 dataset. These percentages represent data lost by all causes, including instrument malfunction and removal by data processing previously described, and the removal of cattle fluxes from the drained degraded pasture dataset explains the larger percentage of gap-filled values at this site compared with the rice paddy.

Winds are strong even during the nighttime at both sites, eliminating the need to account for uncertainties typically related to nighttime eddy covariance measurements due to nighttime atmospheric stratification and stability (Massman and Lee 2002). To partition NEE into ecosystem photosynthesis (P_{eco}) and ecosystem respiration (R_{eco}), we applied the partitioning technique of Reichstein *et al.*, 2005 to the ANN gap-filled NEE values. This method partitions NEE by extrapolating nighttime CO_2 flux as respiration using a short-term temperature response over 2 weeks using the temperature response function of Lloyd and Taylor, 1994 (Reichstein et al. 2005). By calculating the temperature response function on short timescales, this method accounts for seasonal changes in the temperature response due to confounding factors like substrate availability. This partitioning algorithm yielded results that followed an intuitive annual pattern for both sites, but we also investigated alternative partitioning

algorithms to ensure that the Reichstein *et al*. (2005) method was the best choice for our data. We closely investigated the nighttime NEE data from both sites for patterns that would indicate a better partitioning of R_{eco} from the early evening maximum NEE method presented in van Gorsel *et al*. (2009) . However, we were unable to justify the use of this method due to the relatively well-mixed nighttime conditions at the site and resulting lack of canopy storage of CO_2.

To compute annual sums, we integrated the gap-filled (and in the case of NEE, partitioned) fluxes from the ANN method over the course of each year within this study. We integrated the annual sums at the start of the rice growing season, from 25 April 2009 – 24 April 2010 as the first year, and 25 April 2010 – 24 April 2011 as the second year of the study. By using a bootstrapping procedure, we determined the amount of uncertainty in the ANN gap-filling procedure for the annual fluxes of each scalar (LE, NEE, P_{eco}, R_{eco}, and CH_4) (Hagen et al. 2006). We chose 1000 bootstrapped samples with replacement from the annual distribution of non-gap-filled half-hour fluxes of each scalar, and then gap-filled the bootstrapped samples. After gap-filling the bootstrapped samples we computed the integrated annual budget for each gap-filled bootstrapped annual dataset, and we calculated the 95% confidence interval from the distribution of the 1000 bootstrapped annual budgets. We calculated the annual potential evaporation (LE_{pot}) at each site based on the Penman equation (Penman 1948) as in Shuttleworth (2007) from our measurements of R_{net}, wind speed, vapor pressure deficit, and air temperature.

2.3.5 Vegetation sampling methods

Plant area index (PAI) was measured every 1-2 weeks at the grazed degraded peatland and the rice paddy during the growing season by both destructive (direct) and nondestructive (indirect) measurements. We call our measurements PAI rather than leaf area index because at both sites we did not separate leaves from other plant matter. We measured PAI every 2-4 weeks over the winter at the grazed degraded peatland by direct measurement only, due to the short stature of winter grasses at the site. Destructive PAI measurements were conducted at each site by clipping all aboveground biomass within five randomly sampled 400cm^2 plots. We then measured the area of each sample using an optical area scanner (LI-3100 area analyzer; LI-COR Biogeosciences, Lincoln NE, USA). Using these areas, we calculated PAI as area of all standing biomass within each plot divided by the area of the plot (400cm^2). Indirect PAI measurements were made with the LAI-2000 Plant Canopy Analyzer (LI-COR) during months when the height of vegetation was greater than 0.5m. PAI measurements with the LAI-2000 were made every 10m along a 100m transect extending west into the predominant wind direction at the rice paddy, and every 10m along a 200m transect

extending in the east-west direction at the grazed degraded peatland site according to the protocol in Sonnentag *et al*. (2011a) .

2.4 Results

2.4.1 Micrometeorology & the energy balance

Trends in meteorological variables at the two sites follow a strong seasonal cycle as a result of the distinct Mediterranean climate within the Delta (Figure 2.2). Mean air temperatures for May 2009 – April 2010 were 15.0°C at the grazed degraded peatland and 14.2°C at the rice paddy, and for May 2010 – April 2011 mean air temperatures were 14.8°C at the grazed degraded peatland and 13.9°C at the rice paddy, not far from the 50-year (1949-1999) mean of 15.1°C from the Antioch Climate Station 10km from the grazed degraded peatland site (Table 2.2). Total precipitation was 438mm for May 09 – April 10 and 404mm for May 10 – April 11, slightly greater than the 50-year mean of 335mm, and total incoming radiation was 6878MJ m^{-2} yr^{-1} from May 2009 – April 2010 and 6934MJ m^{-2} yr^{-1} from May 2010 – April 2011. When the rice canopy is closed (PAI > 2) and the rice paddy is flooded (15 July to 1 October), the soil is shaded by the dense rice canopy, soil temperatures ($T_{s,grow}$) are on average 3.5-4.5°C lower than the grazed degraded peatland soils (Table 2.2). Such a decrease in soil temperature may help to diminish heterotrophic respiration during the rice growing season, and thus help diminish peat oxidation, as Deverel and Rojstaczer (1996) showed significant correlations of log of carbon dioxides fluxes with soil temperature for chamber measurements on three Delta islands. Our results indicate that generally, there are only very small differences between the two sites with respect to basic meteorological drivers of ecosystem form and function. However, these two land-use types fundamentally differ in the way that they utilize the available incoming energy by mechanisms that correspond to differences in their vegetation cover and water management.

Site	Year	T_{air} (C)	T_s (C)	$T_{s,grow}$ (C)	R_g (MJ $m^{-2}yr^{-1}$)	R_{net} (MJ $m^{-2}yr^{-1}$)	H (MJ $m^{-2}yr^{-1}$)	LE (MJ $m^{-2}yr^{-1}$)	LE_{pot}[a] (MJ $m^{-2}yr^{-1}$)
Grazed degraded peatland	2009-2010	**15.0**	**16.5**	**22.8**	**6878**	**2998**	**764** (734-794)	**1507** (1477-1538)	**2886** (α[b] = 0.71)
	2010-2011	**14.8**	**16.3**	**21.7**	**6934**	**3027**	**589** (560-624)	**1858** (1819-1896)	**2950** (α = 0.88)
Rice paddy	2009-2010	**14.2**	**15.6**	**18.2**	**6878**	**3354**	**138** (105-180)	**2960** (2888-3024)	**2916** (α = 1.24)
	2010-2011	**13.9**	**15.3**	**18.4**	**6934**	**2977**	**211** (185-240)	**2724** (2663-2791)	**3021** (α = 1.25)

[a] Potential evaporation (LE_{pot}) is calculated by the Penman equation after (Shuttleworth 2007).

[b] $\alpha = LE/LE_{eq}$ where LE_{eq} is equilibrium evaporation, and is equal to $(R_{net}-G)(s/(s+\gamma))$.

Table 2.2 Meteorological drivers and energy balance. This table outlines the mean air temperatures (T_{air}), soil temperatures at 2cm depth (T_s), and growing season soil temperatures at 2cm depth ($T_{s,grow}$) for each site and year in this study. The radiation budgets for each site in each year are also presented for total incoming radiation (R_g), net radiation (R_{net}), sensible heat exchange (H), and latent heat exchange (LE), with the bootstrapped 95% confidence intervals for the gap-filling procedure in the parentheses. While both sites receive the same amount of incoming and net radiation due to their spatial proximity, the way that the two land-use types partition the budget of R_{net} is markedly different.

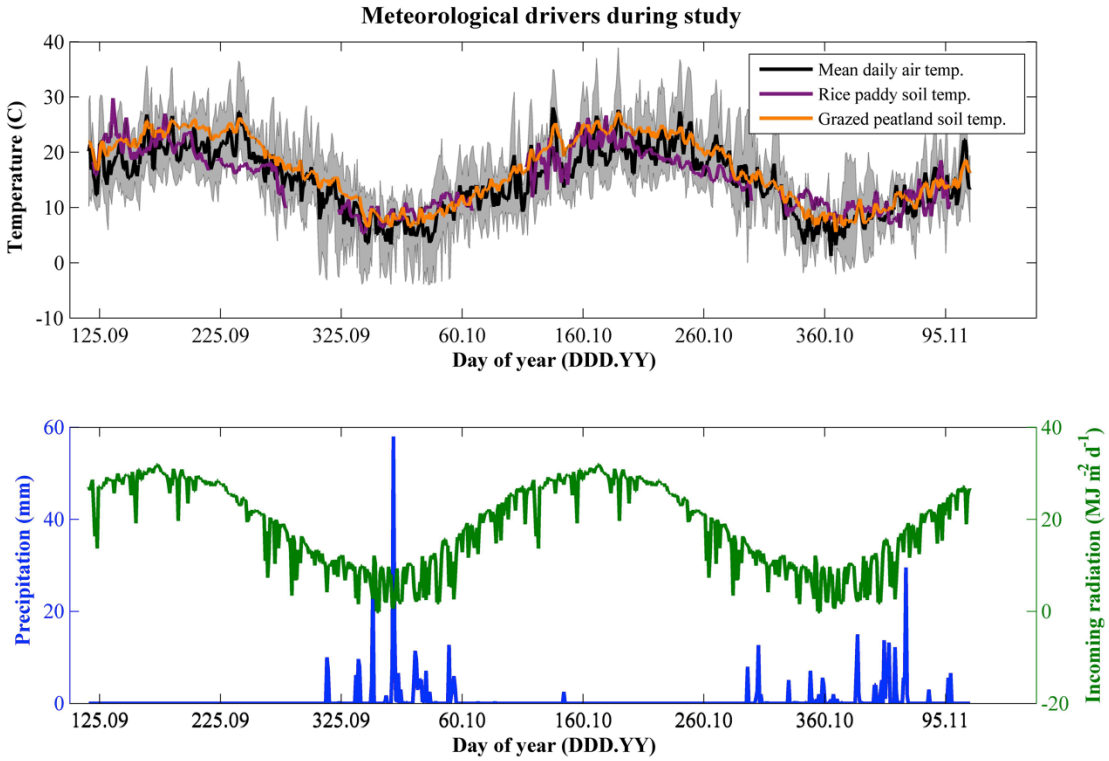

Figure 2.2 Meteorological drivers during study. The top panel shows the mean daily air temperature and soil temperatures at 2cm depth for each site, where the gray shaded area bounds the minimum and maximum daily air temperature. Air temperature is only plotted for the grazed degraded peatland since values for the rice paddy were nearly identical. The flooded status of the rice paddy during the summer months creates a lower average soil temperature than the drained and grazed degraded peatland. The bottom panel demonstrates the typical pattern of a Mediterranean climate at these sites, with high incoming solar radiation and very little rainfall during the summer months, and wet, cool winters.

While the annual net radiation (R_{net}) is similar between the two sites (Table 2), differences in the water management (drained versus flooded) as well as the canopy cover (Figure 2.3) drive differences in the way the energy balance is distributed between sensible and latent heat exchange. As is evident in Figure 2.3, the PAI at the rice paddy demonstrates a short pattern of vegetative growth with low interannual variability due to the crop cycle, whereas the PAI at the grazed degraded peatland is much more variable, both between and within sampling dates, due to the complex phenology of pepperweed (Sonnentag et al. 2011b). While the rice paddy has a short but intense period of vegetation for a small part of the year, the grazed degraded peatland demonstrates vegetative growth throughout the year, which changes meteorological variables connected to the canopy structure.

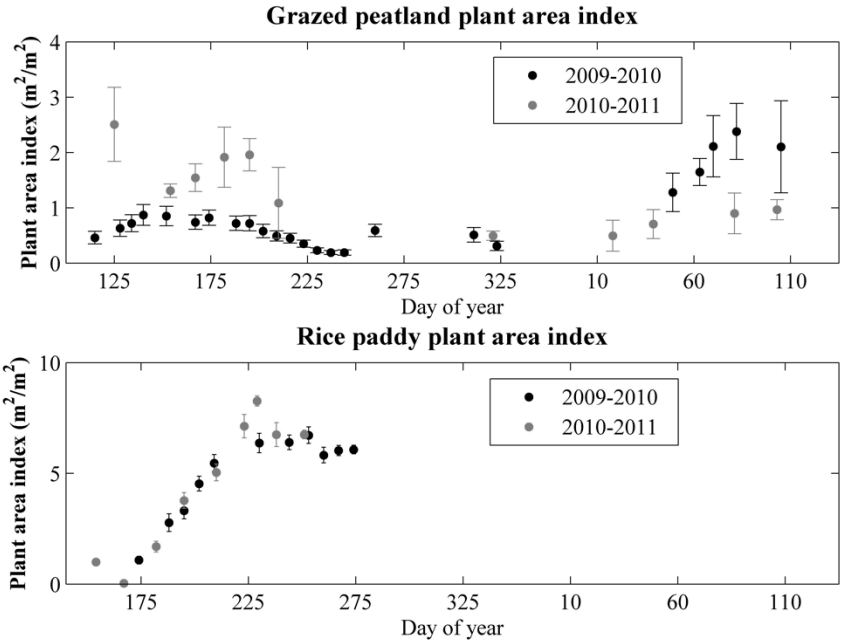

Figure 2.3 Seasonal patterns of plant area index. The plant area index was sampled at each site throughout the study period. The error bars represent standard error in the measurements with at least five samples represented by each point, and the error bars on rice paddy data are present, but some bars are too small to visualize due to low variation within sampling dates. While the pattern of plant growth is predictable and demonstrates very little interannual variation at the rice paddy, the pattern is much more heterogenous between years and within individual sampling dates at the grazed degraded peatland due to the complex vegetation dynamics of the pepperweed plant (Sonnentag et al. 2011b).

For the two years in this study, the grazed degraded peatland is relatively balanced between sensible and latent heat exchange on an annual basis, while the energy balance of the rice paddy is dominated by high rates of latent heat exchange, mostly during the summer growing season (Table 2.2; Figure 2.4). At the rice paddy, actual evaporation was 102% of potential evaporation from May 2009-April 2010 and 91% of potential evaporation from May 2010-April 2011, while at the grazed degraded peatland, actual evaporation was 52% of potential evaporation in the first year, and 63% of potential evaporation in the second year. At the rice paddy, inundation and the maintenance of a dense plant canopy during the warmest time period in the summer buffers sensible heat exchange, increases latent heat exchange, and decreases mean soil temperature when compared with the grazed degraded peatland. The energy balance is less variable throughout the year at the grazed degraded peatland, due to the more continuous plant canopy when compared with distinct growing season during half the year at the rice paddy. The daily energy balance closure of both sites, defined as the slope between the sum of daily H, LE, and G and daily measured R_{net} was 0.85 at the grazed degraded peatland. At the rice paddy, we also accounted for heat storage in the water column as the daily change in water depth multiplied by the specific heat of

water, and daily energy balance closure was 0.94. Hourly energy balance closure at the grazed degraded peatland 76% and at the rice paddy was 65%, within the bounds typically measured at eddy covariance towers across the FLUXNET network of sites (Wilson et al. 2002). The lower energy balance closure at the rice paddy is likely due to the rough approximation of heat storage in the water column in this study, as the change in water temperature was only measured at a single depth in the water column.

2.4.2 H_2O fluxes & annual budgets

Both sites had similar seasonal cycles of evaporation, as they evaporated the most water during the summer when high incoming solar radiation drives soil evaporation at the rice paddy and plant growth and maintenance drive transpiration at both sites (Figure 2.4). The rice paddy evaporated up to 10 mm d^{-1} during the summer growing season, but rates dropped to below 2mm d^{-1} during the winter, even though the surface is covered by exposed water during the winter (Figure 2.4). The grazed degraded peatland had more moderate rates of evaporation throughout the course of the year, evaporating 4-7 mm d^{-1} during the spring and early summer, and about 2mm d^{-1} during the winter (Figure 2.4). The grazed degraded peatland had notably higher evaporation than the rice paddy in winter, when grasses at the grazed degraded peatland transpired water, compared with the fallow canopy at the rice paddy.

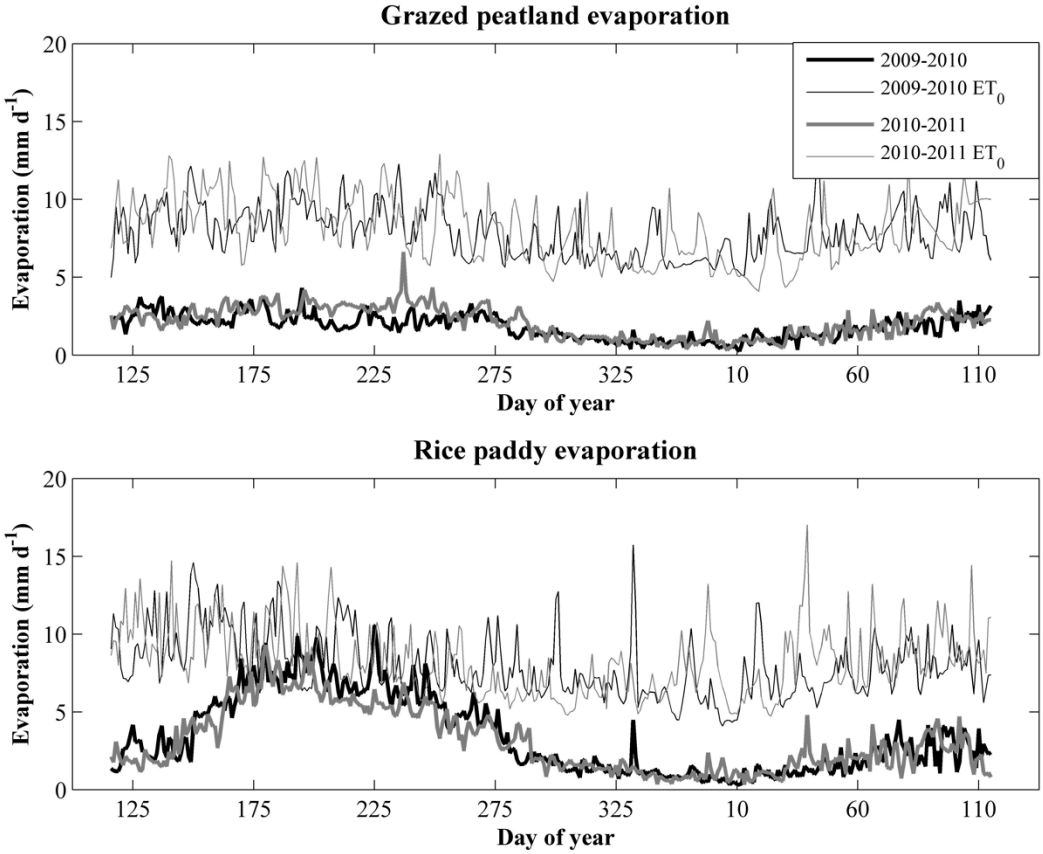

Figure 2.4 Daily potential and actual evaporation. The evaporation fluxes (thick lines) at the two sites follow the same seasonal cycle, with high rates of evaporation during the summer months, and low evaporation during the winter. The potential evaporation, calculated by the Penman equation (thin lines) was significantly higher than the grazed peatland evaporation for the whole year, but matched the rice paddy evaporation during the growing season. The grazed degraded peatland has slightly higher winter evaporation than the rice paddy due to transpiration by the grass canopy, whereas there are no plants at the rice paddy over winter to evaporate water.

Despite this slightly higher wintertime rate, the rice paddy evaporated much larger amounts of water on an annual basis when compared to the degraded peatland. The rice paddy evaporated 1207mm water in 2009-2010 and 1111mm water in 2010-2011, while the grazed degraded peatland evaporated 614mm and 757mm in those respective years. The annual budget of evaporation at the rice paddy was 94% higher than the grazed degraded peatland for the 2009-2010 budget and 47% higher than the grazed degraded peatland for the 2010-2011 budget (annual sums in Table 3). The evaporation budget at the grazed degraded peatland had larger interannual variability than that of the rice paddy due to higher variability in the canopy leaf area index (Figure 2.3), causing more variation between the two years. Whereas the maximum PAI was about 1 during the 2009 growing season, PAI reached up to 2.5 during the 2010 growing season, evaporating more water than in 2009.

Site	Year	H_2O (mm y^{-1})	NEE (g-C $m^{-2}y^{-1}$)	R_{eco} (g-C $m^{-2}y^{-1}$)	P_{eco} (g-C $m^{-2}y^{-1}$)	CH_4 (g-C $m^{-2}y^{-1}$)	Total CO_2-equivalent (g-C m-2 y-1)
Grazed degraded peatland	2009-2010	**614** (602-627)	**299** (222-373)	**1493** (1418-1582)	**-1182** -(1231-1137)	**3.3** (2.8-3.9)	**382** (293-471)
	2010-2011	**757** (741-772)	**174** (113-233)	**1765** (1691-1850)	**-1557** -(1604-1506)	**N/A**	**N/A**
Rice paddy	2009-2010	**1207** (1178-1234)	**-84** -(118-43)	**1176** (1145-1209)	**-1258** -(1290-1227)	**2.5** (2.1-2.9)	**-22** -63-29
	2010-2011	**1111** (1086-1138)	**-283** -(344-226)	**1350** (1297-1395)	**-1577** -(1630-1525)	**6.6** (6.1-7.0)	**-119** -(192-52)

Table 2.3 Annual sums of greenhouse gas fluxes. The annual sums of the H_2O, partitioned CO_2, and CH_4 fluxes (with the bootstrapped 95% confidence intervals for the gap-filling procedures in parentheses) are presented for each site during each year of the study. Positive values indicate sources to the atmosphere, and negative values are sinks from the atmosphere. At the grazed degraded peatland, the FMA CH_4 sensor did not run for the second half of the 2010-2011 time period, so we considered it imprudent to calculate the grazed degraded peatland CH_4 budget for this year. In both years, the grazed degraded peatland acted as a net source of carbon to the atmosphere, and the rice paddy acted as a net sink for carbon, although CH_4 fluxes at the rice paddy in 2010-2011 increased dramatically compared with the first year of this study. The grazed degraded peatland evaporated water than the rice paddy in both years, and generally demonstrated more interannual variability for H_2O and CO_2 exchange due to higher variation in PAI between years.

2.4.3 CO_2 fluxes & annual budgets

The overall pattern in NEE at both sites followed a similar seasonal cycle (), as most photosynthesis occurred in spring and summer, corresponding to the period with high incoming solar radiation. The highest rates of CO_2 uptake at the grazed degraded peatland, about -4g-C $m^{-2}d^{-1}$, occurred in late spring and corresponded with pepperweed growth. Even though there is a total absence of rain at the grazed degraded peatland during the late spring and summer and surface soil moisture is very low (about 7-15% volumetric water content), plant growth is nonetheless possible because pepperweed can tap the shallow water table, which is maintained by managers at about 50cm below the grazed degraded peatland surface year-round. The highest rates of CO_2 release at the grazed degraded peatland corresponded to the period of the return of autumn rainfall, and reached about 8g-C $m^{-2}d^{-1}$ of net CO_2 emissions to the atmosphere during this time. The highest rate of NEE uptake at the rice paddy corresponded with high rice photosynthesis during the middle of the growing season, and reached about -12 g-C $m^{-2}d^{-1}$. The highest period of net emission of CO2 to the atmosphere at the rice paddy corresponded with drainage events, and averaged about 6g-C $m^{-2}d^{-1}$.

High rates of photosynthesis but even higher rates of respiration at the grazed degraded peatland made it a net source of CO_2 to the atmosphere in both years of this study. The grazed degraded peatland released 299g-C/m^2 as CO_2 in 2009-2010, and 174g-C/m^2 in 2010-2011. Annual budgets in this study were a larger net source of CO_2 than in 2008-2009 due to the regrowth of pepperweed following a mowing event in early summer 2008 (a common land management practice in Delta pasture) (Sonnentag et al. 2011a). Differences in the annual NEE budget at the grazed degraded peatland between years (Figure 2.5) were primarily caused by an increase in plant growth during the 2010 growing season (Figure 2.3), as pepperweed continued to recover after the 2008 mowing event.

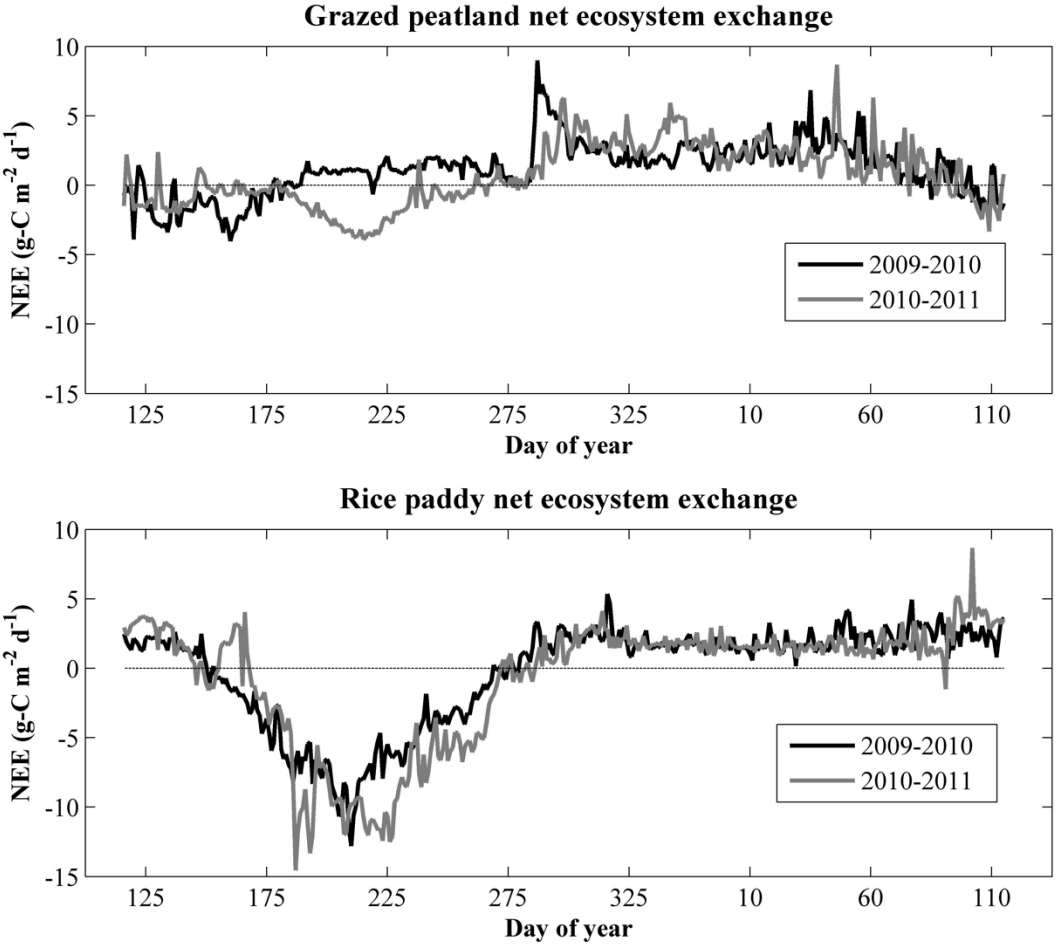

Figure 2.5 Daily net ecosystem exchange. The net ecosystem exchange at each site follows a seasonal pattern with the growing season with highest carbon uptake in the spring and summer and highest carbon efflux during winter. Error bounds derived from bootstrapping the half-hourly EC fluxes are not included in this figure since they are too small to visualize, as the 95% bounds of bootstrapped values varied only 5.1% from the measured CO_2 fluxes at the grazed degraded peatland and 4.3% of measured CO_2 fluxes at the rice paddy.

While the grazed degraded peatland and rice paddy captured similar amounts of CO_2 through ecosystem photosynthesis in both of the studied years, the CO_2 lost through R_{eco} is smaller at the rice paddy when compared with the grazed degraded peatland (Figure 2.6). The rice paddy acted as a net sink for CO_2 in both years, capturing 84g-C m^{-2} as CO_2 from the atmosphere in 2009-2010 and 283g-C m^{-2} in 2010-2011 (sums in Table 3). Differences in the net budget of CO_2 at the rice paddy between years were caused by higher rates of P_{eco} in 2010-2011 than 2009-2010, resulting in higher CO_2 uptake. Although the rice growing season extends for only half the year, ecosystem photosynthesis captures about the same amount of CO_2 as the year-round grazed

degraded peatland vegetation, and P_{eco} at the two sites only differs by about 50-75 g-C $m^{-2}yr^{-1}$ (Table 2.3).

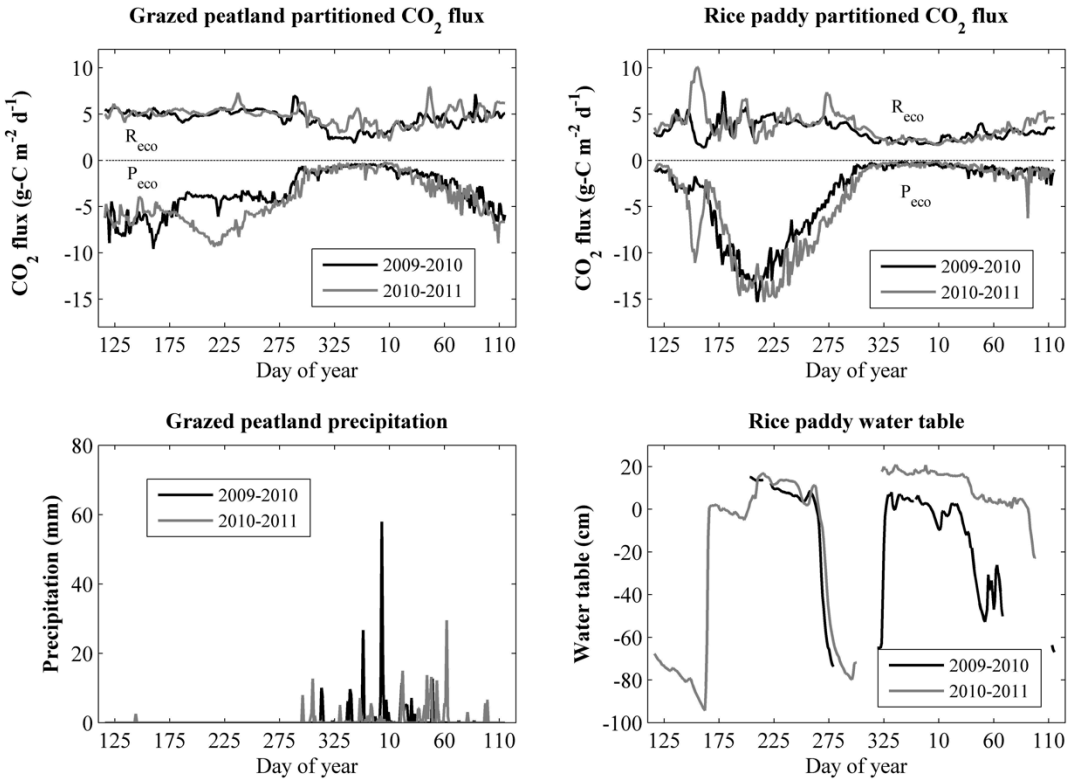

Figure 2.6 Partitioned daily CO_2 fluxes. The partitioned CO2 fluxes for the grazed degraded peatland and the rice paddy site follow the same pattern of CO2 uptake during the summer growing season. There is large interannual variability in the GEP at the grazed degraded peatland site, whereas the rice paddy shows less variation between the two years. Whereas peaks in respiration at the grazed degraded peatland are primarily governed by precipitation pulses, respiration at the rice paddy is closely tied to changes in the water table. While the addition of water by precipitation at the grazed degraded peatland has the effect of stimulating ecosystem respiration, the addition of water by flooding at the grazed degraded peatland suppresses ecosystem respiration.

Differences in the processes that control R_{eco} at each site caused variation in the seasonal pattern of R_{eco} at the grazed peatland and rice paddy (Figure 2.6). Upon the return of the autumn rains to the Delta, rates of R_{eco} at the grazed degraded peatland increased as moisture at the surface renews microbial activity, and R_{eco} increased from its summertime rate of about 5g-C $m^{-2}d^{-1}$ to 8g-C $m^{-2}d^{-1}$. At the rice paddy, the winter season is a period of low rates of R_{eco}, since decomposition and respiration occur much more slowly in the flooded and unvegetated conditions that are maintained for migrating birds. R_{eco} at the rice paddy is nearly always lower than 5g-C $m^{-2}d^{-1}$, with the exception of drainage events that create large pulses of CO_2 to the atmosphere. Thus,

while the presence of additional water during the winter months through precipitation stimulates R_{eco} at the grazed degraded peatland, total inundation at the rice paddy inhibits R_{eco}.

2.4.4 CH_4 fluxes & annual carbon budgets

Large differences exist in both the magnitude and seasonal pattern of CH_4 fluxes at the grazed degraded peatland and rice paddy (Figure 2.7). The grazed degraded peatland CH_4 fluxes in 2009-2010 and 2010-2011 had a very low and stable rate of CH_4 fluxes ranging from 1-10 mg-C $m^{-2}d^{-1}$, which increased slightly during the wetter winter months when compared with the summer when the soil surface is very dry. This pattern of degraded peatland soil CH_4 flux matches well with previous studies at the site, which concluded that the background soil flux is low, but occasionally dominated by high fluxes from wet drainage ditches, which are more frequently inundated during winter (Teh et al. 2011). The gap-filled CH_4 budget accounting for background ecosystem flux released 3.32 g-C m^2 as CH_4 to the atmosphere during 2009-2010, but we did not collect enough CH_4 flux data in 2010-2011 to reliably compute the annual sum.

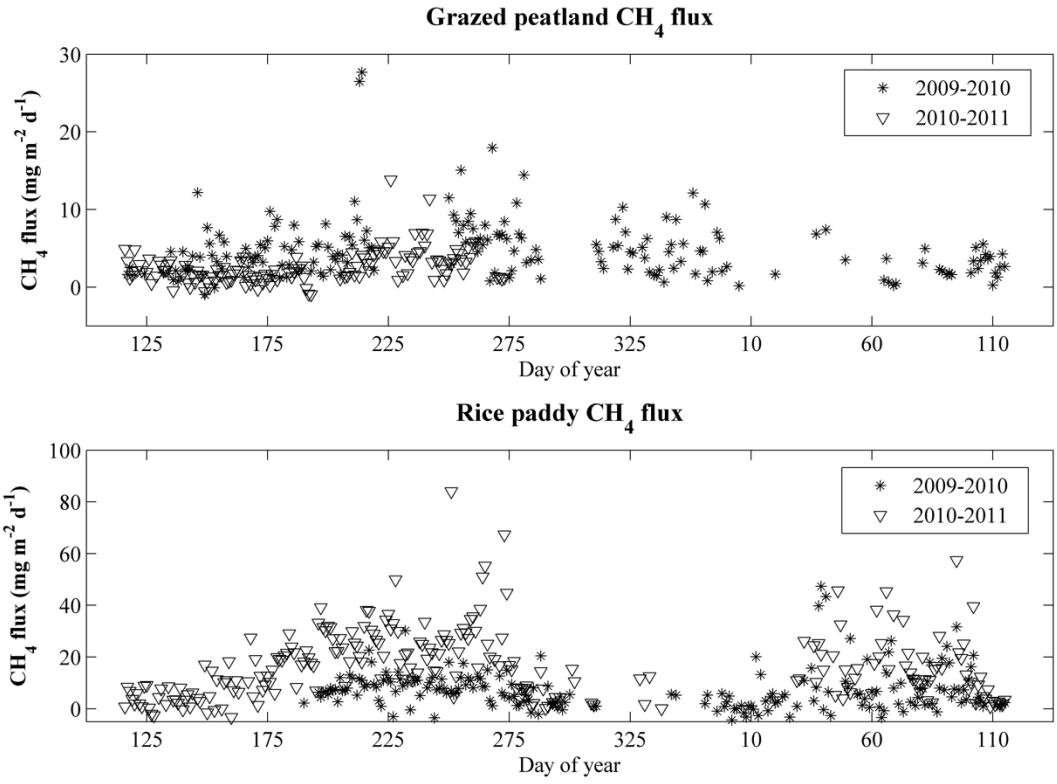

Figure 2.7 Daily methane flux. Daily integrated CH_4 flux at each site for days when there was a measured flux for at least half of the possible 48 half-hour intervals. Values are missing for many days due to instrument malfunction and/or power supply issues at the sites, particularly during the winter

months. The CH_4 sensor was removed from the grazed peatland on DOY 276 in 2010, so no values appear after this date. At the grazed degraded peatland, there are many missing values due to the filtering of fluxes when cows were present in the tower footprint. Soil fluxes at the grazed degraded peatland are generally low, although slightly higher in the wetter winter months. Although CH_4 flux was generally low at the rice paddy during the 2009 growing season, the CH_4 flux in the 2010 growing season was much larger, and followed a pattern that matched that of gross primary productivity.

The CH_4 fluxes in the first year of rice paddy measurements (2009-2010) were low at about 10mg-C $m^{-2}d^{-1}$, and did not follow a strong pattern (Figure 2.7). However, the CH_4 fluxes during the 2010 growing season followed a seasonal pattern as they paralleled P_{eco} of the rice (Figure 2.6) and peaked during drainage of the field in late September, a pattern more typical of other rice paddy studies. While the CH_4 flux was near zero in the beginning of the 2010 growing season, by August the rice paddy was emitting about 40mg-C $m^{-2}d^{-1}$ as CH_4. In the 2009-2010 annual budget the rice paddy released 2.5 g-C/m^2 as CH_4 to the atmosphere and in 2010-2011 the rice paddy released 6.6 g-C/m^2.

Using the climate warming factor for CH_4 as 25 times that of CO_2 on a 100-year horizon (Forster et al. 2007), the CH_4 emissions from the grazed degraded peatland in 2009-2010 were 83g-C/m^2 CO_2 equivalent. The same calculation for the rice paddy CH_4 emissions yields 63g-C/m^2 CO_2 equivalent in 2009-2010 and 165g-C/m^2 CO_2 equivalent in 2010-2011. While the grazed degraded peatland emitted about 25% more CH_4 than the rice paddy in the first year, assuming that the grazed degraded peatland would have emitted the same amount in 2010-2011, the rice paddy would have emitted about 50% more CH_4 than the grazed degraded peatland in the second year of this study. We also point out the relatively high uncertainty regarding the extrapolation of the annual CH_4 budget from these data due to the large amount of data missing due to power failures, instrument malfunction, and filtering due to cow presence at the grazed degraded peatland.

Using a CO_2-equivalent warming factor conversion for the annual CH_4 budget calculations of 25, we determined that the CO_2-equivalent carbon budget at both sites still follows the same trend that the annual NEE budgets indicated: the grazed degraded peatland emitted 382g-C/m^2 CO_2 equivalents in 2009-2010, and the rice paddy captured 22g-C/m^2 in 2009-2010 and 119 g-C/m^2 in 2010-2011, even after accounting for the higher-impact emissions of CH_4 (Table 3). We caution that these numbers represent emissions only after two years of land-use conversion, which is a relatively small time scale for ecological changes, and the rice paddy might continue to emit more CH_4 each year as data collection at these sites continues into the future.

2.5 Discussion

2.5.1 Water vapor

In the first year of the study, the rice paddy evaporated about 94% more water than the grazed degraded peatland site, and in the second year evaporation at the rice paddy exceeded grazed degraded peatland evaporation by about 47% (Figure 2.4; Table 2.3). This pattern matches our expectations, since the higher water table at the rice paddy is more directly exposed to the atmosphere. In addition to these fundamental differences in the annual budget due to differences in water table management, additional variability in the seasonal evaporation from each site can be explained by the differences in vegetation cover. The grazed degraded peatland has year-round vegetation cover, as pepperweed grows during the summer and grass during the winter, continually transpiring water from the soil to the atmosphere. At the rice paddy, although the water surface is directly exposed to the atmosphere during winter, there is much lower evaporation due to the very low amount of incoming radiation at this point in the year due to both the low solar angle and winter rain and fog (Figure 2.2). Thus, transpiration at the grazed degraded peatland due to the growth and maintenance requirements of the winter grasses outpaces the small amount of evaporation from the exposed water surface at the rice paddy.

A week-long study on the energy balance at a Japanese rice paddy found that rates of evaporation were near potential evaporation, although at rates from 4.2-5.8 mm d^{-1} the magnitude of evaporation was lower than in our study, likely due to the lower vapor pressure deficit when compared with our site (Harazono et al. 1998). Earlier measurements throughout the growing season at another Japanese rice paddy found similar results, with daily evaporation rates near 5 mm d^{-1}, again lower than the rates in our study likely due to the high incoming solar radiation at our site (Uchijima 1976). Our study reaches similar conclusions as those from an early lysimeter study at a rice paddy near Davis, CA (about 55km north of Twitchell Island, but climatically warmer and less windy than the Delta), which demonstrated that rice agriculture at this site on average evaporated about 1100 mm yr^{-1}, but that this evaporation budget is only 3.5% higher during the growing season than fescue, a common pasture crop of the area (Lourence and Pruitt 1971). Thus, while it seems like the differences in evaporation between the rice paddy and grazed degraded peatland are large, evaporative sums might be closer between the rice paddy and other traditional irrigated crops grown on drained soil in the Delta. In a year-long study of evaporation from five irrigated grass pastures at locations throughout California's Central Valley, experimenters found rates of evaporation that ranged from 1035-1315mm yr^{-1} (Pruitt et al. 1972), which is very similar to the evaporation rates of rice measured in this study (Table 2.3). Corn, the

dominant Delta crop, evaporates about 580-690mm of water just during the growing season (May-September) (Hoffman et al. 1983).

The evaporation rates of a restored marsh on Twitchell Island measured from 2002-2004 also fall within the same range as the measurements in this study; mean evaporation was about 6mm d^{-1} during the course of the year, and the annual budget ranged from 1480-1530 mm yr^{-1} (Drexler et al. 2008). Evaporation fluxes at a southern California marsh were much lower, with peak evaporation rates near 5 mm d^{-1} in mid-summer (Goulden et al. 2007). Rates of evaporation from the rice paddy were similar to those from a riparian cottonwood forest about 50km east of the Delta, which evaporated 1095mm yr^{-1} (Kochendorfer et al. 2011). The results from our study can also be compared with evaporation rates from 2 long-term AmeriFlux sites in an oak savanna and grassland located about 60km east of the Delta sites, which are climatically similar to the Delta, but are located on mineral soils with a much deeper water table. Evaporation of the grassland over six years averaged 319 mm yr^{-1} (Ryu et al. 2008), and that of the oak savanna ranged from 295-497 mm yr^{-1} over three years (Xu et al. 2004). This demonstrates the strong control that water availability plays in determining rates of evaporation in Mediterranean climates. At the rice paddy, the water surface is exposed to the atmosphere, driving much higher rates of evaporation, while at the grazed peatland the ability of the pepperweed plant to tap shallow water table drives higher rates of transpiration.

Differences in the evaporative balance between the grazed degraded peatland and rice paddy translate to differences in the latent heat exchange budgets due to the timing of evaporation during the year at the two sites. Because the rice paddy loses nearly its entire annual evaporation budget during the hot summer months and latent heat exchange is a function of air temperature and vapor pressure deficit, the latent heat budget of the rice paddy is much higher than that of the grazed degraded peatland on an annual basis (Table 2). Thus, although the two sites have similar levels of net radiation, the energy budget at the rice paddy is heavily weighted toward latent heat exchange, which might create a net cooling effect on the local climate at the rice paddy when compared with the grazed degraded peatland. Although our study included only two years of data, we can reasonably assume that the water use at the rice paddy will not demonstrate drastic interannual variability between growing seasons due to the regularity of the rice canopy structure between years (Figure 2.3), and thus the rice paddy can be expected to evaporate a similar amount of water into the atmosphere in future years. There may be more interannual variability at the grazed degraded peatland that parallels changes in the canopy structure at the site (Figure 2.3).

The relatively high rates of evaporation from the rice paddy within our study might be considered a negative consequence for the water budget in California, but high evaporation rates at the rice paddy also yield some benefits. On Twitchell Island, much of the water supply for the rice is pumped from island drainage ditches and recirculated rice drain water, which reduces the need for pumping of drainage water from the island. Conversion of entire islands to rice will eliminate the need for removing shallow groundwater to maintain a drained root zone and thus provide greater drainage control and reuse opportunities which will likely reduce pumping costs. Since the Delta islands where the sites are located are below sea level, land managers are required to expend large amounts of fossil fuels constantly pumping water out of the islands to prevent flooding. Pumping water throughout California is one of the highest consumers of electricity production, and thus reducing the amount of required pumping by increasing evaporation might help to alleviate some of the fossil fuels needed to regulate water supply on the islands. Conversion of Delta islands to rice production will also reduce the hydraulic forces on levees and seepage through levees. Raising the average groundwater table by about 1 meter will reduce the hydraulic gradients onto islands and thus reduce seepage, further reducing drainage pumping costs and fossil fuel consumption. Using groundwater flow modeling, Deverel *et al.* (2007) estimated that seepage will be reduced by 14-24 % relative to present-day conditions on Twitchell Island if the entire island is converted to rice or wetlands.

2.5.2 Carbon dioxide

Patterns of NEE at each site followed a seasonal pattern where carbon uptake was highest during the spring and summer months (Figure 2.5). Peak carbon uptake at each site corresponds to periods with high solar radiation since both the grazed degraded peatland and the rice paddy have a plant-accessible water table, preventing water limitation even though there is no rainfall during this period. Interestingly, both sites had similar annual budgets of ecosystem photosynthesis in each year (Table 3), indicating that the plant canopy at each site is well-established with similar carbon capture potentials. Since the grazed degraded peatland and rice paddy are situated in the same climate with the same incoming radiation, the same C3 photosynthetic pathway, and are both not water-limited, the main difference in plant cover type between the two sites is that the grazed degraded peatland has perennial vegetation with a lower canopy photosynthetic capacity, and the rice paddy has annual vegetation with a higher photosynthetic capacity than the grazed peatland. This trade-off between perennial plants with lower photosynthetic capacity and annual plants with higher photosynthetic capacity causes the integral of P_{eco} at each site to converge when considering the annual budget of photosynthesis at the site. Because on an annual basis P_{eco} is similar between sites, the differences in NEE are attributed to different rates of

R_{eco}, supporting the hypothesis that focusing management attention on limiting R_{eco} will promote net carbon capture. The differences we observed in R_{eco} between the drained grazed degraded peatland and flooded rice paddy indicated that flooding is an effective management strategy to minimize losses of C through R_{eco} by heterotrophic respiration throughout the duration of the year, as R_{eco} at the rice paddy was consistently lower than that at the grazed degraded peatland, regardless of season (Figure 2.6).

The CO_2 budget for the Sherman Island grazed degraded peatland compares relatively well with that calculated from a grazed dairy cow pasture in New Zealand, which calculated the net carbon balance (including CH_4 loss and milk loss) as source of 106.1±50 g-C $m^{-2}yr^{-1}$ (Nieveen et al. 2005). The CO_2 fluxes at Sherman Island in this study are lower than those measured and reported at other drained peatland sites on Sherman Island by Deverel and Rojstaczer (1996). For soils that ranged from 10-15% organic carbon, Deverel and Rojstaczer (1996) measured CO_2 flux with chambers and used $^{14}CO_2$ and $^{13}CO_2$ in gas samples (Rojstaczer and Deverel 1993) to estimate the portion of the CO_2 flux attributable to peat oxidation. Values ranged from 700 to 1110 g-C $m^{-2}yr^{-1}$. A key differentiating factor is likely the depth to groundwater as Deverel and Rojstaczer (1996) measured fluxes where the depth to groundwater was typically about 1m. Stephens et al. (1984) reported a logarithmic effect of changing groundwater depth on organic-soil subsidence rates and carbon loss.

The pattern of CO_2 fluxes at the Twitchell Island rice paddy (Figure 2.4) match those from work at Japanese rice paddies, which concluded that CO_2 fluxes decreased and CH_4 increased after flooding of the rice paddy soil (Miyata et al. 2000). The pattern of NEE throughout the growing season at the rice paddy corresponds well with other studies from Japan (Saito et al. 2005) and Texas (Campbell et al. 2001), although the magnitude of the partitioned P_{eco} and R_{eco} fluxes are much smaller in our study, presumably from the lower temperatures in the Delta compared with other sites that are more traditionally suited to rice agriculture. A two-year study at a rice paddy near Sacramento, CA using the eddy covariance method found a higher rate of CO_2 uptake than in our study (-594 g-C $m^{-2}yr^{-1}$) due to lower rates of R_{eco} at this site (McMillan et al. 2007). However, we expect the P_{eco} of the Twitchell Island rice paddy to increase slightly over time as the study continues and managers learn to optimize the timing of planting and harvest at this new site.

Rates of CO_2 capture at the rice paddy were slightly lower than those from a riparian cottonwood stand about 50km east of our sites, which acted as a net sink of 310g-C m^{-2} yr^{-1} (Kochendorfer et al. 2011). The magnitude of CO_2 uptake at the rice paddy was well below that from a restored marsh in southern California, where net primary productivity captured between 458-1245 g-C $m^{-2}yr^{-1}$ as CO_2 during an eight-

year study (Rocha and Goulden 2009). However, this southern California cattail marsh also had high rates of R_{eco}, making it a net carbon source of about 700g-C m^{-2} over five years of eddy covariance measurements (Rocha and Goulden 2008).

The largest seasonal variation in the CO_2 fluxes from the rice paddy was driven by changes in water and canopy management. In 2010, from about mid-May to early June, weeds filled the paddy field before planting, causing huge uptake in P_{eco} and a large release of CO_2 through R_{eco}. During this weed growth event, which lasted 32 days until the weeds were removed, 160g-C/m^2 of CO_2 was taken by weed photosynthesis (9.5% of the rice paddy annual P_{eco} in 2010-2011) and 200g-C/m^2 of CO_2 was released through enhanced R_{eco} (13% of the rice paddy 2010-2011 annual R_{eco}). This can be contrasted with the fluxes from the 2009 rice growing season that did not experience weed infiltration, when fluxes during the same time period captured 64g-C/m^2 of CO_2 through canopy photosynthesis (4.5% of the 2009-2010 annual P_{eco} budget) and released 88g-C/m^2 through ecosystem respiration (6.6% of the 2009-2010 annual R_{eco} budget). While enhanced ecosystem photosynthesis and R_{eco} somewhat balance each other out in this case when considering the net release of CO_2, the weed infiltration still caused a 106% increase in NEE during the period of weed infestation (42g-C/m^2) when compared with the same time period in 2009 (20g-C/m^2). Higher rates of NEE due to higher rates of R_{eco} than P_{eco} during the weed infestation might be attributed to soil priming by plant exudates in the well-aerated, recently disked field (Kuzyakov et al. 2000). Although higher NEE during this time period in 2010 might have also been higher due to a larger pool of labile carbon substrates from the incorporation of the rice straw from the 2009 growing season into the soil, it nonetheless created a large spike in the pattern of CO_2 exchange at the rice paddy. These results also highlight the impact that herbicides can have on the overall carbon balance of the rice paddy by controlling the amount of aerobic respiration and photosynthesis.

Flooding and drainage at the rice paddy contributes to marked pulses in CO_2 exchange (Figure 2.6). Compared with other agricultural systems, growing season respiration in rice paddies can be strongly reduced by flooding (Eugster et al. 2010), where flooding acts as a "switch" for ecosystem respiration by decreasing the habitat for aerobic microorganisms in addition to creating a barrier to gas diffusion, since diffusion through water is four orders of magnitude slower than through air. Aside from the R_{eco} pulse from the weed event in the 2010 growing season, the other pulses of R_{eco} in both years at the rice paddy are tied to flooding and drainage events. The rice paddy experiences two distinct drainage events during each year: the autumn drainage before harvest, and the spring drainage before planting. While movement of the water table recorded by the pressure transducer is rapid, the enhanced R_{eco} due to degassing during drainage typically extends over a period of 14 days. In the May 2009 – April

2010 time period, the autumn drainage released 99g-C/m^2 over 14 days (7.4% of the annual R_{eco} budget) and the spring drainage of the same duration released 74g-C/m^2 (5.5% of annual R_{eco}). In the May 2010 – April 2011 year, autumn drainage released 99g-C/m^2 as CO_2 (6.6% of annual R_{eco}). The spring drainage in the 2010-2011 time period was broken into two different events, where the first 14-day drainage event released 58g-C/m^2 (3.9% of annual R_{eco}) and the second released 77g-C/m^2 (5.1% of annual R_{eco}). This rapid loss of CO_2 upon drainage emphasizes the need for continual monitoring of CO_2 fluxes throughout the entire year, and especially during and after drainage at a seasonally flooded system like a rice paddy. Drainage events contribute significant fluxes of CO_2 from the ecosystem to the atmosphere on short timescales, and thus monitoring such events is essential for calculating accurate annual budgets of CO_2 exchange. While land managers might minimize the loss of CO_2 due to respiration by maximizing the length of flooded periods, accounting of the CO_2 loss upon drainage is essential for accurate integration of an annual CO_2 budget due to the higher magnitude drainage flux.

At the grazed degraded peatland, the surface is drained year-round, which causes extreme drying of the soil surface during the summer months, and a precipitation-induced R_{eco} pulse upon the return of the autumn rains that matches the microbial pulse response observed for other semi-arid climates (Huxman et al. 2004, Xu et al. 2004). Especially upon the first rainfall during autumn there is a large pulse in R_{eco} (Figure 2.6). However, the effect of these pulses on the annual NEE budget at the grazed degraded peatland is somewhat low, as the high rates of R_{eco} year-round at the grazed degraded peatland makes the impact of the pulses less significant. The first autumn rain in 2009 caused an R_{eco} pulse that respired 5% of the annual R_{eco} budget, and the autumn rain in 2010 created an R_{eco} pulse than respired 3% of the annual budget. These rain-induced R_{eco} pulses are not observed at the rice paddy since the water table is above the surface for most of the rainy season.

The grazed degraded peatland acted as a source for CO_2 in both years, whereas the rice paddy was an atmospheric sink for CO_2 (Figure 2.8). However, we emphasize that during the year following a pepperweed mowing event in spring 2008, the grazed peatland acted as a net sink for CO_2 as pepperweed grew more extensively and recovered from the harvest event (Sonnentag et al. 2011b). Despite having an atypical canopy cover of the invasive pepperweed plant, the Sherman Island grazed degraded peatland site during the two years in this study was near the mean NEE from extensively managed grasslands from an analysis of 172 non-forested EC flux tower sites (Gilmanov et al. 2010). A three-year study of a 10-year abandoned agricultural peatland in the Netherlands where the water table was maintained 10cm below the soil surface acted as a carbon sink in each year, taking up 232-446 g-C m^{-2}yr^{-1} through NEE

(Hendriks et al. 2007), which compares more closely to rates from the rice paddy than the grazed degraded peatland in our study.

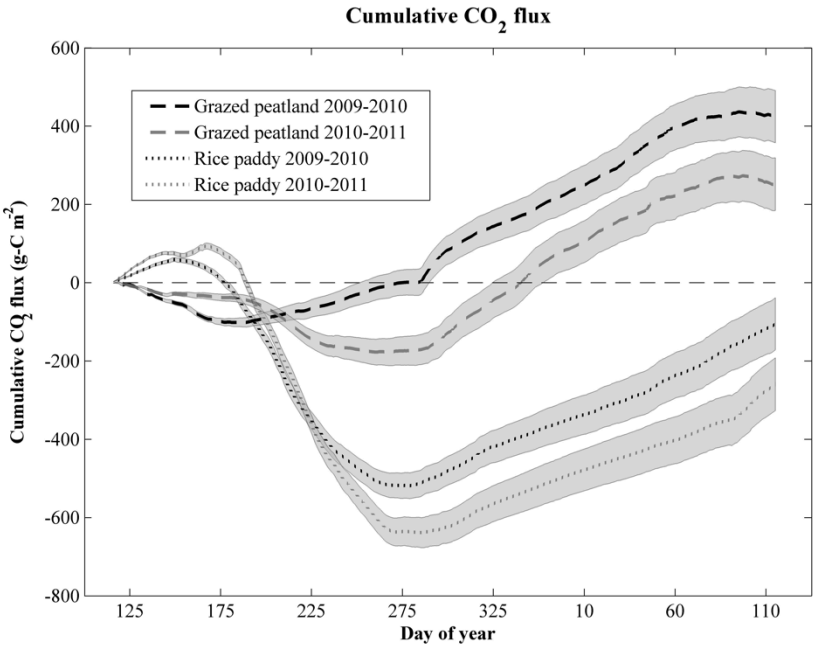

Figure 2.8 Annual cumulative CO_2 flux. Cumulative NEE is plotted for the grazed degraded peatland (dashed lines) and rice paddy sites (dotted lines) for the two years of this study. Gray shaded areas represent the 95% confidence interval from bootstrapping the half-hourly fluxes. Due to the large uptake of CO_2 during the growing season at the rice paddy and lower rates of wintertime respiration, much less CO_2 is released to the atmosphere on an annual basis. Conversely, the lower photosynthetic CO_2 uptake and high wintertime respiration at the grazed degraded peatland make it an annual CO_2 source to the atmosphere. More favorable growing conditions in the 2010-2011 season cause greater photosynthetic uptake at both sites compared with 2009-2010.

We emphasize that the CO_2 budgets for the rice paddy presented in Table 3 are budgets from an atmospheric perspective, and thus do not account for the removal of carbon from the ecosystem through rice grain harvest and addition of carbon by seed planting; the amount of carbon removed from the field through harvest was 231g/m^2 in the 2009 growing season and was 477g/m^2 in the 2010 growing season, and the amount of carbon added as seed was 16.8 g/m^2 in 2009 and 7.23g/m^2 in 2010. Considering these additional gains and losses of carbon, the rice paddy would lose a small amount of carbon in each year of the study, even though it acts as an atmospheric sink for CO_2. Our greenhouse gas budgets also do not account for secondary emissions at either site,

such as carbon footprint of electricity used to pump water or the emissions from farming machinery.

Using the partitioned annual CO_2 budgets calculated in this analysis along with soil carbon content and bulk density, it is possible to compute a "back of the envelope" approximation of the soil subsidence rates due to microbial oxidation at each of these sites. We can use the following formula to approximate soil subsidence due to soil oxidation (carbon loss) at each site:

$$subsidence = \frac{NBP}{\chi_C \rho_b}$$

where subsidence is calculated in meters, χ_C is the carbon fraction of the soil, and ϱ_b is the bulk density in g/m^3 (Table 1). NBP is net biome productivity in g-C $m^{-2}yr^{-1}$ (Chapin et al. 2006), which at the grazed degraded peatland is equal to the sum of NEE and CH_4 flux, and at the rice paddy is equal to the carbon in harvested grain subtracted from the sum of NEE, CH_4 flux, and the carbon in seeds added. At the grazed degraded peatland, we did not account for the cattle component of NBP since we did not measure the necessary parameters to track cattle growth (Soussana et al. 2007). However, we emphasize that accounting for the cattle component of NBP at the grazed degraded peatland would create a larger net carbon loss from the ecosystem, so that our estimate of grazed degraded peatland subsidence is an imperfect but conservative calculation.

If we assume that R_{eco} originates from the soil surface at the grazed degraded peatland and use the values from the top soil layer in Table 1, we calculate subsidence of 3.7mm in the first year of this study, and 2.2mm in the second year. However, if we instead assume that the grazed degraded peatland R_{eco} originates from the entire unsaturated thickness and use the average bulk density of $1.02g/cm^3$ and 0.11 for average χ_C, we calculate subsidence of 2.6mm in the first year and 1.5mm in the second year. The rates of subsidence at the degraded peatland in this study are slightly lower than those measured at a different site on Sherman Island by Deverel and Rojstaczer (1996) with χ_C of 0.16, which measured all subsidence (oxidation and compaction) at rates of 4.6 mm/yr and rates of subsidence due to carbon oxidation of 3.2 mm/yr. The differences between these rates are likely due to the shallower water table at the degraded pasture relative to the site where subsidence was measured by Deverel and Rojstczer (1996), which has an average water table of 1.2m. Stephens *et al.* (1984) demonstrated that subsidence rates in Florida peat soils where the depth to groundwater of 1.2 m were about 2-fold larger than rates in soils where the depth to groundwater was 0.6 m. The rates of subsidence at the drained degraded peatland in this study were also lower than rates measured on Sherman Island by Deverel and

Leighton (2010), which measured 5-20 mm/yr of subsidence from 1988-2006 at power pole foundations, which also maintained much deeper groundwater than the degraded pasture site in this study.

At the rice paddy, assuming that R_{eco} originates above 45cm and using the average bulk density for this layer of 0.61g/cm^3 and χ_C of 0.23, we determined that the rice paddy subsided 1.0mm in the first year and 1.4mm in the second year of this study, values lower than that from the grazed degraded peatland. While the rice paddy acts as a net carbon sink from an atmospheric perspective, it still acts as a net carbon source from a subsidence perspective due to the loss of carbon through harvest. If we do not account for the loss of grain through harvest in the NBP calculation (approximating the flooded rice paddy as a non-harvested ecosystem like a wetland) we calculated rates of soil growth at 0.58mm in the first year and 2.0mm in the second year. Although these data were collected only a small period of time after land-use conversion, they do indicate that after two years subsidence at the rice paddy is less than that from the drained and grazed degraded peatland.

It is also useful to compare the calculated subsidence with rates from soils with similar organic carbon content with additional agricultural management practices representative of the Delta. Since subsidence rates are correlated with soil organic carbon content (Rojstaczer and Deverel 1995, Deverel and Leighton 2010), larger subsidence rates than estimated for the degraded peatland are expected for soils with larger organic carbon fractions and deeper depths to groundwater. Indeed, the degraded peatland pasture is atypical as most of the Delta is farmed to corn and groundwater levels are maintained and 1-1.2 m below land surface. In a corn field in Twitchell Island, an extensometer similar to the one described in Deverel and Rojstaczer (1996) has operated since 2009 in soil with 0.15 carbon content and 1.2m water table depth. During the first 440 days of operation, we measured subsidence of 24.6 mm/yr. Consistently, on Bacon Island, Deverel and Leighton (2010) reported 22 mm/yr of subsidence from 1978 to 2006 for an average soil organic carbon content of 0.2 and water table depth of 1.2m. In light of these data, rice cultivation represents a substantial benefit for subsidence mitigation relative to other current agricultural management practices.

2.5.3 Methane

The pattern and magnitude of CH_4 fluxes at the grazed degraded peatland and rice paddy in this study were markedly different (Figure 2.7), due to the difference in the management controls on emission at each site. The background soil CH_4 fluxes at the grazed degraded peatland are a mixture of fluxes from high CH_4-emitting drainage ditches and much lower CH_4-emitting upland soils (Teh et al. 2011), and thus our

background CH_4 flux measurements represent an averaged value for this land-use. The CH_4 fluxes for the background ecosystem flux is generally stable throughout both 2009 and 2010 and averaged 5mg-C $m^{-2}d^{-1}$, with occasional fluxes of larger magnitude during the wet winter months. This pattern compares well with results of CH_4 fluxes from a heterogeneous former agricultural peatland in the Netherlands, where measurement from both eddy covariance and chambers revealed large spatial variability of fluxes between landforms, but a relatively stable rate of averaged ecosystem CH_4 flux throughout the year (Hendriks et al. 2010). However, rates of CH_4 flux in this Dutch agricultural peatland (24-96 mg-C $m^{-2}d^{-1}$) were much higher than those measured from the grazed degraded peatland in our study (2.4-12 mg-C $m^{-2}d^{-1}$), likely due to the much lower water table at our site (50-80cm) compared with the 10cm water table at the Dutch peatland. The presence of cows on drained Delta peatlands is also expected to dramatically increase the CH_4 budget of these land-uses (Shaw et al. 2007). Furthermore, the budget of nitrogen greenhouse gases is unaccounted for in each of the land use types in this study, although nitrous oxide fluxes may occasionally be high from drainage ditches at the pasture (Teh et al. 2011) and during drained conditions at rice paddies (Cai et al. 1997).

The CH_4 fluxes at the rice paddy were low and stable at about 10 mg-C $m^{-2}d^{-1}$ during the first year, but demonstrated a clear seasonal pattern of growth during the 2010 rice growing season (Figure 2.7). The CH_4 fluxes during the 2010 rice growing season ranged from near zero during the start of the growing season up to 40 mg-C $m^{-2}d^{-1}$ by mid-August 2010. The magnitude and pattern of the CH_4 fluxes from the rice paddy in this study were generally smaller than those observed by other studies of CH_4 flux in rice agriculture, although they followed a similar pattern during the 2010 growing season. Early work in Davis, CA (about 55km north of Twitchell Island, but climatically warmer than the Delta) on rice fertilized at the same rate as the rice paddy in this study calculated methane fluxes at 135mg-C $m^{-2}d^{-1}$, although this measurement was obtained through a single chamber campaign in late summer (Cicerone and Shetter 1981). Subsequent work at the same site in Davis demonstrated a strong seasonal pattern in CH_4 fluxes (ranging from 0.75–375 mg-C $m^{-2}d^{-1}$) with a peak in late summer (Cicerone et al. 1983), and mechanistic work in Italian rice fields with the same seasonal pattern (Schutz et al. 1989b) demonstrated that the late summer peak is due to favorable thermodynamic conditions for methanogenesis from acetate at this time (Kruger et al. 2001). Analysis of the year-round CH_4 budget at a rice paddy near Sacramento, CA demonstrated a strong seasonal pattern that matched that of the 2010 growing season at Twitchell Island, but with much higher CH_4 fluxes than those found in our study. The CH_4 fluxes in the Sacramento rice paddy from 2002-2004 peaked around 400mg-C $m^{-2}d^{-1}$ at the middle of the growing season (McMillan et al. 2007), much lower than the peak at 20mg-C m^{-2} d^{-1} we saw at Twitchell Island. However, we again emphasize that our

analysis only includes the first two years after land conversion, so our data might represent a land-use in a state of transition after a state change.

In this study we found very low CH_4 emissions and lack of a seasonal pattern from the Twitchell Island rice paddy in 2009 compared with typical values of CH_4 fluxes from rice agriculture (Figure 2.7). As other studies have demonstrated that the labile carbon released through decomposition drive carbon cycling in rice paddies (Cicerone et al. 1992, Kimura et al. 2004), and since 2009 was the first year of rice cultivation at this site, we suggest that the low emissions in 2009 were due to the lack of labile organic carbon substrate within the soil due to the past land-use history. When corn and alfalfa agriculture was practiced at Twitchell Island, all plant litter was harvested after each growing season, preventing the input of large quantities of fresh labile carbon back into the soil. So, although the soil has very high carbon content, we believe the pool of labile carbon compounds small enough to meet the metabolic needs of methanogens (Megonigal et al. 2003) were in insufficient quantity until the first harvest of rice straw was incorporated into the soil after the 2009 growing season. Following this line of reasoning, we expect to see growing amounts of CH_4 emitted from the rice paddy as more fresh rice straw is incorporated into the soil following the harvest each year, up to some maximum threshold of CH_4 production. Lagged effects of land-use change are important to investigate through multi-year studies, and investigation of CH_4 dynamics at this site is still underway to determine whether the difference in CH_4 between 2009 and 2010 is the result of interannual variability or represents a long-term trend.

In addition to gradual trends throughout the growing season, the pattern of CH_4 emissions at the Twitchell Island rice paddy also show a large release of CH_4 upon drainage of the field for harvest. This pattern matches that of other work that measured quasi-continuous fluxes of CH_4 upon drainage, and found that the drainage flux was due to a combination of degassing due to reduced hydrostatic pressure in addition to decreased methanotrophy (CH_4 oxidation) due to the more rapid transport of CH_4 through the soil profile (Han et al. 2005). Water table management also controls CH_4 fluxes at the Twitchell Island rice paddy, since anaerobic conditions for methane production only occur in saturated conditions, after the sequence of more favorable electron acceptors for anaerobic metabolism have been depleted (Megonigal et al. 2003). Evidence from studies in Asian rice agriculture has suggested that mid-season drainage of the rice paddy may mitigate annual emissions of CH_4, since a brief aerobic period may re-oxidize reduced alternative electron acceptors to again make methanogenesis energetically unfavorable upon re-flooding (Li 2005).

2.6 Conclusions

The Delta has experienced extreme rates of subsidence and carbon loss due to peat oxidation, and continuing the practice of drained agriculture will likely be infeasible and unsustainable in the near future. One of the most promising interventions to halt further subsidence and to turn Delta landscapes into carbon sinks is to convert drained landscapes back to flooded conditions; however, the efficacy of this practice in the Delta remains relatively untested (but for an example in a restored wetland see Miller *et al*. (2008)) . Rice agriculture has been proposed as a flooded agricultural land-use type that can prevent subsidence by limiting ecosystem respiration, and our study concluded that in the short-term, the Delta rice paddy was effective at capturing CO_2 from the atmosphere and acting as a net carbon sink from an atmospheric perspective. Considering the net biome productivity of the rice ecosystem and accounting for the carbon losses from harvest indicated that the rice paddy was still a net source of carbon from an ecosystem perspective. However, the rice paddy experienced subsidence rates lower than those of the grazed degraded peatland and more than an order of magnitude lower than subsidence rates of over 20mm/yr for agricultural soils in the Delta farmed for corn. From a subsidence perspective, rice appears to provide a substantial benefit for Delta agricultural sustainability.

The flooded status of the rice paddy also had secondary effects on the greenhouse gas budget through increased CH_4 production and higher rates of evaporation. While increased evaporation might be considered a negative consequence in water-limited California, it does benefit local farmers by reducing pumping costs. Since the Delta islands constantly leak water due to their location below sea level, land managers expend large costs to pump water out of the islands and increased evaporation saves on fossil fuels required for pumping. Another secondary ecosystem service that the rice paddy provides and is absent from the grazed degraded peatland is its ability to act as habitat for migrating birds during its flooded but fallow period during the non-growing season. Assessing these trade-offs within a policy context will reveal whether or not the benefits of land-use conversion from drained to flooded agriculture outweigh the costs.

The results from two years of flux measurements at the drained grazed degraded peatland and rice paddy indicated that converting from drained to flooded agricultural practices will help to buffer the loss of soil carbon by reducing peat oxidation in the short-term, but further research is required over a much longer timescale to determine the rate of true soil carbon sequestration. While land-use conversion to rice agriculture might be a prudent choice to abate the further loss of carbon to the atmosphere when compared with conventional drained agriculture, net soil sequestration will not be

attained until all the carbon lost from the ecosystem through grain harvest can be accounted for by more carbon uptake during the year. Some strategies that land managers might employ to further reduce the loss of carbon from rice agriculture in the Delta are to maintain the flooded status of soils for as long as possible, prevent weed infestations that cause unexpectedly large amounts of CO_2 loss, and to reduce soil disturbance such as tilling that can increase aeration and promote microbial soil oxidation. Optimizing the inclusion of rice straw to promote carbon sequestration and minimize loss of CH4 might also be a management option, as CH_4 emissions have been found to be closely tied with the amount of straw left in the field (Cicerone et al. 1992). As the rice paddy site has only been farmed as such for two years, these management options represent opportunities for future action to tip the carbon balance of the Delta rice agriculture to a net carbon sink.

The difficulty in replenishing soil carbon lost due to oxidation in the drained peatlands in this study should be of special concern with respect to the rapid drainage now occurring in the tropics through the conversion of tropical peatlands to agriculture (Jauhiainen et al. 2008). While the short-term results in this study indicated that re-flooding might help to stem the rates of soil subsidence, replenishing the carbon rapidly lost during the past century of drainage is will occur over a much longer timescale. Although there are additional water losses with converting from a drained to flooded system, these environmental costs can be weighed against the benefits of net sequestration, considering the release of CH_4 and increased rates of evaporation. This analysis provided an analysis of the short-term effects of drained to flooded agricultural land-use conversion in the Delta, and further study both at these sites and at different land-use types in the Delta will reveal whether it is feasible to transform the Delta landscape into a net carbon sink.

Chapter 3: Gross ecosystem photosynthesis causes a diurnal pattern in methane emission from rice[2]

3.1 Abstract

Understanding the relative contribution of environmental and substrate controls on rice paddy methanogenesis is critical for developing mechanistic models of landscape-scale methane (CH_4) flux. A diurnal pattern in observed rice paddy CH_4 flux has been attributed to fluctuations in soil temperature physically driving diffusive CH_4 transport from the soil to atmosphere. Here we make direct landscape-scale measurements of carbon dioxide and CH_4 fluxes and show that gross ecosystem photosynthesis (GEP) is the dominant cause of the diurnal pattern in CH_4 flux, even after accounting for the effects of soil temperature. The time series of GEP and CH_4 flux show strong spectral coherency throughout the rice growing season at the diurnal timescale, where the peak in GEP leads that of CH_4 flux by 1.3±0.08 hours. By applying the method of conditional Granger causality in the spectral domain, we demonstrated that the diurnal pattern in CH_4 flux is primarily caused by GEP.

3.2 Introduction

Rice is the dominant staple food crop for over 5 billion people worldwide (Hossain and Narcisco 2005) and contributes 11% of annual global methane (CH_4) emissions (Smith et al. 2007). Constraining carbon turnover times in rice paddy agroecosystems is particularly important for improving mechanistic predictions of CH_4 flux magnitude and timing. A diurnal pattern in CH_4 emissions from rice paddies has previously been attributed to daily fluctuations in temperature physically driving diffusive CH_4 transport (Schutz et al. 1989a, Denier van der Gon and van Breemen 1993, Hosono and Nouchi 1997). Methanogens in rice paddy soils only produce CH_4 in reduced soil conditions (Conrad 2007), and as a result many models treat CH_4 flux as a function of temperature and redox potential (Alewell et al. 2009).

However, ecosystem CH_4 flux not only depends on physiochemical environmental conditions, but is also highly regulated by the ecological function of rice plants. Rice plants provide the dominant transport mechanism for CH_4 flux from soil to

[2] This chapter is reprinted, with permission, from the original journal article: Hatala, J. A., M. Detto, D. D. Baldocchi. 2012b. Gross ecosystem productivity causes a diurnal pattern in methane flux from rice. *Geophysical Research Letters* 39(6): L06409, doi:10.1029/2012GL051303.

atmosphere by diffusive emission through their porous aerenchyma tissue (Cicerone and Shetter 1981, Holzapfel-Pschorn et al. 1986, Nouchi et al. 1990) and they are the primary source of carbon substrates for methanogenic metabolism on a range of timescales (Holzapfel-Pschorn et al. 1986, Cicerone et al. 1992, Minoda et al. 1996, Finnigan 2000, Sass et al. 2002). Net ecosystem production is highly correlated with CH_4 flux across a range of climatically diverse wetlands, indicating that substrate supply is an important control on the magnitude of CH_4 flux (Whiting and Chanton 1993). Stable isotope labeling studies in controlled laboratory settings have revealed a strong transient link between rice photosynthesis and CH_4 flux, with time lags between plant carbon dioxide (CO_2) assimilation and CH_4 emission from 2 hours to 3 days (Minoda and Kimura 1994, Minoda et al. 1996, Dannenberg and Conrad 1999).

While there is a clear link between plant productivity and CH_4 flux at the plant and plot scale, the mechanisms controlling short-term CH_4 flux in the field remain unclear based on a history of CH_4 fluxes measured with soil chambers. Diurnal coupling between photosynthesis and heterotrophic microbial respiration is an emergent property of many ecosystems (Kuzyakov et al. 2000, Vargas et al. 2010), although most chamber-based studies that directly measure CH_4 flux are not accompanied by simultaneous measurements of photosynthesis. In this analysis, we tested the hypothesis that daily carbon substrate supply by rice photosynthesis, not soil temperature, causes the diurnal pattern in rice paddy CH_4 flux by using the eddy covariance technique to measure fluxes of CO_2, CH_4, and evaporation (Baldocchi et al. 1988) over the course of a rice growing season.

3.3 Methods

3.3.1 Micrometeorological methods

We examined the relative roles of gross ecosystem photosynthesis (GEP) and soil temperature in modulating the temporal spectrum of CH_4 flux with high frequency micrometeorological data collected continuously over the course of a growing season. We measured landscape-scale fluxes of CO_2, H_2O, CH_4, and energy at a rice paddy located on Twitchell Island, CA, USA (latitude: 38.1087°N, longitude: 121.6530°W; elevation: 4m below sea level) from the emergence of rice seedlings on 15 June 2011 to harvest on 15 October 2011. The water table at the field was maintained at 5cm above the soil surface for the duration of the growing season. Winds during the study period were strong in magnitude and stable in direction where the 90% flux area footprint fell entirely within the bounds of the rice paddy. We measured soil temperature at 2cm depth below the soil surface with three replicate copper-constantan thermocouples at a

rate of 0.2Hz, recorded as half-hourly averages. At a height of 3.05m and a rate of 10Hz, we measured 3-dimensional wind velocities (u, v, w) with a sonic anemometer (Gill WindMaster Pro; Gill Instruments Ltd, Lymington, Hampshire, England), CO_2 and H_2O density with an open-path infrared gas analyzer (LI-7500; LI-COR Biogeosciences, Lincoln NE, USA), and CH_4 density with a closed-path tunable diode laser CH_4 analyzer (FMA, Los Gatos Research, CA, USA). This sampling rate allowed for a 5Hz cut-off for the co-spectra between the scalars (CO_2, CH_4, H_2O) and turbulence, which was adequate for eddy covariance measurements at this site (Baldocchi et al. 2012). Additional micrometeorological instrumentation (air temperature, humidity, barometric pressure, incoming and net radiation, precipitation, and water table depth) is detailed in (Hatala et al. 2012).

Using standard eddy covariance processing techniques, we analyzed fluxes of CO_2, H_2O, CH_4, and heat after applying corrections with in-house software (Detto et al. 2010) explained in detail in (Hatala et al. 2012). Briefly, the procedure removed artificial data spikes (greater than six standard deviations from the mean) from the 10Hz data and filtered bad readings that resulted from very infrequent fog events. For each 30-minute block of 10Hz values, we applied a coordinate rotation to align the mean vertical and lateral wind velocities to zero and removed effects of air density fluctuations by the Webb-Pearman-Leuning correction (Webb et al. 1980, Detto and Katul 2007). We applied co-spectral corrections to CO_2, H_2O, and CH_4 fluxes to account for sensor separation, and additional co-spectral corrections to CH_4 fluxes to correct for tube attenuation, residence time in the analyzer cell, and small changes in analyzer flow rate (Detto et al. 2011). We filtered 30-minute flux values with anomalously high and low friction velocity (u_*>1.2m/s and $|\overline{uw}|$<0.02) to constrain our analysis to periods where the air near the sensors was well-mixed. Of all possible 30-minute flux values during the growing season period in this analysis, 9% of CO_2, H_2O, and CH_4 fluxes were eliminated due to low friction velocity and an additional 10% of half-hourly CH_4 fluxes were not available due to brief FMA sensor malfunction.

We gap-filled CO_2 fluxes using an artificial neural network approach standardized within the international Fluxnet project with meteorological variables driving the fitting (Papale et al. 2006). To partition CO_2 fluxes into gross ecosystem photosynthesis (GEP) and ecosystem respiration (R_{eco}), we extrapolated nighttime CO_2 flux as R_{eco} using a short-term (2 week) 2cm-depth soil temperature response and subtracted daytime R_{eco} from net CO_2 flux to obtain GEP (Reichstein et al. 2005). To avoid spurious correlations between CH_4 flux and GEP, we did not gap-fill CH_4 flux data with the artificial neural network technique, and instead replaced missing values with the median for the entire growing season. There were no gaps in the soil temperature time series for this measurement period. For spectral analysis, we

standardized the CH_4 flux, GEP, and soil temperature time series to have zero mean and unit variance.

3.3.2 Wavelet spectral analysis methods

We used the continuous wavelet transform (CWT) with the Morlet mother wavelet to examine correlation between the spectra of GEP, CH_4 flux, and soil temperature (Torrence and Compo 1998). Compared with Fourier analysis, wavelet spectral analysis is a more powerful tool for analyzing geophysical time series with nonstationarity, including trace-gas flux data measured by eddy covariance (Katul et al. 2001, Vargas et al. 2010). The wavelet coherence spectrum is interpreted as the local correlation between two variables in frequency-time space where high coherence indicates phase-locked behavior between the two time series (Grinsted et al. 2004). We tested the statistical significance of wavelet power against the null hypothesis of a red noise first order autoregressive process with lag-1 autocorrelation (Grinsted et al. 2004). For time periods with significant wavelet coherence, we used the phase angle to calculate the time lag between the correlated oscillations of the two series.

3.3.3 Spectral Granger-causality analysis

We used the method of Granger causality to determine whether the patterns of wavelet coherence between the time series of GEP and temperature and CH_4 flux represented causal relationships. Granger causality is a method whereby a time series of one variable is determined to cause a second time series if it can successfully be used to predict the response of a second lagged time series (Granger 1969), and here we applied the principles of conditional Granger causality to the nonparametric spectral domain (Chen et al. 2006, Dhamala et al. 2008).

Although in this analysis we used the spectral nonparametric Granger causality analysis, we briefly review the foundation of parametric Granger causality and then explain the extension to the nonparametric form. Details on the foundations of spectral Granger causality and applications to complex ecological systems are found in *Detto et al*. [2012]. Granger initially proposed causality analysis in parametric form with autoregressive order m where the bivariate form assesses the influence of a random variable y on another random variable x as:

$$x_n = \sum_{j=1}^{m} a_{1,j} x_{n-j} + \sum_{j=1}^{m} a_{2,j} y_{n-j} + \varepsilon_n \qquad \text{(Equation 3.1)}$$

where ε_n is the bivariate prediction error and a and b are coefficients describing the linear interactions between variables with j time lags. Granger determined that y caused x by comparing the bivariate with the univariate case:

$$x_n = \sum_{j=1}^{m} a_j x_{n-j} + \eta_n \qquad \text{(Equation 3.2)}$$

where η_n is the univariate prediction error. In this form, y is said to cause x if the bivariate model outperforms the univariate model so that $\sigma^2_\varepsilon < \sigma^2_\eta$ (Granger 1969). In parametric form, Granger-causality is expressed as:

$$G_{y \to x} = \ln \frac{\sigma^2_{\varepsilon}}{\sigma^2_{\eta}} \qquad \text{(Equation 3.3)}$$

If the variables x and y are not interacting, Granger-causality will tend to zero, even if the variables are correlated. Because of temporal ordering, Granger-causality can only capture interactions that are sufficiently separated in time.

The spectral approach to Granger-causality is nonparametric, since it does not require any assumptions about the autoregressive order of the model. This approach is particularly useful for this analysis, where periodicities might be superimposed on long-term memory of the system, requiring high order autoregressive models to accurately replicate dynamics. Additionally, estimation error increases with the order of autoregressive models, which can create spurious causal relationships (Hlavackova-Schindler et al. 2007) and nonparametric analysis avoids this error.

We use the definition of Granger-causality expanded to the spectral domain (Geweke 1982, Dhamala et al. 2008) where Granger-causality I is a function of frequency f:

$$I(f)_{y \to x} = \ln \frac{S_{xx}(f)}{S_{xx}(f) - \left(\Gamma_{yy} - \frac{\Gamma^2_{xy}}{\Gamma_{xx}} \right) \left| H_{xy}(f) \right|^2} \qquad \text{(Equation 3.4)}$$

where S_{xx} is the spectral density of x at frequency f, Γ is the error covariance matrix for Equation S1 and the converse equation for the influence of random variable x on y, and H is the spectral transfer function for writing the system of equations in the Fourier domain. S is estimated directly from the spectral and cross-spectral functions of the time series and H and Γ are computed by the matrix factorization of S as described below. As in Equation S3, if x and y are not interacting, $I(f)$ will tend to zero.

We computed the spectral transfer function H and the error covariance matrix Γ from the measured wavelet spectral and co-spectral density functions of the time series. We chose wavelet rather than Fourier analysis due to the ability of wavelets to accommodate non-stationary time series and reduce spectral noise (Geweke 1982, Dhamala et al. 2008). For this spectral analysis we used the Morlet mother wavelet. In wavelet analysis, the frequency domain (given in angular frequency $\theta=2\pi f$) is discretized uniformly in the interval 0 to π after the relationship between wavelet scale s and f is known. Global spectra and co-spectra are averaged together if there are multiple realizations of the process, and the spectral matrix $S(\theta)$ is numerically extrapolated for $f \rightarrow 0$ where these spectra and co-spectra are used to infer H and Γ. In this analysis we broke the growing season dataset into realizations of 14 days to more accurately determine the causal relationship of high-frequency oscillations in CH_4 flux.

The factorization theorem of a spectral matrix states any spectrum that is Hermitian, non-negative and integrable with Fourier expansion $S(\theta) = \sum_{k=-\infty}^{\infty} \gamma_k e^{ik\theta}$ where the sequence of coefficients γ_k are given by $\gamma_k = \frac{1}{2\pi}\int_{-\pi}^{\pi} S(\theta)e^{-ik\theta}d\theta$, can be decomposed into $S(\theta) = \psi(\theta)\,\psi(\theta)'$, where $'$ denotes the matrix adjoint (Torrence and Compo 1998, Katul et al. 2001). $\psi(f)$ has a Fourier expansion in non-negative powers of $e^{2\pi if}$ given as $\psi(\theta) = \sum_{k=0}^{\infty} A_k e^{ik\theta}$ and the moving average coefficients $\{A_k\}_0^{\infty}$ are given by $A_k = \frac{1}{2\pi}\int_{-\pi}^{\pi} \psi(\theta)e^{-ik\theta}d\theta$. We use the Wilson algorithm to solve for the convergence of $\psi(f)$ (Masani 1966). The algorithm is solved by imposing the initial condition $\psi_0(\theta) = A_{0,0}$, a real, upper triangular matrix that is constant for all θ. $A_{0,0}$ can be taken by factorization of $\gamma_0 = A_{0,0}A_{0,0}'$. Once the convergence is reached, the prediction of Γ and H can be computed as:

$$\Gamma = A_0 A_0' \qquad \text{(Equation 3.5)}$$

$$H = \psi A_0^{-1} \qquad \text{(Equation 3.6)}$$

A tolerance is imposed on the determinant of Γ at each iteration step so the algorithm quickly converges.

The conditional Granger-causality is evaluated by the factorization of a spectral matrix of order three. For the trivariate system with random variables x, y, z given the factorizations $S(x,y,z) = H\Sigma H'$ and $S(x,z) = G\Gamma G'$ the conditional Granger causality of the effect of y on x given z is computed as:

$$I(f)_{y\to x|z} = \ln \frac{\Gamma_{xx}}{\left|Q_{xx}(f)\Sigma_{yy}Q'_{xx}(f)\right|} \qquad \text{(Equation 3.7)}$$

where Q is given by:

$$Q = \begin{pmatrix} \tilde{G}_{11} & 0 & \tilde{G}_{13} \\ 0 & 1 & 0 \\ \tilde{G}_{31} & 0 & \tilde{G}_{33} \end{pmatrix} \begin{pmatrix} \tilde{H}_{11} & \tilde{H}_{12} & \tilde{H}_{13} \\ \tilde{H}_{21} & \tilde{H}_{22} & \tilde{H}_{23} \\ \tilde{H}_{31} & \tilde{H}_{32} & \tilde{H}_{33} \end{pmatrix}$$

and $\tilde{H} = HP_1^{-1}$, $\tilde{G} = GP_2^{-1}$ where P_1 and P_2 are the transformation matrices needed to make the noisy terms independent.

We tested the significance of nonparametric Granger causality against the null hypothesis that no direct interaction exists by the iterative amplitude adjusted Fourier transform, which preserves the power spectrum and distribution of the original time series but eliminates the correlation structure (Wilson 1972, Molini et al. 2010). We tested the hypothesis that the periodic signal of GEP caused a periodic response in CH_4 flux after we conditioned the response for the effect of soil temperature on CH_4 flux. Support for this hypothesis indicates that GEP modulates CH_4 flux at the time lags indicated by the spectral analysis.

3.4 Results & Discussion

3.4.1 Analyzing the interactions between CH_4 flux, soil temperature, and GEP

GEP, CH_4 flux, and soil temperature all demonstrated a strong diurnal pattern for the duration of the growing season, where the daily peak in GEP leads that of CH_4 flux and soil temperature (Figure 3.1a-c). The mean growing season peak in GEP occurred in late morning at 11:00 hours, the mean peak in soil temperature occurred in late afternoon at 16:30 hours, and the mean peak in CH_4 flux occurred in mid-afternoon at 14:30 hours. If either GEP or soil temperature are driving the diurnal pattern in CH_4 flux, we would predict that the diurnal peak of GEP or soil temperature would temporally lead the peak in CH_4 flux. However, this is not the case, as GEP leads CH_4 flux, but the peak in soil temperature lags both of these variables. All variables also demonstrate coherent seasonal trends, where GEP peaks mid-season, CH_4 flux increases and soil temperature at 2cm depth decreases throughout the season (Figure 3.1d-f). The contrary seasonal pattern of decreasing soil temperature but increasing CH_4 flux provides further evidence that soil temperature might not be driving CH_4 flux. The

application of a general herbicide for weed control in the field at day of year 179 caused a sharp decline in GEP (Figure 3.1e) with a concomitant decrease in CH_4 flux (Figure 3.1d), also providing qualitative mechanistic insight regarding the strong control of GEP on CH_4 emission.

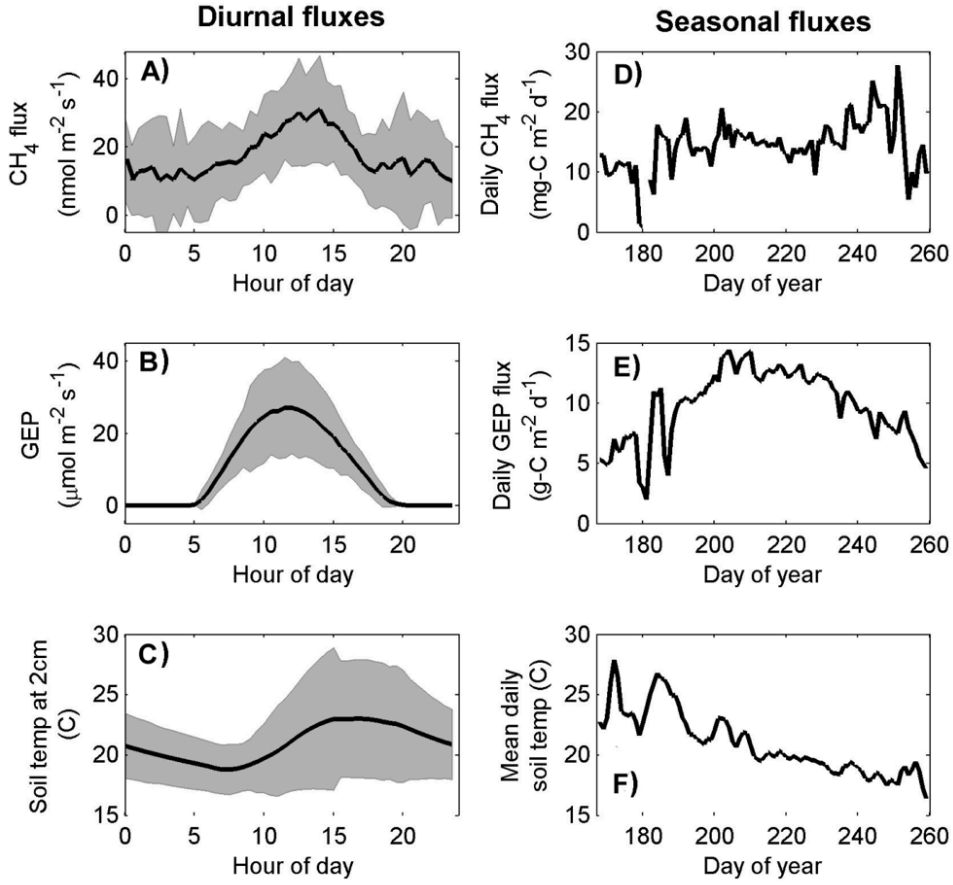

Figure 3.1 Diurnal and seasonal patterns in CH_4 flux, soil temperature, and photosynthesis. A-C) CH_4 flux, gross ecosystem productivity (GEP), and soil temperature at 2cm depth all demonstrate a diurnal pattern for the duration of the rice growing season, where the solid line represents the growing season mean, and the shaded area represents the growing season standard deviation for each half-hour interval. The diurnal peak in GEP leads that of CH_4 flux, soil temperature, and evaporation, indicating that GEP is a more likely driver of the daily peak in CH_4 flux than soil temperature. **D-F)** These figures show the trend across the growing season for CH_4 flux, GEP, and soil temperature at 2cm depth. GEP shows strong seasonality with a mid-summer peak, while CH_4 flux increases throughout the growing season and soil temperature decreases over the course of the season. Low values of GEP at day of year 178-180 are caused by the application of a general herbicide to the field to control the growth of weeds with a concomitant decrease in CH_4 flux, indicating a strong link between these two variables.

We examined the wavelet coherence spectra (Torrence and Compo 1998, Grinsted et al. 2004) to determine the dominant timescales and strength of coupling between CH_4 flux and GEP and soil temperature. GEP and CH_4 flux are strongly coherent throughout the growing season at the daily timescale, where the mean lag time with 95% confidence interval is 1.3±0.08 hours (0.350±0.021 radians) (Figure 3.2a). The soil temperature and CH_4 flux time series are also significantly coherent at the daily period (Figure 3.2b), however soil temperature lags CH_4 flux by 5.5±0.1 hours (-1.47±0.030 radians). The soil temperature-CH_4 flux wavelet coherence is also significantly coherent at the weekly time period (Figure 3.2b), and the mean time lag here is 14±1.8 hours (0.52±0.079 radians). Although both GEP and soil temperature are correlated with CH_4 flux at multiple timescales, strong coherencies occur at the daily timescale that are maintained for the duration of the growing season. Soil temperature is also highly correlated with CH_4 flux at the weekly period, which might indicate a relationship where soil temperature drives kinetic rate changes in CH_4 flux on longer timescales.

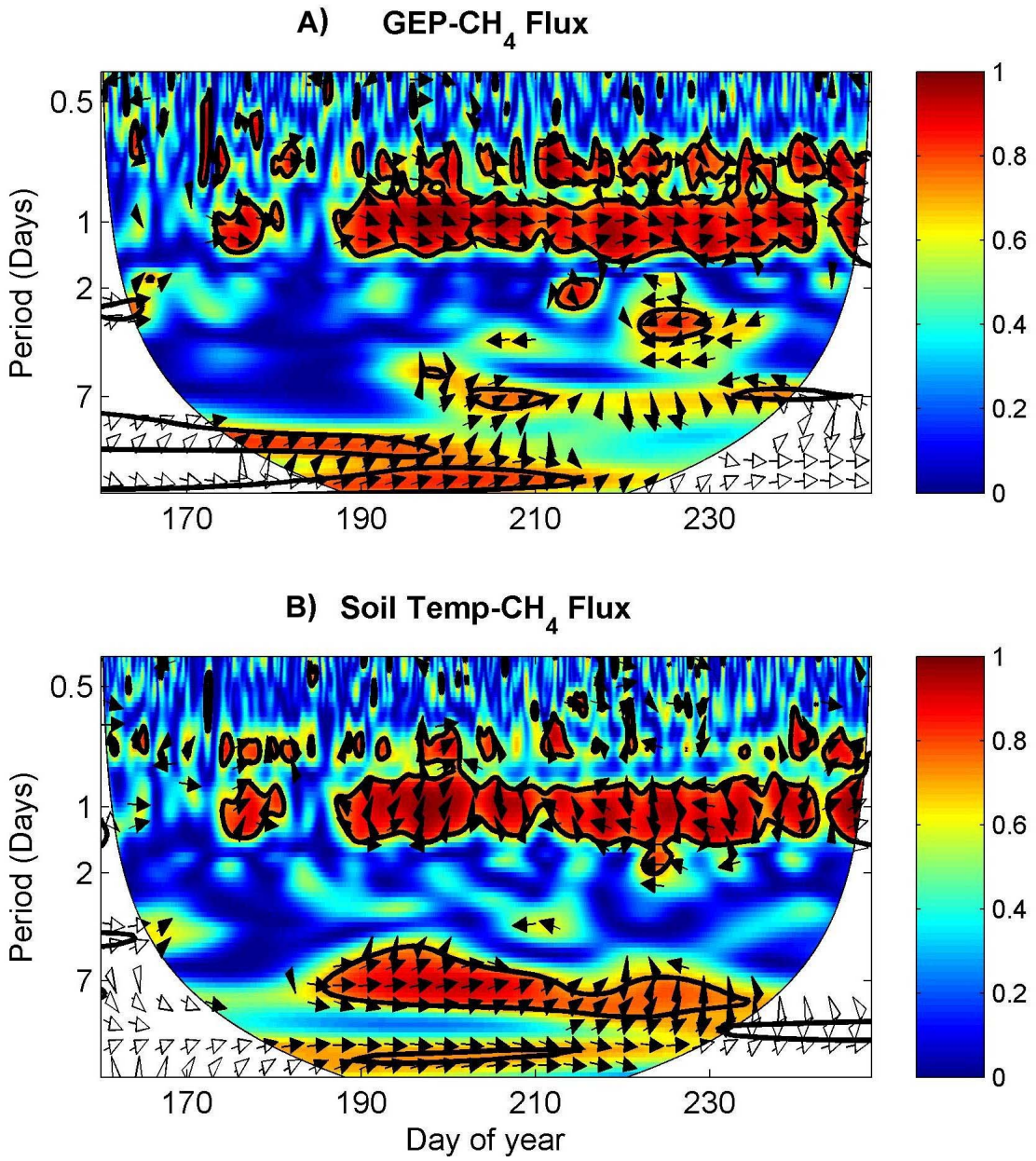

Figure 3.2 Wavelet coherence between CH_4 flux, soil temperature, and GEP. The wavelet coherence between GEP and CH_4 flux for the rice paddy growing season shows high in-phase coherence between the two time series at the daily timescale for the duration of the growing season, and lower periodic coherence at the 18 hour, weekly, and bi-weekly timescales. Soil temperature and CH_4 flux have the highest coherency at the daily and weekly timescale, whereas soil temperature and GEP are coherent at the daily timescale. Significant coherency (at the 5% level with 1000 Monte Carlo simulations of AR-1 autocorrelation) is indicated by the bold black lines. The direction of arrows indicate the phase angle between the two time series, where an arrow with an inclination of zero pointed to the right indicates zero lag (the series are perfectly correlated). The cone of influence represents the limit where wavelet power dropped to e^{-2} of the edge values.

From the spectral Granger causality analysis, we found strong support for the hypothesis that GEP modulates CH_4 flux at the daily timescale. The GEP-CH_4 flux Granger causality spectrum (Figure 3.3a) shows strong power at the daily timescale as well as at the harmonic 12-hour timescale after accounting for the effects of soil temperature on CH_4 flux. The spectrum of GEP-induced CH_4 flux demonstrates that carbon cycling between plants and methanogens occurs rapidly with a coherent temporal pattern that is maintained for the duration of the growing season. We also tested the alternative hypothesis that soil temperature causes a diurnal pattern in CH_4 flux, and conditioned this relationship on GEP. Soil temperature modulates CH_4 flux over a longer five-day timescale and demonstrates a much weaker daily signal than that of GEP-induced CH_4 flux (Figure 3.3b). Since a few observations have suggested that stomatal conductance might drive CH_4 flux (Chanton et al. 1997), we tested but did not find strong support for this other alternate mechanism.

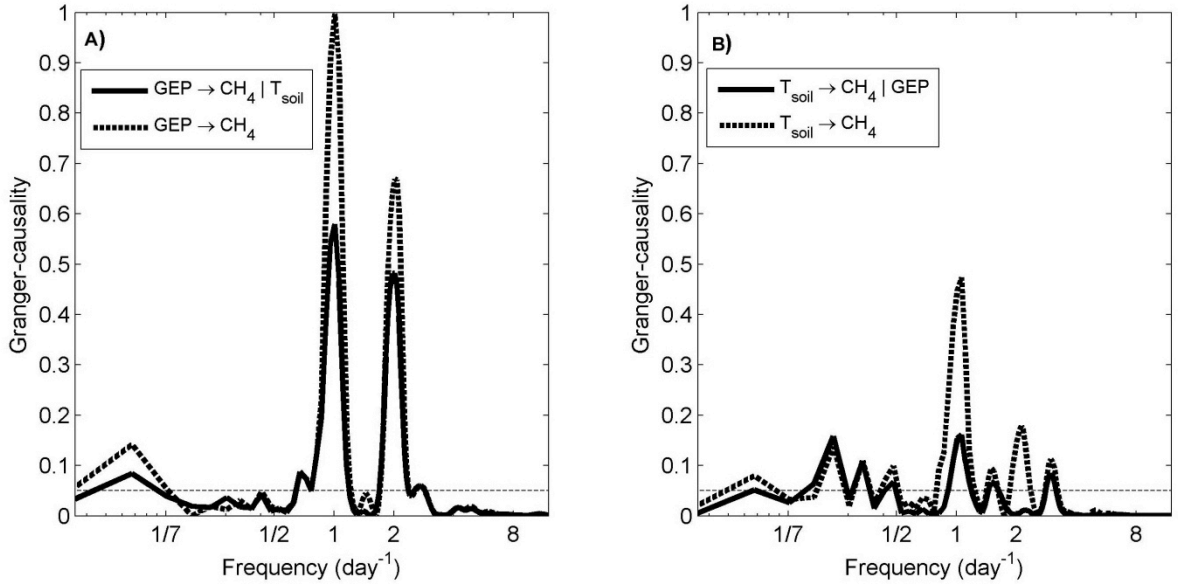

Figure 3.3 Granger-causality metric for the interactions between CH_4 flux, GEP, and soil temperature. The Granger-causality spectra are plotted for the causal relationships between GEP and soil temperature and CH_4 flux. When conditioned on soil temperature, GEP still has a strong causal relationship with CH_4 flux at the daily timescale. Conversely, when soil temperature is conditioned on GEP the Granger-causality at the daily timescale becomes insignificant, although temperature is still a significant driver of CH_4 flux for frequencies smaller than 0.5 day^{-1}.

3.4.2 Testing the alternate hypothesis that stomatal conductance drives CH_4 flux

Although there is limited direct evidence for a link between stomatal conductance and CH_4 flux (Nouchi et al. 1990), we also evaluated the alternative hypothesis that mass flow through canopy stomatal conductance (G_s) regulates CH_4 flux. To compute stomatal conductance for the rice growing season, we used the Penman-Monteith equation with our measured micrometeorological fluxes and variables. We calculated G_s as:

$$G_s = \left(\frac{s(R_n - G) + \rho_a C_p D G_a}{\gamma \lambda E G_a} - \frac{s}{\gamma G_a} - \frac{1}{G_a} \right)^{-1} \qquad \text{(Equation 3.8)}$$

where G_s is canopy stomatal conductance in m/s, s is the slope of the relationship between saturation vapor pressure and temperature in Pa/K, R_n is measured net radiation and G is measured soil heat flux in $Wm^{-2}s^{-1}$, ρ_a is the dry air density in kg/m^3, C_p is the specific heat capacity of water equal to 1003.5 J $kg^{-1}K^{-1}$, D is the measured vapor pressure deficit in Pa, γ is the psychrometric constant equal to 66 Pa/K, and G_a is the canopy boundary conductance in m/s, calculated as:

$$G_a = \frac{u_*^2}{\overline{u}} \qquad \text{(Equation 3.9)}$$

where u is the measured 10Hz streamline wind speed averaged over each 30-minute interval and u^* is the measured friction velocity in each 30-minute interval.

The stomatal conductance for the growing season follows a distinct diurnal pattern, as we would expect from the daily pattern of photosynthesis (Figure 3.4).

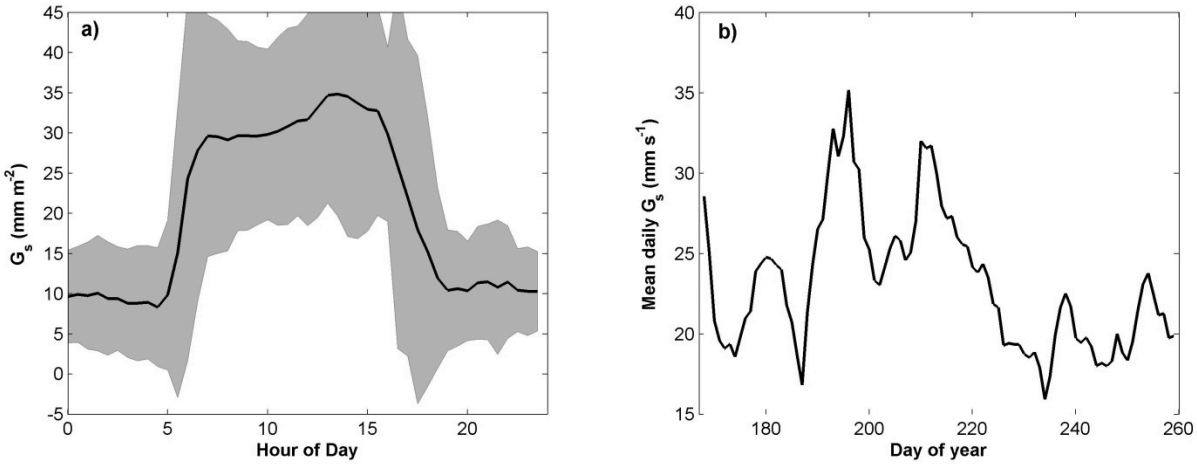

Figure 3.4 Diurnal and seasonal trend in canopy conductance A) Canopy stomatal conductance follows a strong diurnal pattern during the growing season, where G_s increases rapidly following sunrise, and begins to decrease quickly around hour 15. **B)** The pattern of canopy stomatal conductance also follows a seasonal pattern that corresponds to different rice developmental stages. G_s is high during tillering (leaf growth and expansion) and flowering, and decreases during grain formation.

G_s increases rapidly following sunrise, and decreases rapidly around hour 15 each day, while the mean growing season rate is about 30-34 mm/s during daylight hours (Figure 2a). Although G_s leads the diurnal peak of CH_4 flux, if G_s were driving CH_4 flux we would expect to see a corresponding increase in CH_4 flux much earlier, rather than when G_s begins to decrease for the day. Computing the conditional Granger causality for the hypothesis that G_s causes CH_4 flux conditional on the relationship between both GEP and temperature and CH_4 flux revealed that there is no direct causal link between G_s and CH_4 flux within our dataset (Figure S3). This analysis allows us to reject the alternative hypothesis that stomatal conductance causes the diurnal pattern in CH_4 flux, and reinforces the connection between GEP and CH_4 flux.

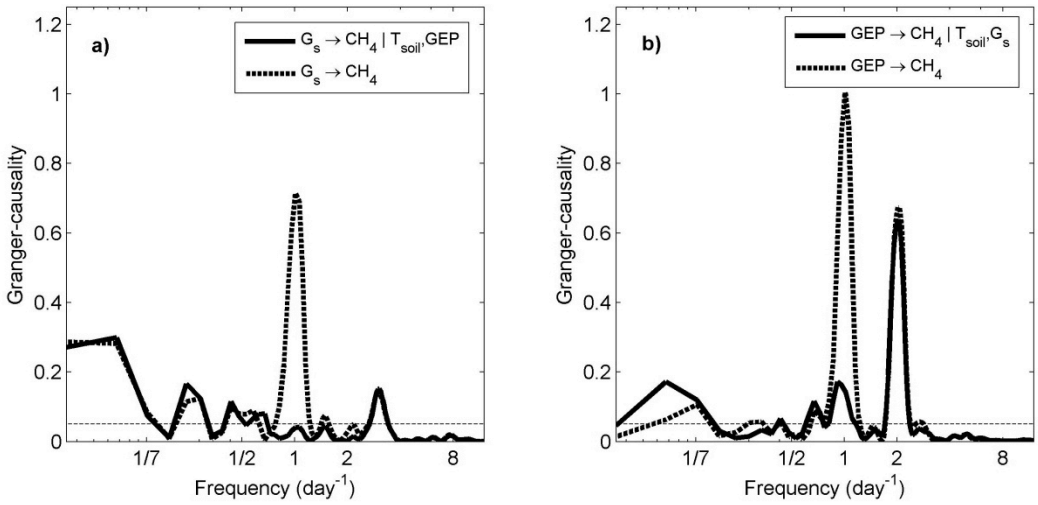

Figure 3.5 Granger-causality metric for the interaction between CH_4 flux, GEP, and canopy conductance. The Granger-causality for the hypothesis that G_s causes CH_4 flux at the daily timescale has little support after accounting for the relationship between GEP and soil temperature and CH_4 flux. Conversely, when accounting for G_s, GEP remains a significant predictor of CH_4 flux at the daily and harmonic 12-hour timescales.

3.5 Conclusions

Understanding the temporal lags of carbon turnover from plants to methanogens is essential for scaling methanogenesis to ecosystem-level CH_4 flux. Our analysis concludes that in rice, CH_4 flux rapidly response to GEP in a coherent pattern for the duration of the growing season. Although this analysis is conducted in a spatially homogeneous rice paddy, it may yield insight into the high-frequency mechanisms that contribute to variability in CH_4 flux measurements at spatially heterogeneous sites. For example, if photosynthetic rates vary across the landscape and high-frequency CH_4 flux is driven by GEP, accurately measuring and modeling photosynthesis might help explain at least some of the heterogeneity in CH_4 flux. The diurnal pattern of GEP-regulated CH_4 fluxes also has direct implications for the daily and seasonal extrapolation of studies that measure only daytime CH_4 flux, due to an inability to account for diurnal variation in CH_4 flux due to changes in GEP. Furthermore, the strong connection between GEP and CH_4 flux found in this study highlights a possible trade-off in using flooded ecosystems for carbon capture and sequestration, a subject of research that warrants further study at other sites. This analysis re-examines assumptions about the importance of biotic and abiotic factors in regulating landscape-scale CH_4 flux on the timescale of hours to days, and concludes that gross ecosystem photosynthesis is the primary cause of the diurnal pattern in rice paddy CH_4 flux.

Chapter Four: Abundance and fractal complexity of emergent vegetation controls landscape-scale CO_2 and CH_4 flux in a recently restored wetland

4.1 Abstract

Landscape heterogeneity is an important driver of variability in CO_2 and CH_4 fluxes measured by eddy flux towers in many ecosystems. In this analysis, I examined the impacts of spatially heterogeneous vegetation patterns on measured CO_2 and CH_4 fluxes from three eddy flux sites within a recently restored wetland. I combined a two-dimensional analytical flux footprint model with a time series of satellite images classified for emergent vegetation to analyze the impact of emergent vegetation abundance and fractal scale (a metric of spatial complexity) on measured CO_2 and CH_4 fluxes. Both the vegetation abundance and fractal dimension within the flux footprint explained variability in the maximum daily flux of CH_4 and minimum daily flux of CO_2. The maximum daily CO_2 flux was slightly correlated with vegetation abundance, but was better explained by nighttime air temperature. This analysis yields important insights for engineering restored wetlands for ecological carbon sequestration.

4.2 Introduction

Measured CO_2 and CH_4 fluxes from peatland and wetland ecosystems have notoriously large spatial and temporal variability that can span orders of magnitude within a single landscape (Baldocchi et al. 2012). Understanding the contribution of spatial and temporal heterogeneity to measured CO_2 and CH_4 flux is essential for analyzing the mechanistic drivers of ecosystem carbon cycling. In northern peatlands and wetlands with spatially variable soil moisture, vegetation cover, and land-use, incorporating wind direction as a mechanistic driver to account for sub-landscape-scale variation has proven essential for interpreting and modeling CO_2 and CH_4 fluxes measured by eddy covariance towers (Herbst et al. 2011, Parmentier et al. 2012). In heterogeneous agricultural peatlands, knowing the relative percentage of the landscape composed of drainage ditches and uplands is critical for calculating a landscape-scale flux since the CH_4 fluxes within these two land features can differ by up to three orders of magnitude (Schrier-Uijl et al. 2010, Teh et al. 2011). Recent work also demonstrated that oversimplification in the spatial and temporal representation of water table variability at periodically inundated peatlands can result in large modeled CH_4 flux biases (Bohn and Lettenmaier 2010). Although the environmental mechanisms that initiate and preserve landscape-scale heterogeneity vary among wetlands, the

integration of satellite imagery with landscape-scale flux measurements is a promising avenue for detangling variability in CO_2 and CH_4 flux measurements that originates from differences in land cover.

In this study, conducted at a restored wetland in California, I investigated the impact of spatially heterogeneous vegetation cover on landscape-scale CO_2 and CH_4 fluxes by integrating flux footprint modeling and remote sensing imagery with measured eddy covariance fluxes from one stationary and one mobile tower that visited two other locations on weekly intervals throughout the summer growing season. The flux footprint describes the spatial portion of the landscape represented by each half-hourly eddy covariance flux measurement and is a function of land surface roughness and atmospheric turbulence and stability. To examine the impact of spatial heterogeneity on the measured fluxes in this analysis, I used a two-dimensional analytical flux footprint model (Hsieh et al. 2000, Detto et al. 2006). Flux footprint models have been previously used to interpret how spatial heterogeneity contributes to variability in CO_2 fluxes measured by eddy covariance in Eastern forests (Chasmer et al. 2011) and to validate the quality of eddy covariance measurements with respect to their representativeness of particular land-use types (Goeckede et al. 2004, Goeckede et al. 2008). The use of periodic remote sensing images in combination with flux footprint models is especially useful for identifying variability in the measured eddy covariance fluxes due to ecosystem dynamics in non-steady-state landscape conditions, such as disturbance and restoration. Here, I used high spatial resolution satellite imagery from the WorldView-2 satellite (pixel size of ~2m) to classify emergent vegetation within the restored wetland in tandem with the flux footprint model in order to determine the emergent vegetation abundance and spatial pattern contributing to each measured half-hourly CO_2 and CH_4 flux.

Different mechanisms operate in vegetated and open water areas to impact the overall net CO_2 and CH_4 fluxes measured by eddy covariance towers. Areas covered by plants have high rates of CO_2 uptake and also produce the highest rates of CH_4 efflux, since porous aerenchyma tissue used to transport oxygen from the atmosphere to roots is also a key conduit for CH_4 flux from the soil to the atmosphere (Chanton et al. 1992, Schimel 1995). Plants also impact the net CH_4 released to the atmosphere by redox cycling of alternative microbial electron acceptors in the rhizosphere, which influence rates of CH_4 production and consumption (Neubauer et al. 2005, Laanbroek 2009). Fluxes of CH_4 from open water surfaces are regulated by diffusion and ebullition (bubbling), where rates of diffusive CH_4 efflux are often correlated with friction velocity (u^*; m/s) from open water surfaces (Herbst et al. 2011). The rate of CH_4 flux from ebullition is a function of net CH_4 production and accumulation in the soil and fluctuations in hydrostatic pressure that release bubbles from the soil to the surface

(Walter et al. 2008, Varadharajan et al. 2010). The net flux of CO_2 and CH_4 measured by eddy covariance towers is the aggregate result of these mechanisms operating simultaneously in the landscape.

Because the mechanisms controlling CO_2 and CH_4 flux differ between vegetation and open water, I hypothesize that the abundance and landscape structure of emergent vegetation within the flux footprint can help explain observed variability in the measured eddy covariance fluxes. I expect areas with a high abundance of emergent vegetation to have the largest CO_2 uptake and largest CH_4 release, since photosynthesis by emergent vegetation is the most significant ecosystem sink of CO_2, and emergent vegetation also convectively transports CH_4 from the soil to the atmosphere. I also expect that the spatial pattern of emergent vegetation within the flux footprint will impact the measured CO_2 and CH_4 fluxes. If the emergent vegetation within the footprint occurs in a pattern with large patch perimeters (i.e. large patch edges), it is likely that CO_2 uptake would be larger than a scenario with a smaller patch perimeters but the same overall vegetation abundance, as light harvesting by leaves is more efficient at edges compared with patch interiors. And conversely, I would expect that CH_4 flux would be lower in a scenario with longer patch edges, as the increased edge length provides more opportunity for the carbon substrate produced as root exudates to flow laterally into areas outside the immediate rhizosphere, where it is less likely to be respired by microbes. Additionally, in a scenario with longer patch edges, the CH_4 produced in the rhizosphere could also flow laterally into deeper water where it escapes transport by emergent vegetation and instead is released in larger but more infrequent ebullition events.

In this analysis conducted from May to October 2012, I combined measured CO_2 and CH_4 fluxes from eddy covariance towers at three locations with high-resolution satellite imagery and a two-dimensional flux footprint model to examine the influence of emergent vegetation abundance and spatial patterning on CO_2 and CH_4 flux. This work is motivated by the following research questions:

1) How variable are growing season CO_2 and CH_4 fluxes across sites within the same restored wetland ecosystem?
2) Is temporal variability in net CO_2 and CH_4 fluxes measured by the eddy flux towers driven by spatial changes in the flux tower footprints?
3) How well does the emergent vegetation abundance within the flux footprint explain variability in the measured CO_2 and CH_4 fluxes?
4) How does spatial patterning of emergent vegetation within the flux footprint impact the net CO_2 and CH_4 fluxes measured by the flux towers?

This suite of research questions advances understanding of ecosystem-atmosphere carbon fluxes in restored wetlands, which have been identified as having major potential for ecosystem carbon sequestration in the future (Miller et al. 2008). Additionally, the combined flux footprint and remote sensing framework presented in this analysis can be extended into other spatially heterogeneous ecosystems measured by eddy flux towers. As investigators seek to measure eddy fluxes of more spatially variable trace gases, like CH_4 and N_2O in complex landscapes, this type of analysis can act as a guide to assess the impacts of spatial heterogeneity from both footprint composition and vegetation structure on measured eddy covariance fluxes.

4.3 Methods

4.3.1 Site description

The site in this analysis is a restored wetland (latitude: 38.049722°N, longitude: 121.765070°W, elevation: 3m below sea level) that was converted from a drained degraded peatland pasture by flooding in October 2010 (Figure 4.1a). Before the field was flooded, a heterogeneous bathymetry was excavated within five checks surrounded by built-up levees to preserve small patches of extant wetland vegetation and create areas of shallow water and contiguous areas of deep water. As a result, the water depth at the site ranges from a few centimeters to about 2m. Maintaining spatial heterogeneity of shallow and deep water areas was identified as a management goal in this restoration project, as spatially heterogeneous wetlands might act as 'keystone structures' that encourage biodiversity (Tews et al. 2004).

Vegetation patches within the wetland are composed of *Schoenoplectus acutus* (common names: tule, hardstem bulrush) and *Typha latifolia* (common names: cattail, bulrush). *Typha latifolia* is a cosmopolitan plant that reproduces primarily through clonal ramet growth, with a dense advancing front of sprouts that outcompete other plants, aptly described as a 'phalanx strategy' of population growth (Dickerman and Wetzel 1985). *Schoenoplectus acutus* is a native wetland species specific to North America that also reproduces clonally, but is often outcompeted by the faster and more densely sprouting *Tyhpa* species (Farrer and Goldberg 2009, Miller and Fujii 2010). Data were collected at the site from 9 May to 25 October in 2012, when temperatures and incoming solar radiation were high and precipitation was absent due to the Mediterranean climate of the area.

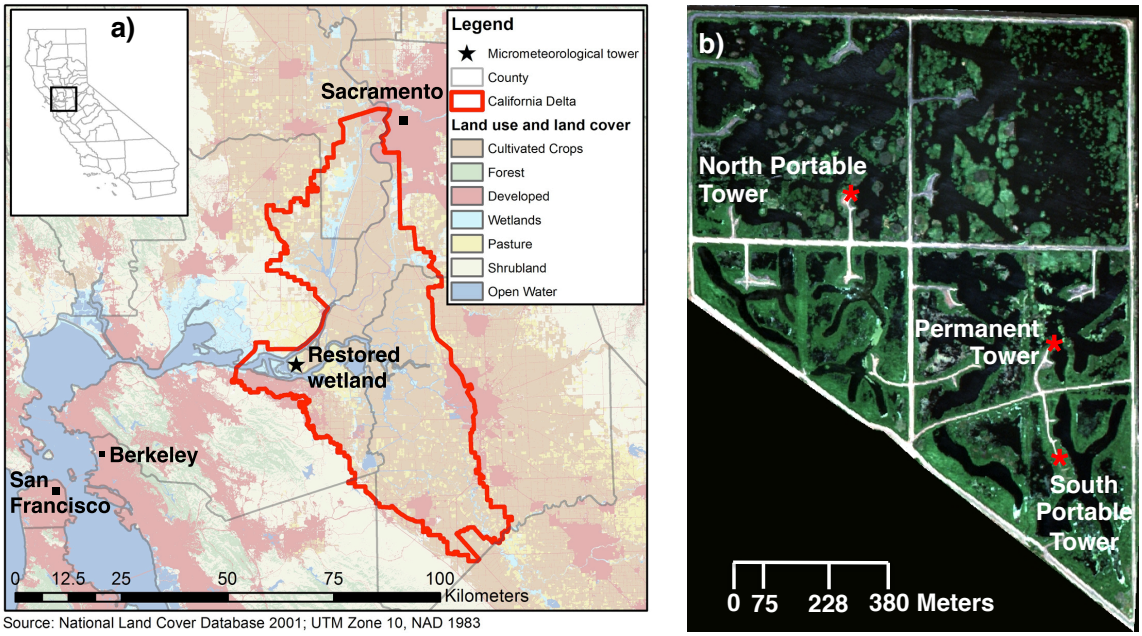

Figure 4.1 Map of study site and eddy flux tower locations. a) The restored wetland is located at the west end of the California Delta, about midway between San Francisco and Sacramento in an area mostly used for agriculture and pasture. **b)** This red-green-blue WorldView-2 satellite image captured on 9 July 2012 shows the relative locations of the restored wetland Permanent Tower and the North and South Portable Tower locations.

4.3.2 Eddy covariance flux measurements

I measured fluxes of CO_2, CH_4, water vapor, and energy from 9 May 2012 until 25 October 2012 (170 days total) with two eddy covariance systems at the wetland: one stationary tower in the center of the wetland (hereafter referred to as 'Permanent Tower') and a second mobile tower built in the back of a pickup truck that was moved every week between one location south of the permanent tower ('South Portable Tower') and a second location north of the permanent tower ('North Portable Tower') (Figure 4.1b). Eddy covariance instrumentation at the Permanent Tower was situated 4.08m above the wetland water surface and the Portable Tower eddy covariance instrumentation was located 4.26m above the water surface. Each tower contained an identical set of eddy covariance instrumentation. I measured wind speed in three directions and the speed of sound (u, v, w, sos; m/s) with a sonic anemometer (Gill WindMaster Pro; Gill Instruments Ltd, Lymington, Hampshire, England), CO_2 and H_2O density (ϱ_{CO2}, ϱ_{H2O}; mmol/m^3) with an open-path infrared gas analyzer (LI-7500; LI-COR Biogeosciences, Lincoln NE, USA), and CH_4 density (ϱ_{CH4}; mmol/m^3) with an open-path infrared gas analyzer (LI-7700; LI-COR Biogeosciences, Lincoln NE, USA). I used a

digital datalogger system (LI-7550A; LI-COR Biogeosciences, Lincoln NE, USA) to record raw turbulence data at 10Hz. At the Permanent Tower I measured air temperature and humidity with an aspirated and shielded thermistor and capacitance sensor (HMP45C; Vaisala, Vantaa, Finland), logged as a 30-minute average of 0.2Hz measurements.

Using standard processing techniques, I used the 10Hz turbulence data to calculate half-hourly fluxes with in-house software written in MATLAB. This software removed artificial data spikes in the 10Hz data (values greater than six standard deviations from the mean in a one-minute window) and values of 10Hz ϱ_{CO2}, ϱ_{H2O}, and ϱ_{CH4} corresponding to diagnostic values that indicated a fouled laser path. I then rotated the x-axis of the 10Hz sonic anemometer data to the mean wind direction in each half-hour window by applying a coordinate rotation to align the mean vertical and lateral velocities to zero. I calculated fluctuations in sonic temperature from fluctuations in speed of sound after accounting for crosswind and humidity effects (Schotanus et al. 1983, Kaimal and Gaynor 1991). For each half hour window of turbulence data, I applied the Webb-Pearman-Leuning correction to account for the effects of air density fluctuations (Webb et al. 1980, Detto and Katul 2007) and I applied the relevant additional spectroscopic corrections for ϱ_{CH4} fluctuations measured with the LI-7700 instrument (McDermitt et al. 2010). After these corrections, I computed the average half-hourly covariance between vertical wind and trace gas density to calculate fluxes of CO_2 ($\mu mol\ m^{-2}s^{-1}$), CH_4 ($nmol\ m^{-2}s^{-1}$), and evaporation ($mmol\ m^{-2}s^{-1}$). I filtered out values with anomalously low ($|uw|<0.02$) turbulence conditions to constrain our analysis to periods where the air near the sensors was well-mixed. During the study period the site experience good and consistent turbulent conditions, and only 7% of half-hourly flux data were removed due to low turbulence. A large period of CH_4 flux data was missing at the Portable Towers early in the growing season due to sensor damage that was subsequently repaired, and a large period of CH_4 flux data are missing in the middle of the growing season at the Permanent Tower due to sensor malfunction.

4.3.3 Satellite imagery classification

For this analysis, I used images collected from the WorldView-2 satellite (DigitalGlobe, Boulder, CO), which are comprised of 8 spectral bands ranging from 400-1040nm with 1.8-2.1m spatial resolution. Images used in this analysis were collected on 19 May 2012, 12 July 2012, 9 August 2012, and 2 September 2012 (hereafter referred to simply by the month of collection). Before classification analysis, the imagery was processed for atmospheric corrections using the Fast Line-of-sight Atmospheric Analysis of Spectral Hypercubes (FLAASH) module based on the MODTRAN4 radiative transfer code in ENVI 4.8 (Exelis, Boulder, CO). All images were then clipped

to the spatial extent of the wetland. Although the images were already georectified, I georegistered all images to the 19 May 2012 image using 25 control points per image located on immobile features like levees and roads to maximize the image-to-image spatial precision for comparative analysis. Prior to image classification for emergent wetland vegetation, I masked all levees and roads using a shapefile created with high-precision GPS by the project engineers who constructed the wetland for the California Department of Water Resources with an additional 2-pixel buffer mask around each levee or road feature. Masking levees prevented erroneous classification of wetland vegetation, as there was some grass and herbaceous vegetation present on levees in the early summer images that might have interfered with classification accuracy.

To classify emergent wetland vegetation, I use the spectral angle mapper (SAM) routine in ENVI. The SAM technique determines the spectral similarity between a reference spectrum and a pixel spectrum by calculating the angle between the two spectra, treating the spectra as vectors in a space with dimensionality equal to the number of bands (in this case, 8). I chose this method since it is relatively insensitive to illumination and albedo effects, and uses the most significant identifying information from all eight spectral bands to separate the image into classes. Within the SAM routine, I defined 4 reflectance classes: water, senescent vegetation, floating aquatic vegetation, and photosynthetic vegetation. I classified both *Schoenoplectus* and *Typha* into a single class because of their similarity in both function and spectral reflectance, since *Schoenoplectus acutus* and *Typha latifolia* share the same growing season and both convectively transport CH_4 from the soil to the atmosphere (Yavitt and Knapp 1995). I identified reference spectra for classification by mapping 3 patches (about 3-5 m in diameter) of each classification type near the permanent eddy covariance tower with a high precision (0.5 m spatial resolution) GPS (Trimble XT; Trimble Navigation Limited, Sunnyvale, CA) on 13 May 2012. I used the same GPS-located shapefiles as reference spectra for all images, as weekly visits to the field site confirmed that the patches did not change class over the duration of this study. Reference spectra for each of the classes followed typical patterns for photosynthetic vegetation, senesced vegetation, and water (Figure 4.2). Within the SAM routine, I defined the maximum distance between the classification pixels and the reflectance spectra as 1 radian.

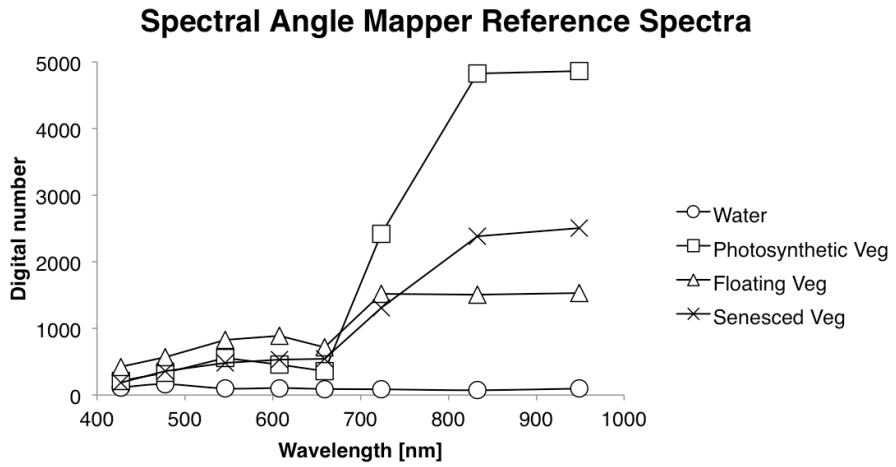

Figure 4.2 Reference reflectance spectra from WorldView-2 imagery for vegetation classification. The WorldView-2 reference spectra for the four classes used in the ENVI Spectral Angle Mapper routine were measured by high-resolution GPS plots on 13 May 2012 at the restored wetland sites in the footprint of the permanent flux tower. Reference spectra showed enough differences among the eight spectral bands, particularly in the infrared bands, to achieve high classification accuracy (see Table 4.1).

I evaluated the accuracy of the SAM classification routine by comparing classified results to ground-truth plots established with high-accuracy GPS on 13 May 2012. Five plots of 3-5m in diameter for each class (separate from the set used as reference spectra) were mapped on 13 May 2012 and were tracked every other week throughout the study period to determine whether or not the plots switched classes over time. The accuracy of our classification was robust, as user's accuracy ranged from 89-98% and producer's accuracy from 87-98% for the four classes defined in this analysis (Table 4.1).

		Reference plots				
		Photosyn. Veg	Aquatic Veg	Senesced Veg	Water	**User's Accuracy (%)**
Classified cells	Photosynthetic Veg	125	12	2	1	89.3
	Aquatic Veg	9	109	4	1	88.6
	Senesced Veg	2	3	75	1	92.6
	Water	1	1	1	137	97.9
	Producer's Accuracy (%)	91.2	87.2	91.5	97.9	

Table 4.1 Accuracy statistics for classification of WorldView-2 imagery into 4 classes. I classified the WorldView-2 satellite imagery by the supervised spectral angle mapper (SAM) routine in ENVI, using endmember spectra outlined in Figure 4.2. Classification accuracy was determined by the collection of five high-accuracy GPS ground plots of 3-5m in diameter within 200m of the tower footprint of each

classification type (separate from the data used for endmember spectra) that were revisited every 2 weeks throughout the study period to determine whether their classification state changed. This table represents the aggregated statistics for classification accuracy across all four images used in this analysis.

4.3.4 Eddy flux footprint model

To model the spatial origin of eddy covariance flux measurements, I used an analytical two-dimensional footprint model (Hsieh et al. 2000, Detto et al. 2006). This footprint model estimates footprint extent and lateral dispersion by a parameterization for different atmospheric stability conditions using friction velocity (u^*; m/s), the Monin-Obukhov atmospheric stability length (L; m), variance in lateral wind (σ_v; m/s), momentum roughness length (z_o; m), and measurement height (z_m; m) as driving variables. The values for u^*, L, and σ_v are calculated directly from the turbulence statistics for each half hour. Since z_o changes as vegetation grows and develops, I used an iterative method to calculate half-hourly z_o for periods of near-neutral stratification ($|z_m/L| < 0.025$) and for high wind speeds (greater than 1m/s) as in Sonnentag *et al.* [2011]. Briefly, this method solves for z_o, canopy height (h; m) and the displacement height (d_o; m) by iterating through the following three equations:

$$(1) \quad z_o = \frac{z_m - d_o}{\exp\left(\frac{\kappa \bar{u}}{u^*}\right)} \qquad (2)\ d_o = 0.66h \qquad (3)\ z_o = 0.1h$$

where κ is the von Karman constant (0.4), $\bar{u}$ is the mean wind speed during the half hour interval (m/s), and u^* and z_m are as above. Since we only solved these equations for near-neutral stability and high wind speeds, we gap-filled values for all half hours where flux measurements were made at the three towers by spline fitting.

This flux footprint model has been tested against several datasets, and in general is succeeds at reproducing the source region for flux measurements at eddy covariance towers in spatially heterogeneous ecosystems (Baldocchi and Rao 1995, Detto et al. 2006). I used the 85% analytical footprint for this analysis (i.e. the areal extent from which 85% of the measured eddy flux originated), since as the analytical footprint approaches 100% the areal extent rapidly expands, although there is in fact a very small contribution to the measured flux from this extensive area.

4.3.5 Fractal analysis of emergent vegetation

I used fractal analysis to characterize the spatial patterns of emergent vegetation within the tower footprints at the three sites. Fractal analysis has a rich history in ecological pattern analysis (Mandelbrot 1983), as fractal theory has been invoked to understand scaling laws for paritioning the aboveground and belowground

components in trees (van Noordwijk and Mulia 2002), characterize leaf area distributions in trees (Jonckheere et al. 2006), and determine the distribution of soil particle size (Montero 2005). Fractal analysis has also been applied to analysis of vegetation patterns at the landscape scale, where it has generally been used as a metric for landscape complexity. To give a few examples, fractals have been used to characterize environmental landscape patterns (Milne 1992), determine spatial scales of anthropogenic deforestation (Krummel et al. 1987), and assess the impacts of landscape connectivity on population distributions (With et al. 1997).

In this analysis, I used the perimeter-area fractal dimension (PAFRAC) to calculate the fractal pattern among emergent vegetation patches within the flux footprint to evaluate spatial complexity. The fractal dimension (D) characterizes the degree of complexity of a two-dimensional polygon by relating the perimeter of a patch (P) to its area (A) by: $\log(P) = \frac{1}{2} D \log(A)$. For simple Euclidean shapes like circles and rectangles, D will tend to one, but for more complex shapes where the perimeter becomes increasingly plane-filling, D will approach 2. Thus, D can well-describe the expansion of emergent vegetation through space; if D is near 1, then P increases more slowly with A (less patch edge with respect to area), whereas if D is closer to 2, that P increases more rapidly as A increases (more patch edge with respect to area). I applied this metric to the population of emergent vegetation patches within each half-hour flux footprint and calculated D by conducting a linear logistic regression of P on A and calculating the slope for footprints with 5 or more emergent vegetation patches to obtain robust regression statistics. For this analysis I only used values of D where the R^2 statistics was greater than 0.95 and the p-value of the regression was below 10^{-5}. It is important to note that no landscape is purely fractal, and for this analysis the spatial resolution of fractal dimension analysis is constrained by the spatial resolution of the satellite imagery, which is 2m.

4.4 Results & Discussion

4.4.1 Comparing measured eddy covariance fluxes

The measured eddy covariance fluxes of CO_2 and CH_4 across the three sites are within the same order of magnitude (Figure 4.3). However, the daytime CO_2 uptake and nighttime CO_2 flux (ecosystem respiration) as well as the maximum CH_4 flux from the Permanent Tower tended to be larger than those at the Portable Tower sites, possibly indicating faster rates of both vegetation and microbial productivity at the Permanent Tower. There is relatively large day-to-day variability in the measured CO_2 and CH_4 fluxes, which I hypothesize is controlled by changes in the flux footprints. There were

no strong seasonal trends in the daily flux measurements as the time series of CO_2 and CH_4 fluxes was stationary, indicating that environmental conditions were relatively stable during the study period. This is further validation that our data were collected at the height of the long California summer growing season, when sunlight was abundant and there were high rates of biogeochemical cycling, although no strong trend across the time series.

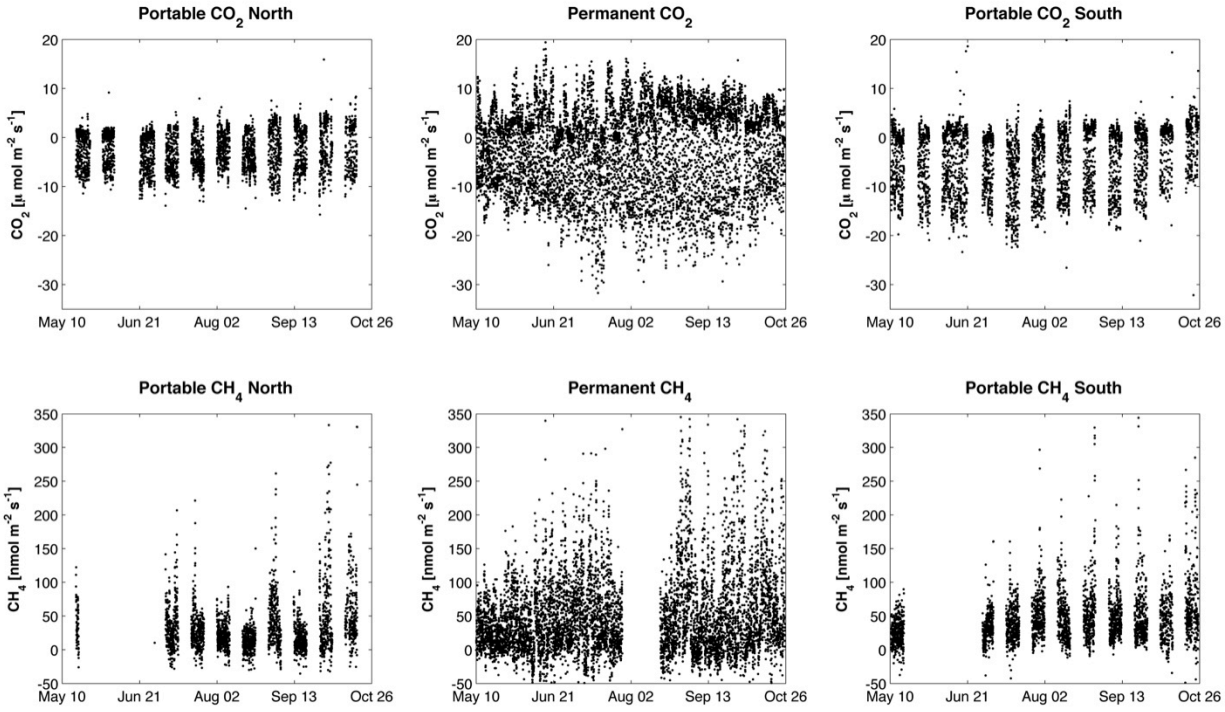

Figure 4.3 Measured half-hourly CO_2 and CH_4 fluxes from the three towers. The measured CO_2 and CH_4 fluxes at all sites generally fall within the same order of magnitude, although there is large variability both within and between sites. Much of the short-term variability in magnitude is due to strong diurnal patterns in both CO_2 and CH_4 fluxes, as most of CH_4 flux is transported convectively from the soil to the atmosphere through plant stomata. There is not an apparent seasonal trend in either the CO_2 or the CH_4 fluxes during the study period, reflecting the fact that these data were collected at the height of the long California summer growing season. There is a large gap in the Permanent Tower CH_4 flux measurements in the middle of the growing season and at the two Portable Towers in the beginning of the growing season due to sensor malfunction. The remaining gaps at the two portable towers correspond to periods when the portable tower was measuring the other portable site.

Although there appears to be large variability in the measured half-hourly CO_2 and CH_4 fluxes, the all three eddy covariance towers demonstrate consistent and well-

constrianed diurnal trends in CO_2 and CH_4 flux controlled by the physiology of plant stomata (Figure 4.4). The pattern in daily CO_2 uptake is controlled by the photosynthetically active period for vegetation that corresponds to the diurnal cycle of incoming solar radiation. The diurnal trend in CH_4 flux is physically linked to plant stomata, as both *Typha* and *Schoenoplectus* convectively transport CH_4 through their porous arenchyma tissue from where it is produced in the soil to the atmosphere. When the stomata open in the morning to begin taking up CO_2 for photosynthesis and transporting O_2 to their roots for respiration, they also begin releasing CH_4 from the soil to the atmosphere.

As the diurnal pattern in the net CO_2 and CH_4 flux measurements are linked through plant physiology, I used this consistent diurnal pattern to test the hypothesis that the amount of vegetation present within the flux tower footprint controlled the daily minimum and maximum magnitude of the fluxes. I focused only on constraining the daily maximum and minimum flux at each site with the footprint and remote sensing imagery since changes in stomatal conductance driven by solar radiation control the regular daily pattern between the maximum and minimum CO_2 and CH_4 flux. Thus, if vegetation abundance and/or spatial patterning within the footprint explains variability in the daily minimum and maximum CO_2 and CH_4 flux, it would be possible to essentially connect the daily maximum and minimum fluxes through curve fitting to approximate diurnal physiology and reconstruct the daily pattern of CO_2 and CH_4 flux.

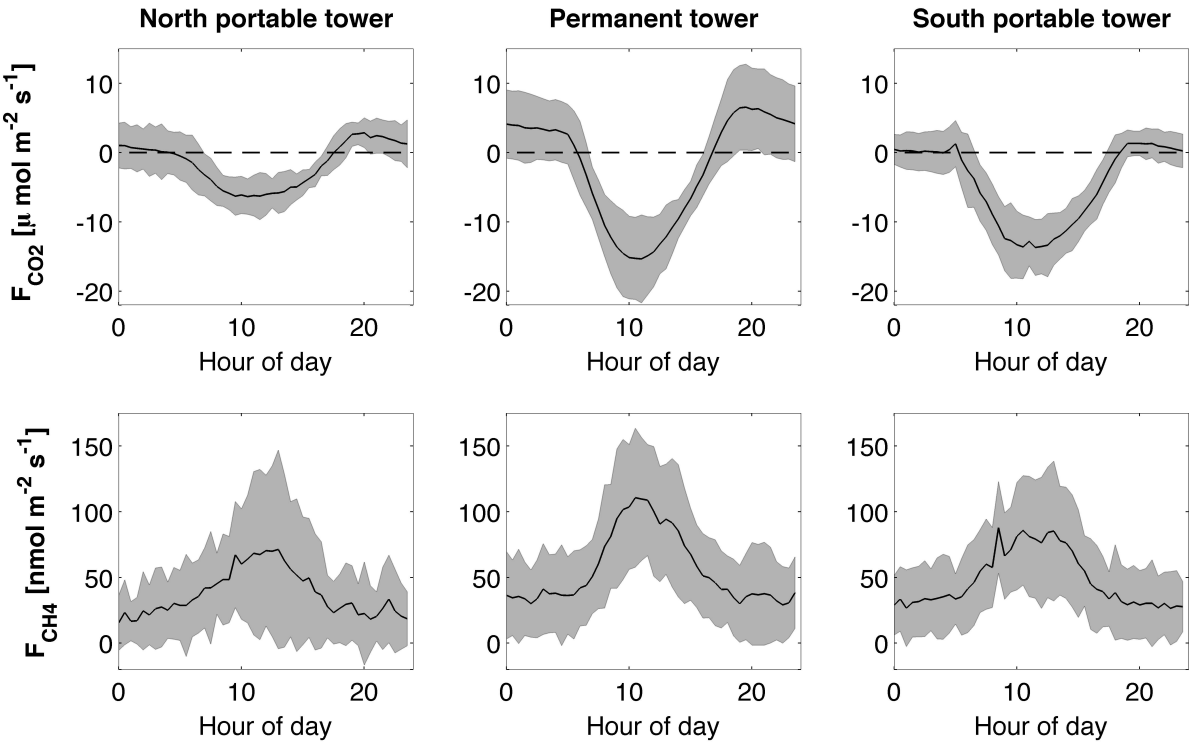

Figure 4.4 Diurnal trends in net CO_2 and CH_4 flux across the study period. Although there is large day-to-day variability in the daily sum of measured CO_2 and CH_4 flux, there are consistent diurnal patterns. These diurnal patterns are controlled by plant physiology at the site, since both *Typha* and *Schoenoplectus* vegetation convectively transport CH_4 from the soil, where it is produced, to the atmosphere.

4.4.2 Trends in flux footprints over the study period

A corresponding flux footprint was modeled for each half-hour when an eddy flux measurement of CO_2 and/or CH_4 was collected. The climatological flux footprints for the study period are stable in direction and do not vary between day and nighttime due to the strong and regular winds through the California Delta during the summertime (Figure 4.5). The mean extent of the climatalogical daytime 85% flux footprints across all three locations is 135m, and the mean extent of the climatological nighttime 85% flux footprints across all three sites is 152m. While the flux footprints at other eddy flux sites around the world are much more variable in time and space (Goeckede et al. 2008), the strong and regular turbulence during the study period at this site constrained the flux footprints in both size and direction. As a result, there are not large geographical shifts in the location of the flux footprints during the duration of the study period.

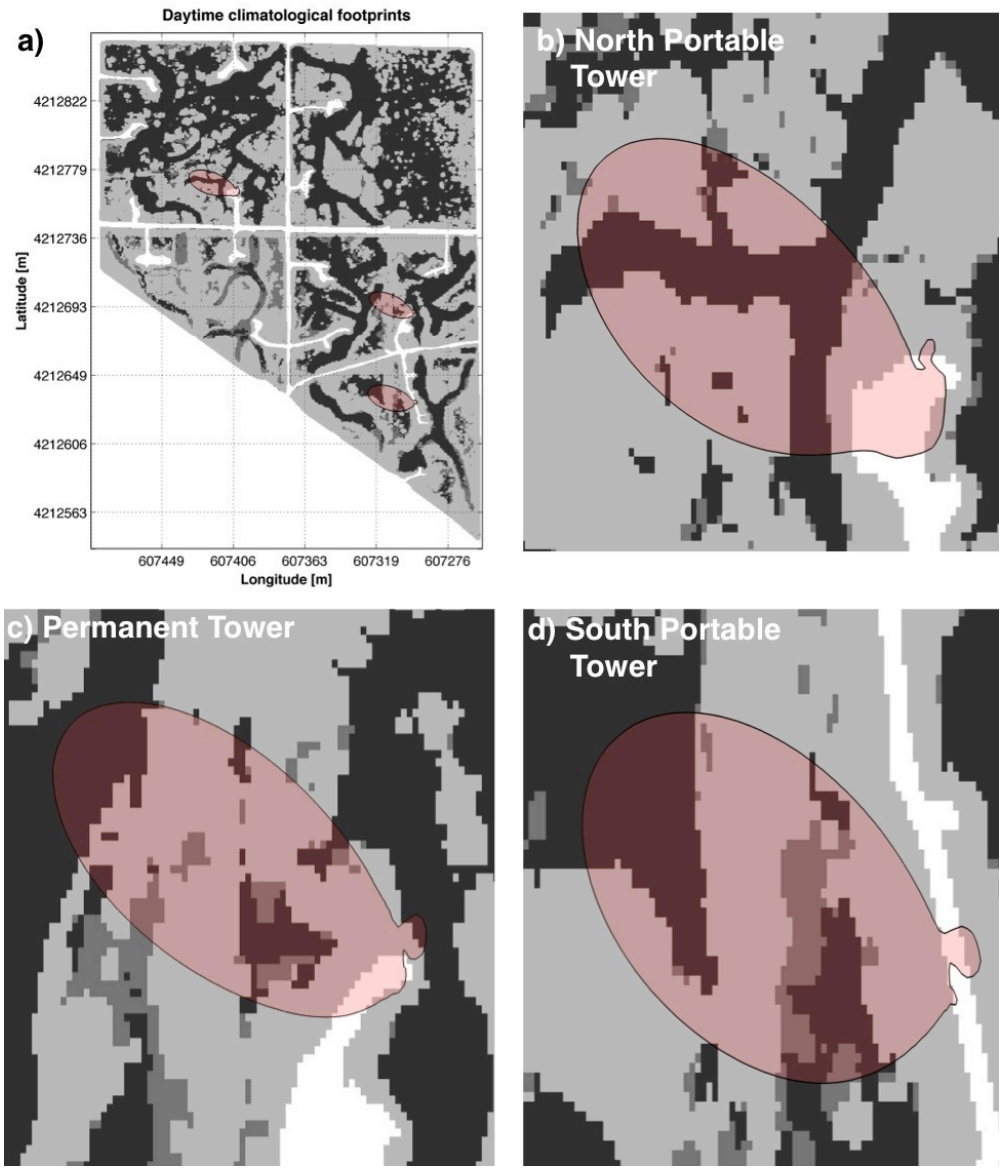

Figure 4.5 Daytime climatological footprints for the three sites. The daytime 85% flux footprints calculated by the two-dimensional analytical footprint model are displayed in red, overlaid on the classified September 2012 WorldView-2 image. White areas are berms (above the water surface), light grey is emergent vegetation, dark grey is floating aquatic vegetation, and black is open water. The flux footprints are only displayed for daytime measurements, since nighttime climatological footprints were essentially identical due to strong and regular turbulence during the study period.

At all three of the tower locations, the mean fraction of vegetation within the flux footprint increased throughout the summer growing season (Figure 4.6a-c). The flux footprints at all three sites contained between 20-30% emergent photosynthetic vegetation in May, which more than doubled by the end of the study period in

September. The fraction vegetation within the flux footprints at the North Portable Tower site increased the least over the growing season, and by September the flux footprints at the site were about half emergent vegetation and half open water. The vegetation within the Permanent Tower footprint expanded the most over the study period, increasing from a mean emergent vegetation fraction of 0.25 in May to a mean of 0.7 in September. The fraction of emergent vegetation within the flux footprints at the South Portable tower expanded a moderate amount, from about 0.3 in May to a mean of 0.62 in September.

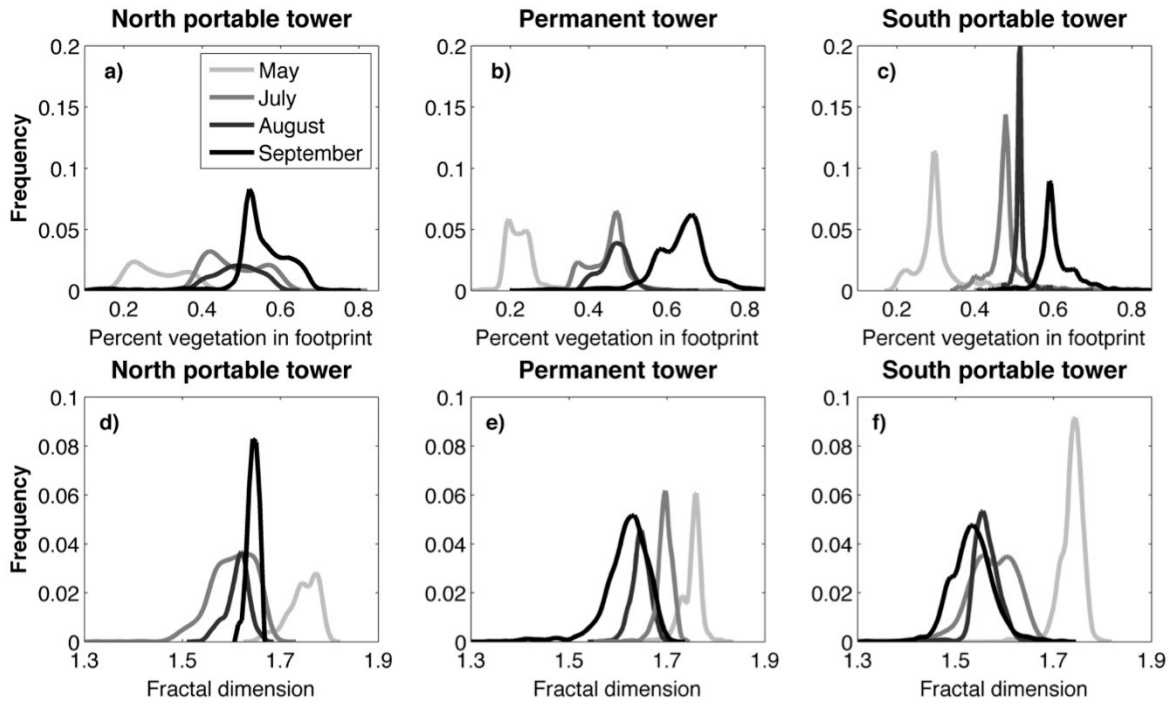

Figure 4.6 Mean temporal trends in emergent vegetation abundance and fractal dimension in tower footprints through study period. a-c) Across all three sites, the percent vegetation within the measured flux footprint increased throughout the summer growing season. The largest increase in vegetation growth occurred at the Permanent Tower site. While the Permanent Tower flux footprint became more stable in the vegetation abundance within the flux footprint over time (i.e. the distribution narrows) both the North and South Portable Tower sites show increasing variability in vegetation abundance over time (i.e. the distribution widens). **d-f)** At all three sites, the fractal dimension of vegetation patches within the tower footprint decreased over the summer growing season. By the end of the growing season, the Permanent tower site had the highest fractal dimension, while the North and South Portable Tower footprints demonstrated more variability in fractal dimension.

The mean fractal dimension of the emergent vegetation patches within the flux footprints decreased and became more variable over the study period (Figure 4.6d-f). However, the emergent vegetation patterns within the flux footprints were all still significantly fractal by September. In May, the pattern of emergent vegetation within all three sites had a highly fractal structure, as the fractal dimension was near 1.75 (a fractal dimension of 2 is a perfect complex fractal). As the growing season progressed, the fractal dimension at all sites decreased, forming less complex and more geometric shapes, although the footprints still remained fractal in composition. This decrease in the fractal dimension indicates that the pattern of vegetation growth at all three sites occurred in a way where the perimeter of emergent vegetation patches grew more slowly with respect to the patch area, forming more regular circular shapes over time. The North Portable site had the smallest decline in fractal dimension, from 1.75 in May to 1.65 in September. The South Portable site had the largest decline in fractal dimension over the study period, from a mean of 1.75 in May to 1.51 in September. And the Permanent Tower site had a moderate decline in fractal dimension from 1.75 in May to 1.62 in September. Thus, although the fraction of emergent vegetation within the Permanent Tower flux footprints grew the most over the study period, the growth patterns occurred in a way that preserved the complex fractal nature of the vegetated landscape, especially compared with the South Portable tower site.

The concurrent changes in both vegetation abundance and the structure of emergent vegetation within the flux tower footprints yields insight into differences among the landscape-scale vegetation dynamics operating at the three sites. At the South Portable Tower site, the amount of vegetation increased a moderate amount during the study period, while the fractal dimension significantly decreased and became more variable. This indicates that the emergent vegetation growth within the South Portable tower footprint during the study period occurred in a way that geometrically expanded and filled-in vegetation patches on the landscape, creating shapes with lower perimeter to area ratios. Conceptually, this can be thought of as complex patches merging together to form more regular shapes, or a complex shape growing to a larger, more rotund shape.

At the Permanent Tower site, the fraction of the flux footprint covered by emergent vegetation expanded a very large amount during the growing season, but a relatively high fractal dimension was preserved compared with the other two sites. This indicates that the emergent vegetation patches at the Permanent Tower site expanded in ways that preserved shape complexity, increasing their patch perimeter at a faster rate than the concomitant increase in patch area. At the North Portable Tower site, vegetation abundance increased a small amount, but the fractal dimension remained high through the end of the study period. This indicates that the vegetation growth that

occurred on the landscape preserved the spatial complexity of emergent vegetation patch shapes. The changes in both vegetation abundance and complexity within the three sites in this study are likely controlled by landscape-scale resource patterns such as light and nutrients, or could also reflect bathymetry and water depth limitations. It's worth noting that this analysis only examines changes in the aboveground components of emergent wetland vegetation, and a significant portion of wetland plant biomass occurs belowground, which is not captured by satellite imagery.

The spatial patterns of emergent vegetation abundance and structure within flux footprints also highlight important changes within individual wind direction sectors at each of the eddy flux towers (Figure 4.7). As in Figure 4.6, the percent vegetation within the flux footprints increased throughout the study period across all three sites, but the magnitude of increase was not uniform across all wind directions (Figure 4.7a-c). Complexities in the temporal and spatial dimensions of vegetation growth within this heterogeneous landscape highlight the need for two-dimensional footprint modeling in order to capture changes in the flux footprints. The fraction of vegetation within the May flux footprints at the North Portable Tower were non-uniform in direction, as the vegetation fraction at 260° from the flux tower was near 0.4 while the percent of vegetation at 300° was about 0.2 (Figure 4.7a). However by September, the fraction of vegetation at the North Portable tower was much more uniform between 270-300°, indicating in-filling of emergent vegetation between these wind direction sectors.

At the Permanent Tower, vegetation growth was also non-uniform in direction, as the vegetation fraction near 300° increased from 0.35 in May to 0.6 in September, whereas the fraction vegetation near 285° increased from 0.1 to 0.9 during this same time period (Figure 4.7b). This indicates not only in-filling, but also extensive expansion of existing patches of emergent vegetation within the 385° wind sector during the study period. Changes in the vegetation fraction at the South Portable Tower site were perhaps the most spatially uniform among the three sites, as the fraction of emergent vegetation increased about 20-30% from May to September in all directions, indicating mostly in-filling of existing vegetation patches (Figure 4.7c).

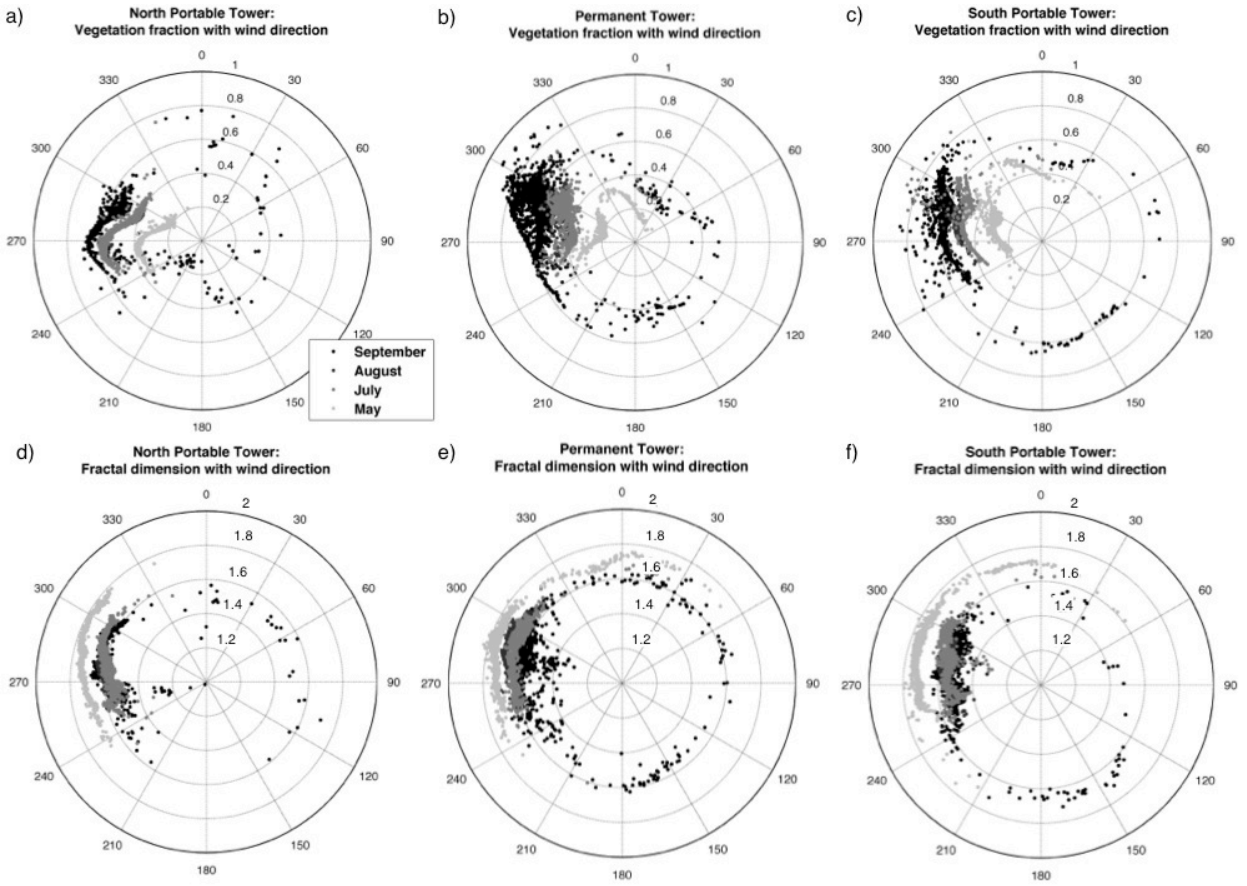

Figure 4.7 Mean spatial trends in emergent vegetation abundance and fractal dimension in tower footprints through study period. a-c) The percent vegetation in the tower footprint increased across all three sites during the study period, but the spatial patterns of growth differed between sites. At the North Portable Tower, the most frequent wind directions had the lowest vegetation growth of the three sites. There was rapid vegetation growth in the Permanent Tower predominant wind directions, and moderate growth at the South Portable Tower. **d-f)** The fractal dimension across all three sites decreased throughout the study period, as vegetation filled in, making more contiguous geometric shapes. There was some spatial directional variability in the fractal dimension across sites, but in general there was more variation across time than through space.

Spatial changes in the fractal dimension of the flux footprints at the three sites were more subtle than changes in the vegetation abundance (Figure 4.7d-f). At the North Portable Tower, the increase in fraction vegetation near 270° was mirrored by a decrease in the fractal dimension from 1.8 to 1.5, indicative of an in-filling process that merged existing vegetation patches into more geometric shapes (Figure 4.7d). There was a slight decline in fractal dimension over time at the Permanent Tower, and by September the fractal dimension was slightly more variable although still relatively high, with a mean of 1.61 (Figure 4.7e). The fractal dimension across all wind directions

at the South Portable Tower experienced a significant decline from May to September, particularly within the wind sector near 270°, which fell from a mean of 1.78 in May to 1.48 in September (Figure 4.7f). Like the dynamics at the North Portable Tower, this large decline in fractal dimension along with an increase in the fraction of vegetation is indicative of an in-filling process, rather than the growth of new vegetation patches within the flux footprints.

This spatial and temporal footprint analysis highlights important landscape-scale processes controlling the growth of new emergent wetland vegetation. The three sites exhibited clear differences in the fraction and spatial pattern of emergent vegetation within the flux footprints over the summer growing season. The South Portable Tower site experienced a moderate increase in vegetation abundance accompanied by a large decrease in the fractal dimension, indicative of an in-filling process. The North Portable Tower site had a small increase in vegetation abundance, but maintained a high degree of fractal structure throughout the study period. The Permanent Tower site had a very large increase in emergent vegetation abundance while maintaining a higher fractal dimension the South Portable Tower site, suggesting a process of patch growth into more complex shapes and the formation of new complex patches.

4.4.3 Impacts of vegetation abundance and structure on CO_2 and CH_4 fluxes

To examine the interactions between emergent vegetation abundance and fractal dimension and the magnitude of the measured CO_2 and CH_4 fluxes, I extracted these variables for the daily flux maximum and minimum at each of the three sites. As outlined in section 4.4.1, all three sites demonstrate a strong diurnal pattern in both CO_2 and CH_4 flux that is controlled by plant physiology, where the CO_2 flux minimum occurs near midday (maximum CO_2 uptake) and the maximum CO_2 flux occurs at nighttime. Conversely, the CH_4 maximum occurs near midday as plants with open stomata convectively transport CH_4 from the soil to the atmosphere, and the minimum CH_4 flux occurs at nighttime when plant stomata are closed (Figure 4.4). I focused only on fluxes at these key timepoints since the diurnal pattern otherwise follows a predictable pattern that essentially connect the daily maximum and minimum.

Both the footprint vegetation abundance and fractal dimension are important explanatory variables driving the maximum daily CH_4 flux across all three sites (Figure 4.8a). The daily maxima across the three sites ranges from 20.5 nmol $m^{-2}s^{-1}$ to 506 nmol $m^{-2}s^{-1}$ during the summer growing season, where the maximum daily flux is clearly correlated with footprints that have high vegetation abundance and a lower fractal index. This indicates that large vegetation patches with a smaller perimeter to area ratio

(fewer edges) supported the highest rates of CH_4 flux to the atmosphere. A mechanism that might explain this phenomenon is that emergent vegetation patches with a more contiguous area and fewer edges are less likely to laterally leak labile carbon from the rhizosphere to the surrounding unvegetated areas, where it is less likely to be respired since microbial populations are lower outside the rhizosphere. Thus, large, contiguous patches of emergent vegetation are hotspots in the landscape for CH_4 flux. There is also a clear turning point for maximum daily CH_4 flux at an emergent vegetation fraction of 0.75, where the maximum daily CH_4 flux increases rapidly.

There is little pattern between the minimum daily CH_4 flux and the fraction vegetation and fractal dimension, although there is as slight trend where footprints with higher fraction vegetation have higher minimum daily CH_4 flux (Figure 4.8b). This low correlation is likely due to the fact that there is much lower variability both temporally and among sites in the minimum daily CH_4 flux since it is near zero at all sites. The lack of a clear correlation between emergent vegetation and nighttime CH_4 flux could also result from the dominance of physical transport processes at nighttime, such as convective transport through the water column, that could be decoupled from vegetation patterns on the landscape.

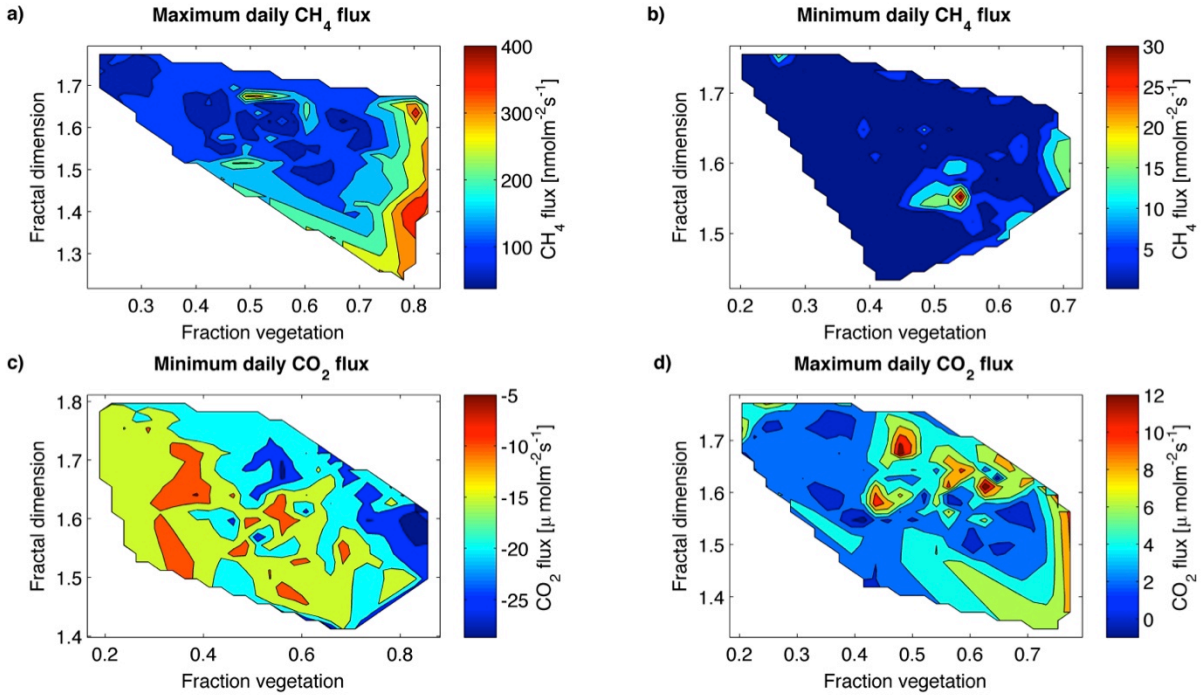

Figure 4.8 Interactions between fraction vegetation, fractal dimension, and flux magnitude within measured flux footprints. a) There is a clear and consistent relationship between the fraction of

vegetation and the fractal dimension of vegetation patches within the flux footprint and the maximum daily CH_4 flux. The highest CH_4 flux occurs in areas with a high abundance of vegetation and a low fractal dimension. **b)** There is no clear pattern between the flux footprint vegetation variables and the minimum daily CH_4 flux, likely because the minimum flux is near zero each day and shows very little variability over the growing season and among sites. **c)** There is a consistent pattern between the footprint vegetation variables, as more CO_2 uptake (a lower minimum daily CO_2 flux) occurs in areas with more vegetation and with a higher fractal dimension. **d)** The correlation between the maximum daily CO_2 flux and the vegetation parameters approximately mirrors that of the minimum daily CO_2 flux, indicating correlation between ecosystem productivity and respiration.

The minimum daily CO_2 flux (maximum CO_2 uptake by vegetation) also shows consistent correlation with both the abundance of vegetation in the tower footprint and the fractal dimension of the vegetation patterns. The lowest minimum CO_2 flux occurs in footprints with high vegetation abundance and at high fractal dimensions (Figure 4.8c). The direct connection between the abundance of vegetation and minimum CO_2 flux is clear since plants are the only organisms within the landscape that consume CO_2. Larger CO_2 uptake occurs at higher fractal dimensions of vegetation patches (more complex shapes with more edges) likely due the effects of competition for light, often the limiting resource in productive wetland ecosystems (Brinson et al. 1981, Rocha and Goulden 2009). For complex vegetation patches with more edges (i.e. a fractal dimension closer to 2), there is higher light penetration into the canopy and more light available per individual stem, and thus increased productivity indicated by higher CO_2 uptake.

The interactions between emergent vegetation abundance and patterning and the maximum daily CO_2 flux somewhat parallel the patterns for the minimum daily CO_2 flux, indicating that productivity and respiration are coupled in this wetland (Figure 4.8d). However, the large variation in nighttime maximum CO_2 flux is better explained by changes in air temperature, as high temperatures promote both microbial activity and increased diffusion of CO_2 through the water column. There is a strong linear relationship between nighttime maximum CO_2 flux and air temperature at the time of this maximum CO_2 flux (Figure 4.9a). Although the vegetation fraction in the tower footprint helps to explain a bit more of the variability in the maximum nighttime CO_2 flux, it is clear that variations in temperature are driving most of the variation in this maximum CO_2 flux value (Figure 4.9b). This indicates that ecosystem respiration is mildly coupled with vegetation at this restored wetland, but that microbial respiration and CO_2 transport are more tightly coupled with changes in temperature than changes in plant productivity. Although this pattern exists for maximum nighttime CO_2 flux, there is not a similar correlation for the minimum nighttime CH_4 flux. The lack of a correlation between air temperature and daily nighttime CH_4 flux could indicate the

dominance of plant-mediated CH_4 transport, or that nighttime CH_4 is transported through more complex pathways, such as convection or ebullition.

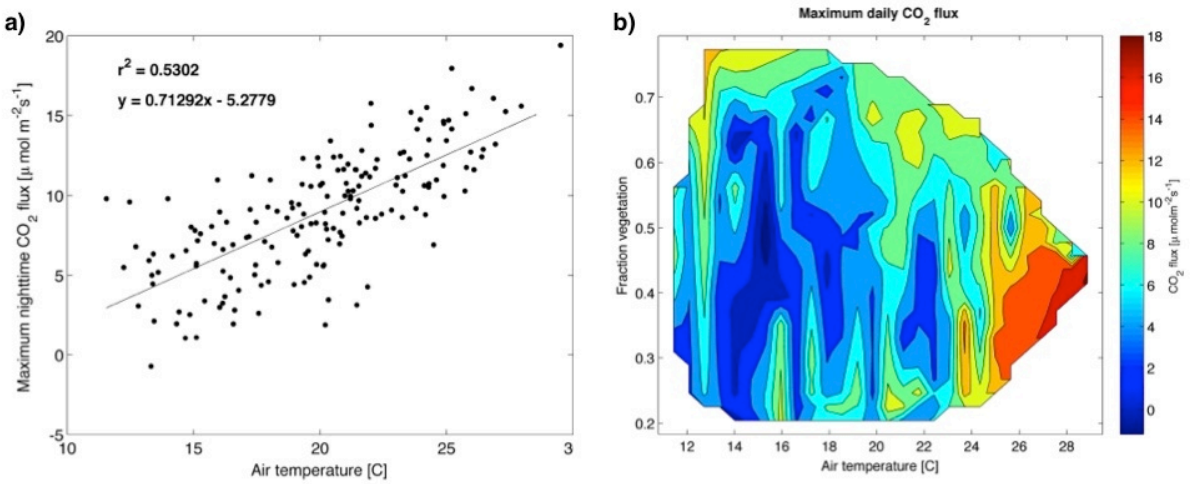

Figure 4.9 Relationship between nighttime maximum CO_2 flux and air temperature. a) There is a strong (r^2>0.5) positive linear relationship between the maximum nighttime CO_2 flux and air temperature at the time of maximum CO_2 flux across all three sites. This relationship likely explains the combined impact of higher microbial respiration rates at higher temperatures as well as higher diffusive flux rates through the water column at higher temperatures. **b)** The three-dimensional plot between the maximum daily CO_2 flux, air temperature at the time of this flux, and the fraction of vegetation in the tower footprint again highlights the strong relationship between air temperature and maximum daily CO_2 flux. Although footprints with a high vegetation fraction also tend to have higher maximum CO_2 flux, the relationship is not as strong and consistent as that with air temperature.

These consistent relationships between the maximum daily CH_4 flux and both minimum and maximum daily CO_2 flux have important implications for developing management techniques to maximize CO_2 uptake and minimize CH_4 release in restored wetlands. These data indicate that the ideal scenario for maximum CO_2 uptake and minimal CH_4 release is a landscape with a moderate abundance of vegetation and a high spatial complexity. However, the maximum daily CO_2 release (nighttime respiration) is also correlated with the CO_2 uptake, so understanding the balance between these two fluxes is necessary for determining the net CO_2 uptake. To minimize CH_4 release at this wetland, managers might take actions to preserve the structural complexity of vegetation patches on the landscape by maximizing the patch perimeter to area relationship, since large and spatially simple vegetation patches emitted the highest fluxes of CH_4 to the atmosphere. Minimizing the loss of nighttime CO_2 by

ecosystem respiration might not be easily manipulated by management actions due to a tight correlation between maximum daily CO_2 flux and air temperature.

As previously mentioned, spatial complexity of wetland vegetation is also considered a keystone structure that can enhance habitat diversity, and as a result, biodiversity (Tews et al. 2004). Other research has demonstrated that restored wetlands negatively impacted by anthropogenic influence have less complex spatial patterns at all scales, so spatial complexity might also help to preserve wetland ecosystem resilience (King et al. 2004, Foti et al. 2013). Thus, developing management actions to preserve fractal landscape complexity in order to minimize CH_4 flux to the atmosphere and maximize CO_2 uptake might also have additional co-benefits of preserving habitat diversity and maintaining ecosystem health.

5. Conclusions

While the half-hourly flux time series of CO_2 and CH_4 appeared highly variable over the course of the summer growing season, much of the variability in the daily flux maxima and minima could be attributed to changes in the fraction of vegetation and complexity of the plant patches within the flux footprint. The highest CH_4 fluxes occurred in footprints with a high fraction of vegetation and low spatial complexity. The daily maximum CO_2 uptake (minimum CO_2 flux) was found in footprints with high vegetation abundance and a higher fractal dimension, indicating complex vegetation patterning. This analysis indicates that large and simple geometric patches of vegetation are hotspots for CH_4 release on the landscape, whereas large and complex geometric vegetation patches are the strongest CO_2 sinks. Air temperature was the strongest driver for maximum daily CO_2 flux, so management actions might be less successful at reducing this flux to the atmosphere.

The impact of vegetation abundance and structural complexity on the resulting CO_2 and CH_4 fluxes yields important considerations for the management of these landscapes as long-term ecological carbon sinks. Restored wetlands have been identified as potential carbon sinks on a long timescale (Miller et al. 2008), however the mechanisms that lead to maximum CO_2 uptake and minimum CH_4 release remain untested. The results of this analysis indicate that an ideal landscape for maximizing CO_2 uptake while minimizing CH_4 release would have a moderately high fraction of vegetation, but arranged on the landscape in complex shapes. Landscapes with increased fractal complexity within this restored wetland ecosystem acted to minimize the maximum daily CH_4 flux to the atmosphere while maximizing the daily uptake of CO_2. While further study is required to see if this pattern holds over many years and

other sites, this is a promising scaling mechanism for engineering restored wetlands for ecosystem carbon sequestration in the future.

Chapter 5: Near-surface hyperspectral reflectance tracks ecosystem productivity in three structurally similar yet functionally diverse California ecosystems

5.1 Abstract

The absorption and reflection of energy from plant canopies can provide detailed information about vegetation physiology, and through this connection, reflectance can track ecosystem-atmosphere CO_2 fluxes. This analysis investigated connections between canopy hyperspectral reflectance from 400-900nm and measures of ecosystem productivity, including gross ecosystem productivity measured by eddy covariance, leaf area index, and foliar nitrogen content, from 2006-2012 at three California ecosystems: a semi-arid annual grassland, a drained peatland pasture vegetated with the invasive pepperweed plant, and an irrigated rice paddy. This set of structurally similar yet functionally diverse ecosystems provided a unique comparison between canopy reflectance and ecosystem productivity. The traditional normalized difference vegetation index (NDVI) best captured trends in gross ecosystem productivity, light use efficiency, and leaf area index across all sites. However, at the pepperweed pasture site productivity was less correlated with canopy reflectance due to the complex phenology of the pepperweed plant and high contribution from heterotrophic respiration at the site. This analysis also investigated and proposed new potential normalized spectral indices for the monitoring of net and partitioned CO_2 fluxes, leaf area index, and foliar nitrogen content across the three sites.

5.2 Introduction

The development of remote sensing metrics that can bridge the scale of carbon flux measurements from individual sites or eddy covariance towers to broader, continuous spatial scales has long been a goal of the earth systems science community (Bauer 1975, Running et al. 1999, Ustin et al. 2004). Near-surface ground reflectance measurements provide an important link between the spatial scales of eddy flux towers and aircraft or satellite measurements, and can yield important insights for variation in measured CO_2 fluxes (Gamon et al. 2006, Inoue et al. 2008, Gamon et al. 2010). Furthermore, data from near-surface hyperspectral reflectance measurements can be used to highlight particular spectral reflectance indices that are correlated with ecosystem productivity that might be used in the future to monitor canopy phenology with relatively inexpensive LED sensors (Ryu et al. 2010a).

Canopy reflectance metrics can be used as proxies for biological processes at the surface when those biological processes have correlating features that change the reflectance and absorption of energy in the plant canopy. The two most commonly used remote sensing metrics, the normalized difference vegetation index (NDVI) and the related enhanced vegetation index (EVI), track ecosystem productivity by measuring broad-band energy absorption at the visible wavelengths where chlorophyll is active and comparing that to the reflectance or emission at near-infrared wavelengths where active plant canopies dissipate energy (Rouse et al. 1973, Liu and Huete 1995). Another reason for the widespread use of NDVI and EVI is that they can be calculated worldwide (although at coarse spatial resolution of about 250m) by reflectance measurements from the MODIS satellite system. Another common canopy reflectance metric, the photochemical reflectance index (PRI), uses narrow-band reflectance from carotenoid pigments in the green region of the spectrum, which have been correlated with light-use efficiency in plants (Gamon et al. 1992). Although it is more difficult to calculate PRI over large areas from satellite platforms, it has successfully been used to track ecosystems experiencing stress and corresponding declines in productivity (Gamon et al. 1997).

This analysis examined the connection between hyperspectral reflectance and landscape-scale CO_2 fluxes by using measurements from a network of three sites in Northern California with similar canopy architecture but diverse ecophysiology: a semi-arid annual grassland, a peatland pasture invaded by pepperweed (*Lepidium latifolium*), and an irrigated rice paddy. The unique hydrological controls on ecophysiology at each site also control the degree to which gross ecosystem photosynthesis (GEP) is coupled with ecosystem respiration (R_{eco}). At the annual grassland, GEP and R_{eco} are closely connected, as the growing season during the winter and spring correspond to the rainy season, causing both CO_2 uptake in plants and CO_2 release through root and microbial respiration. At the rice paddy, GEP and R_{eco} are also temporally coupled as fresh photosynthates released to the soil stimulate some decomposition during the summer, but heterotrophic respiration of soil carbon is minimized due to flooded conditions. At the drained peatland pasture, GEP and R_{eco} are more decoupled, as there is a large contribution to R_{eco} from heterotrophic decomposition of peat soil carbon throughout the year. Thus, these three sites provided a spectrum of GEP/R_{eco} coupling for testing the ability of spectral canopy reflectance to capture trends in both net and partitioned biosphere-atmosphere CO_2 exchange.

Each of these three sites has an active eddy flux tower measuring net carbon dioxide fluxes where ground hyperspectral reflectance from 400-900nm were collected in the tower footprints from 2006-2012 at the annual grassland, from 2007-2012 at the degraded pepperweed pasture, and from 2009-2012 at the rice paddy. This rich dataset

included multiple replicate measurements within the tower footprint on each sampling date, and the extensive temporal coverage yields insight into long-term inter-annual drivers of both canopy reflectance and carbon dioxide flux. Many researchers have demonstrated that canopy geometry is an important factor impacting reflectance measurements (Colwell 1974), but in this comparison the vegetation in all three ecosystems is erectophile in leaf angle distribution and has nearly identical canopy structure during the growing season, with the exclusion of the bright white flowers of the pepperweed plant when in bloom. Due to similarities in canopy architecture among sites, this analysis focused on the ability of canopy reflectance metrics to translate across ecophysiological boundaries and hold in a functionally diverse set of ecosystems.

I used this extensive long-term dataset to motivate the following questions:

1) How do the hyperspectral reflectance and traditional remote sensing reflectance indices vary seasonally within sites?
2) Can traditional reflectance indices like NDVI, EVI, and PRI capture seasonal patterns in CO_2 fluxes, light-use efficiency, and leaf area index across the three sites?
3) Are there other, more ideal spectral indices that correlate with CO_2 flux measurements, leaf area index, and foliar nitrogen?
4) What physiological drivers are producing these correlations between reflectance and ecosystem productivity, and how do they vary among sites?

This long-term near-surface hyperspectral reflectance dataset collected in conjunction with CO_2 flux measurements provided a broad set of conditions to test existing and new reflectance indices that can capture trends in net and partitioned CO_2 fluxes. Although the ecosystems analyzed here are relatively structurally simple, they are similar to other rangelands, managed pastures, and croplands that now cover over 40% of the Earth's surface (Foley et al. 2005). As there is rapidly growing interest in monitoring carbon budgets for managed ecosystems worldwide, the canopy reflectance metrics presented here can serve as a tool for making spatially intensive measurements with near-surface reflectance sensors or aircraft/satellite imagery as a proxy for the ecosystem carbon balance.

5.3 Methods

5.3.1 Site characteristics

I collected hyperspectral plant canopy reflectance measurements at three sites in Northern California with similarly structured, yet functionally diverse plant canopies. The first site is a semi-arid annual grassland in the lower foothills of the Sierra Nevada Mountains near Ione, CA (latitude: 38.4133N; longitude: 120.9508W; altitude: 129m). The second site is a drained peatland pasture located on Sherman Island in the Sacramento-San Joaquin Delta (latitude: 38.0373; longitude: -121.7536; altitude: -4m) with annual grasses growing during the winter and spring, and the invasive perennial pepperweed plant (*Lepidium latifolium*) active from spring through autumn. The third site is a rice paddy located on Twitchell Island in the Sacramento-San Joaquin Delta (latitude: 38.1087°N, longitude: 121.6530°W; altitude: -4.5m) with an active growing season from May through October and a fallow field for the remainder of the year. The semi-arid annual grassland, degraded pasture, and rice paddy are all active Ameriflux sites (site codes, respectively: US-Var, US-Snd, US-Twt) where fluxes of energy, water vapor, and carbon dioxide have been measured since 2000 at the grassland, since 2007 at the degraded pasture, and since 2009 at the rice paddy.

All three sites experience a Mediterranean climate with hot and dry summer months and a rainy cool winter. However, the sites differ dramatically in belowground hydrology, and as a result the plant communities at each site demonstrate a diverse set of ecophysiological characteristics. The annual grassland site is truly semi-arid, as the water table is several meters below the soil surface and the annual grasses that compose the canopy senesce after the last spring rainfall, and remain inactive until the return of autumn precipitation. The water table at the pepperweed pasture is always below the soil surface, although it is much shallower, at 50-80cm. Although the phenology of grasses at the peatland pasture site follows approximately the same pattern as the annual grassland, the pepperweed plants remain relatively active over the summer as their roots can tap the shallow water table. The rice paddy site is flooded through irrigation management during the hot summer months, so the plant canopy maintains high productivity during the hottest but precipitation-free summer months, and flooding reduces heterotrophic soil respiration.

5.3.2 Spectrometer measurements

Hyperspectral ground reflectance was collected with a fiber optic spectrometer (USB 2000; Ocean Optics, Dunedin, FL) with a detector range from 200-1100nm, and for this analysis we constrained our data to 400-900nm due to larger noise at the detection edges. The spectrometer was mounted on a tripod approximately one meter above the canopy and was connected via USB cable to a laptop computer running the OOBase32 software (USB 2000; Ocean Optics, Dunedin, FL), which internally corrected for

instrument-specific calibration parameters. Each spectrum was collected and saved by OOBase32. At the start of each site visit, the integration time within OOBase32 was adjusted appropriately to the ambient light conditions and a reference dark spectrum measurement was collected by covering the fiber optic head with two layers of black electrical tape.

After this initial set-up, reflectance spectra were collected for each replicate at each site by first pointing the spectrometer directly skyward to record the spectrum of incoming energy, and then pointing the spectrometer directly at the ground surface to record the spectrum of reflected energy. Thus the reflectance for each replicate was calculated as the reflected spectrum normalized by the incoming spectrum. For each collection date at each site, we averaged the replicate spectra for this analysis to compute a single mean spectral reflectance per date at each site. The spectrometer records data at approximately 0.28nm intervals, and we smoothed the average spectrum using a spline fit to 1nm intervals between 400-900nm in order to reduce instrumental noise in the data, particularly in the near infrared range.

Hyperspectral reflectance measurements were collected at each site with a sampling and replicate frequency that was suited to the individual site canopy characteristics. At the grassland, which has low spatial variability and a very predictable growing season governed by the semi-arid climate in California, reflectance measurements were collected approximately bi-weekly during the growing season and otherwise bi-monthly, with 2-3 replicate locations randomly sampled during each visit since 2006. At the pepperweed pasture, where the canopy is more spatially and temporally heterogeneous, hyperspectral reflectance was measured approximately weekly, bi-weekly, or monthly since 2007, with 9 replicate locations randomly sampled per visit. At the rice paddy, which has moderate spatial variability, hyperspectral reflectance was collected weekly or bi-weekly during the growing season, with 5 replicate reflectance spectra collected per visit. In general, the repeated measurements well sampled the entire period when a canopy layer is present across all three sites (Figure 5.1). Ground hyperspectral reflectance was captured on a total of 81 days from 2006-2012 at the annual grassland, 109 days from 2007-2012 at the degraded pepperweed pasture, and 45 days from 2009-2012 at the rice paddy.

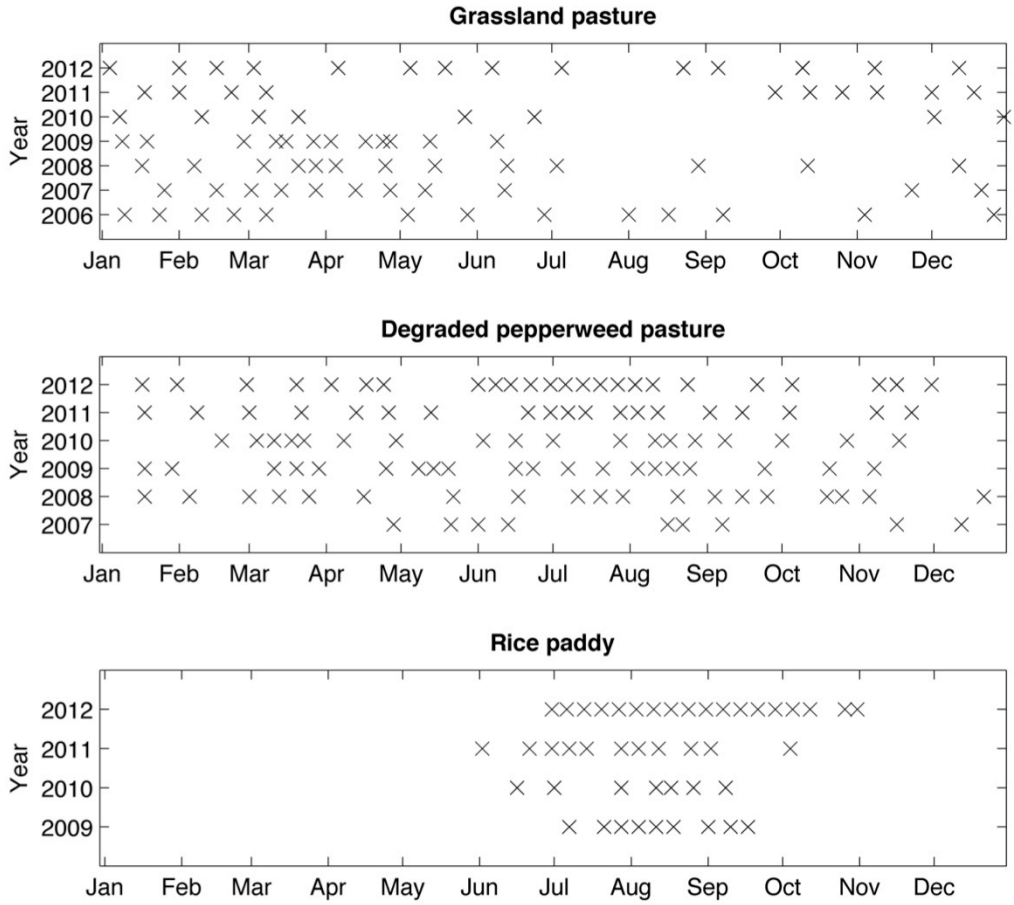

Figure 5.1 Dates of hyperspectral reflectance collection at the three sites. Sampling frequency for each of the three sites, where each 'x' represents one sampling date on which multiple replicates of hyperspectral ground reflectance were collected.

5.3.3 Traditional reflectance indices used as proxies for photosynthesis

A small set of normalized spectral reflectance indices are commonly used as proxies for gross ecosystem productivity, canopy light-use efficiency, or leaf area index that utilize reflectance measurements in the visible and near-infrared range. The use of normalized spectral indices is much more common than direct ratios in remote sensing measurements since normalization helps to correct for differences in the solar azimuth angle between sampling dates (Kriegler et al. 1969). The first two traditional reflectance metrics approximate photosynthetic activity by measuring reflectance at the absorption wavelengths for chlorophyll and the reflectance wavelengths for near-infrared light: 1) the normalized-difference vegetation index (NDVI) (Rouse et al. 1973), and 2) the enhanced vegetation index (EVI), which is similar to NDVI but reduces the saturation effects at high leaf area indices and high photosynthetic rates (Liu and Huete 1995, Jiang

et al. 2008). The photochemical reflectance index (PRI) is also used as a proxy for photosynthetic activity, but through the measurement or carotenoid pigments, which are indicators of light-use efficiency (Gamon et al. 1992). The specific wavelengths and formulae used to calculate these indices are included as Table 5.1.

Name	Formula	Range	On satellite platforms
Normalized difference vegetation index (NDVI)	$\frac{R_{860nm} - R_{670nm}}{R_{860nm} + R_{670nm}}$	0 – 1	Landsat, MODIS
2-band Enhanced vegetation index (EVI)	$2.5\frac{R_{860nm} - R_{670nm}}{R_{860nm} + 2.4R_{670nm} + 1}$	0 – 1	Landsat, MODIS
Photochemical reflectance index (PRI)	$\frac{R_{531nm} - R_{570nm}}{R_{531nm} + R_{570nm}}$	-1 – 1	Difficult due to narrow wavebands, but done from MODIS

Table 5.1 Traditional normalized reflectance indices used to characterize photosynthetic activity. These spectral indices are widely used to characterize photosynthetic activity of vegetation remotely from spectral reflectance measurements. The formation of normalized indices helps to account for variability in incoming radiation at different sites around the globe.

5.3.4 CO_2 flux measurements

All three study sites are active AmeriFlux and FLUXNET sites (Baldocchi et al. 2001) measuring fluxes of energy, water vapor, and carbon dioxide using standard eddy covariance methods and processing procedures described elsewhere in detail (Baldocchi et al. 2004, Ma et al. 2007, Sonnentag et al. 2011a, Hatala et al. 2012). Briefly, the eddy covariance technique was used to measure the fluxes of CO_2 at each site through simultaneous 10 Hz measurements of vertical turbulence (w, m/s), measured with a sonic anemometer (Gill WindMaster Pro; Gill Instruments Ltd, Lymington, Hampshire, England), and CO_2 density (c, μmol/m^3), measured with an infrared gas analyzer (LI-7500; Li-Cor Biosciences, Lincoln, NE). From these measurements I calculated a net flux of CO_2 (NEE, μmol m^{-2} s^{-1}) between the surface and atmosphere by averaging the covariance between w and c over a half-hourly time period after correcting for the effects of air density fluctuations (Webb et al. 1980, Detto et al. 2010). To partition NEE into gross ecosystem photosynthesis (GEP, μmol m^{-2} s^{-1}) and

ecosystem respiration (R_{eco}, μmol m^{-2} s^{-1}) I extrapolated nighttime NEE measurements throughout the entire day as R_{eco} modeled by a 2-week nonlinear temperature response (Reichstein et al. 2005). CO_2 flux data within this analysis are presented from the atmospheric convention, where a negative flux indicates ecosystem uptake, and a positive flux indicates release from the ecosystem to the atmosphere.

All three sites are also instrumented with sensors to measure incoming and reflected photosynthetically active radiation (PAR; μmol photons m^{-2} s^{-1}) mounted on a boom approximately 2 meters into the mean tower footprint at each site (PAR-LITE sensor, Kipp & Zonen, Delft, the Netherlands). From these data I calculated the absorbed PAR (APAR; μmol photons m^{-2} s^{-1}) as the difference between incoming and reflected PAR. I then integrated these measurements of APAR with GEP over each day of hyperspectral reflectance collection at each of the three sites to calculate daily light-use efficiency (LUE; mol CO_2 mol^{-1} PAR). Thus, while GEP is a measure of the gross CO_2 uptake of the plant canopy, LUE is a more ecophysiological measure that takes into account photosynthetic efficiency under different amounts of incoming PAR.

5.3.5 Leaf area index and foliar nitrogen measurements

Measurements of leaf area index (LAI; m^2/m^2) and foliar nitrogen content (N; percent dry mass) were collected throughout the study period to test the correlation between these ecosystem productivity measures and hyperspectral canopy reflectance. LAI was manually measured in situ at the pepperweed pasture and the rice paddy by the gap-fraction method with the LAI-2000 instrument (Li-Cor Biosciences, Lincoln, NE), after correcting for clumping effects (Ryu et al. 2010b). At the pepperweed pasture, LAI was measured at every 10m along a 500m transect into the mean wind direction of the flux footprint from 2008-2009, and every 10m along a 200m transect into the mean wind direction from 2010-2012. At the rice paddy, LAI was measured every 10m along a 200m transect into the mean wind direction in 2009, and every 10m along a 100m transect in 2010-2012.

LAI was measured from 2006-2012 at the annual grassland by destructive sampling. On each sampling date, three replicate samples were collected from the field by randomly placing a 20cm by 20cm PVC frame on the ground and harvesting all biomass within the frame. Back in the lab within 24 hours, the entire harvested green biomass was scanned to measure the surface area (LI-3100 Area Meter; Li-Cor Biosciences, Lincoln, NE) and LAI was calculated at the ratio of biomass area to harvested ground surface area. For this analysis, I calculated the LAI at each collection date at each site as the mean of all replicate measurements, for a total of 39 LAI sampling dates at the grassland, 49 LAI sampling dates at the pepperweed pasture, and 33 LAI sampling dates at the rice paddy.

Foliar nitrogen content was measured at the pepperweed pasture and the rice paddy from biomass harvests by the PVC square method described above except taking 5 random replicate samples per site, drying leaves to constant mass in the lab, and grinding and taking paired sub-samples of 6mg ± 2% for measurement of the percent carbon and percent nitrogen (Shimadzu Elemental Analyzer; Shimadzu Corporation, Kyoto, Japan). Replicate samples were rejected if the paired sub-samples from the same sample were more than 2% different in their N content. N was measured on 19 sampling dates at the pepperweed pasture and on 22 sampling dates at the rice paddy. Nitrogen content was also measured from 2006-2008 at the grassland with identical methods, and the correlation between percent nitrogen content and hyperspectral reflectance are previously published as Figure 10 in Ryu et al., [2010a].

5.4 Results and Discussion

5.4.1 Seasonal and spatial variability in reflectance within sites

For each sampling date at each site, I calculated the mean reflectance among all replicate samples (n=9 for the pasture, n=5 for the rice paddy, and n=2-3 for the annual grassland). The mean reflectance patterns reflect the seasonal drivers and phenology of each site (Figure 5.2). All three sites demonstrate the characteristic 'blue shift' as the red edge of reflectance from 700-720nm moves towards shorter wavelengths later in the growing season as the plants eventually senesce at each site (Rock et al. 1988). This pattern occurs as healthy leaves begin to show declining chlorophyll content and increasing tannin content as they proceed toward senescence. The highest region of light absorption at each of the three sites occurs at 460nm and 670nm, the wavelengths that correlate with chlorophyll a and b, during the peak growing season at each of the sites (springtime for the grassland and pasture, and late summer for the rice paddy).

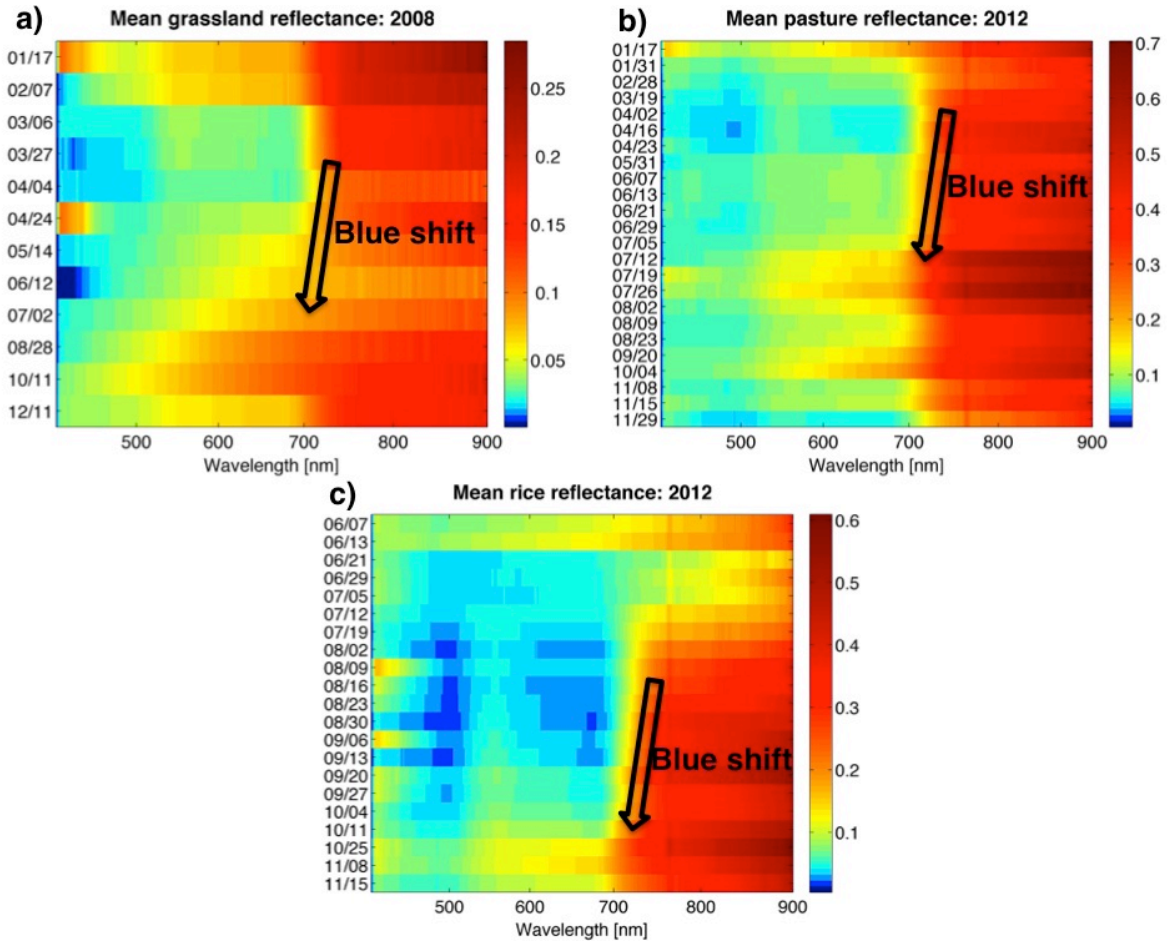

Figure 5.2 Seasonal patterns in mean hyperspectral reflectance. These plots highlight the seasonal pattern of spectral reflectance averaged across all replicates on each sampling date (y-axis) within one example year at each of the three sites. Each band along the y-axis represents the mean of replicate reflectance samples at the grassland (n=2-3), the pasture (n=9), and the rice paddy (n=5). At all three sites the plant canopy absorbs highly the visible wavelengths, and is more reflective in the infrared region. The regions of highest absorption correlate with the wavelengths of chlorophyll, at 460nm (blue) and 670nm (red). The 'blue shift' in the red edge (700-720nm) is especially clear as the plants senesce in mid to late summer at each of the sites.

For each sampling date, I calculated the traditional spectral reflectance indices outlined in Table 5.1 (Figure 5.3). In general, these traditional indices do a good job of capturing seasonal phenology at each of the three sites. At the grassland and rice paddy, NDVI captures the seasonal trends and peaks well. The response between NDVI and photosynthesis can saturate in some highly photosynthetic ecosystems, and there is some evidence for this saturation effect in 2011 at the rice paddy as NDVI plateaus near July. The seasonal pattern of EVI parallels that of NDVI although with a lower magnitude that tends to avoid saturation at high rates of photosynthesis.

At all sites the PRI seasonal time series is noisier than that of NDVI and EVI, although this metric also captures expected phonological patterns. At the grassland site and pasture site, PRI peaks in late spring and decreases during the hot and dry summer months. Surprisingly, the rice paddy PRI also shows a consistent seasonal decline. While a decline in PRI often indicates increasing canopy water or nitrogen stress, this is not the case for the flooded rice paddy, but instead could reflect the impacts of another increasing stressor, or the relationship could be demonstrating a covariation effect with foliar nitrogen, which is very high at the beginning of the season as seedlings emerge, but decreases as the plants mature (Figure 5.5e). Some of this variation in the PRI time series at all three sites might be attributed to the fact that PRI operates on a narrower window of spectral bands, and additional variation might be resolved by collecting a more finely grained time series of reflectance measurements, possibly through the use of continuous sensors, to investigate short-term variations in PRI with changes in LUE and canopy photosynthesis.

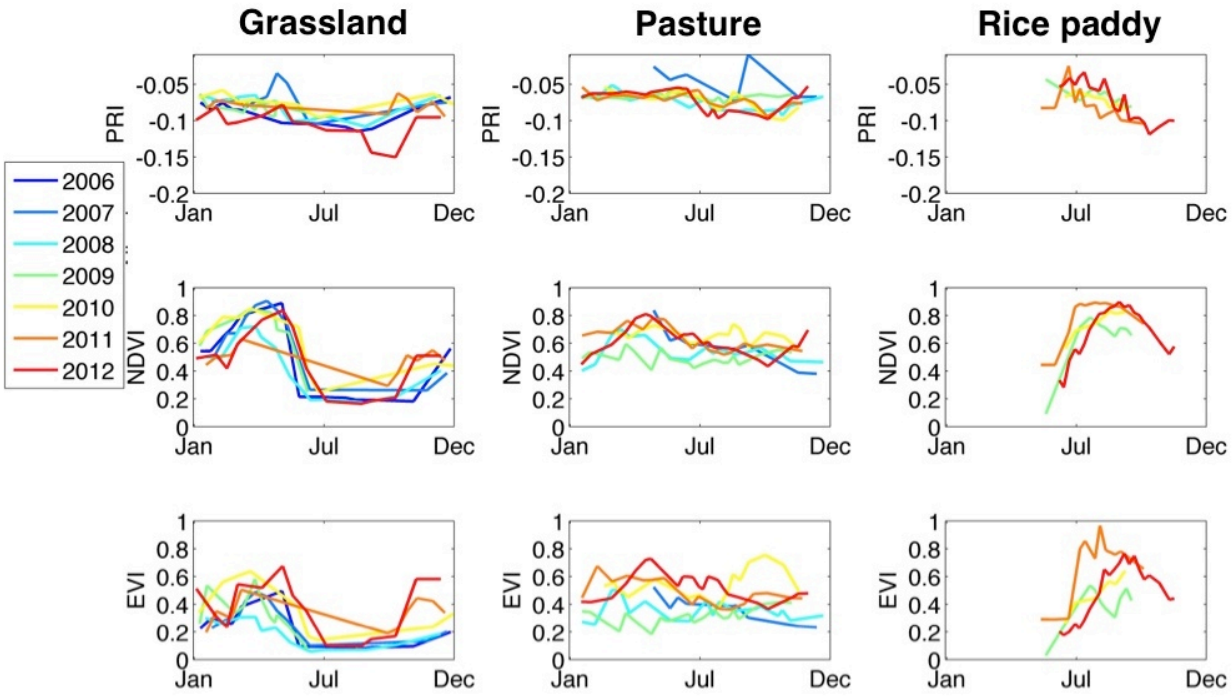

Figure 5.3 Seasonal patterns in traditional reflectance indices. In general, the traditional reflectance indices NDVI and EVI do a good job of tracking canopy phenology throughout the growing season across all sites, although these indices work less well at the degraded pasture site. In many ways the pasture is the most difficult site to characterize since the white canopy of pepperweed flowers may interfere with reflectance measurements during key points during the summer growing season. While PRI showed only slight seasonal variation at the grassland and degraded pasture, this index demonstrated a surprisingly strong seasonal decline at the rice paddy.

5.4.2 Time series of net and partitioned CO_2 fluxes, leaf area index, and foliar nitrogen

The time series of net and partitioned CO_2 fluxes varied dramatically by site during the study period, reflecting differences in ecophysiology among the three sites (Figure 5.4). The annual grassland has a very constrained growing season during the spring months, when both precipitation and sunlight are available. At this site R_{eco} parallels GEP during the spring growing season, and for the remainder of the year both the net and partitioned CO_2 fluxes are near zero as the grassland experiences the intense summer drought (Figure 5.4a-b). GEP at the annual grassland peaks at between 5-10 g-C $m^{-2}d^{-1}$ of CO_2 uptake during the springtime growing season, and R_{eco} peaks around 5 g-C $m^{-2}d^{-1}$.

At the pepperweed pasture, the NEE is more or less similar to that of the annual grassland, however the partitioned fluxes of GEP and R_{eco} are quite different (Figure 5.4c-d). At the pasture, the short springtime grass growing season parallels that of the annual grassland, but the pepperweed plant remains active throughout the summer, as their roots can tap the shallow water table. This increased activity from pepperweed creates higher GEP into the summer months. R_{eco} is also consistently much higher at the pasture than at the grassland, due to a relatively large contribution by heterotrophic microbes decomposing peat soil at the pasture throughout the year. As at the grassland, GEP at the pasture peaks also peaks between 5-10 g-C $m^{-2}d^{-1}$ of CO_2 uptake, but rates of R_{eco} routinely exceeds 5 g-C $m^{-2}d^{-1}$ for much of the year.

The rice paddy demonstrates a temporally constrained growing season, the length of which is similar to that of the annual grassland, but the growing season is offset to the late summer and early fall months (Figure 5.4e-f). GEP and R_{eco} at the rice paddy are temporally coupled, although the rates of heterotrophic soil respiration at the rice paddy are reduced during the growing season due to flooding, compared with the pasture, which is drained. Maximum GEP at the rice paddy is much higher than at the other two sites, between 10-15 g-C $m^{-2}d^{-1}$ of CO_2 uptake, and R_{eco} remains between 4-5 g-C $m^{-2}d^{-1}$ for the summer growing season.

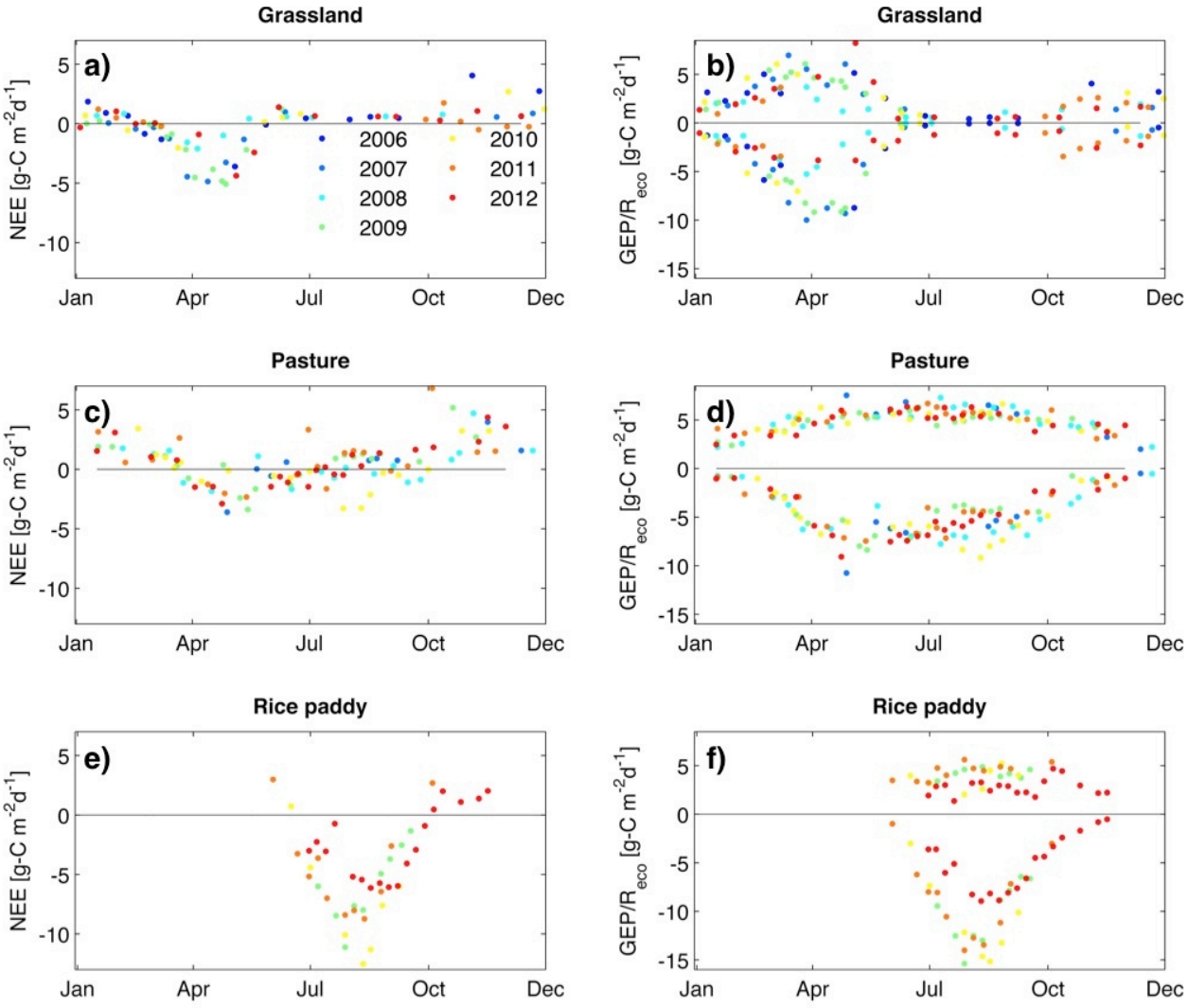

Figure 5.4 Flux time series used for correlation analysis. This figure outlines the net (a,c,e) and partitioned (b,d,f) CO_2 fluxes for dates where hyperspectral canopy reflectance was collected, where a negative value indicates CO_2 uptake. The CO_2 fluxes at the three sites follow a diverse set of ecophysiological adaptations. **a-b)** The grassland site has a very distinct and constrained growing season during the spring months, when both soil moisture and sunlight are available. **c-d)** The pasture site has consistent CO_2 uptake throughout most of the year, as the pepperweed plants at this site are able to tap the shallow water table during the dry summer months. The pasture also has a significant contribution from both autotrophic and heterotrophic respiration throughout the year, as peat soil decomposition is a significant source of CO_2 flux at this site. **e-f)** The rice paddy has a very constrained growing season controlled by the crop growing cycle, with very high rates of GEP during the summer growing season when the field is flooded and sunlight is abundant.

The time series of LAI at the three sites parallel patterns in GEP (Figure 5.5a-c). The LAI at both the grassland and the rice paddy show predictable patterns with moderate interannual variability in the magnitude and timing of the peak in LAI. The

pepperweed pasture site has much more interannual variability in the magnitude and timing of the peak in LAI. LAI at the grassland peaks between 3-4 m^2m^{-2}, LAI at the pasture peaks between 2-3 m^2m^{-2}, and LAI at the rice paddy peaks between 4-7 m^2m^{-2}. There is large interannual variability in LAI at the rice paddy due to differences in planting density between the four years in this analysis.

There are also large seasonal changes in the foliar nitrogen content (N) at the pasture and rice paddy (Figure 5.5d-e). N is high at the beginning of the growing season at both sites during the period of new vegetation growth, and then decreases during the season as the plants mature. At the pasture, N is near 5% at the start of the spring, and decreases to about 2.5% during mid-summer. At the rice paddy, N begins near 4.5% at the start of the growing season, and decreases to about 2% at the end of the growing season.

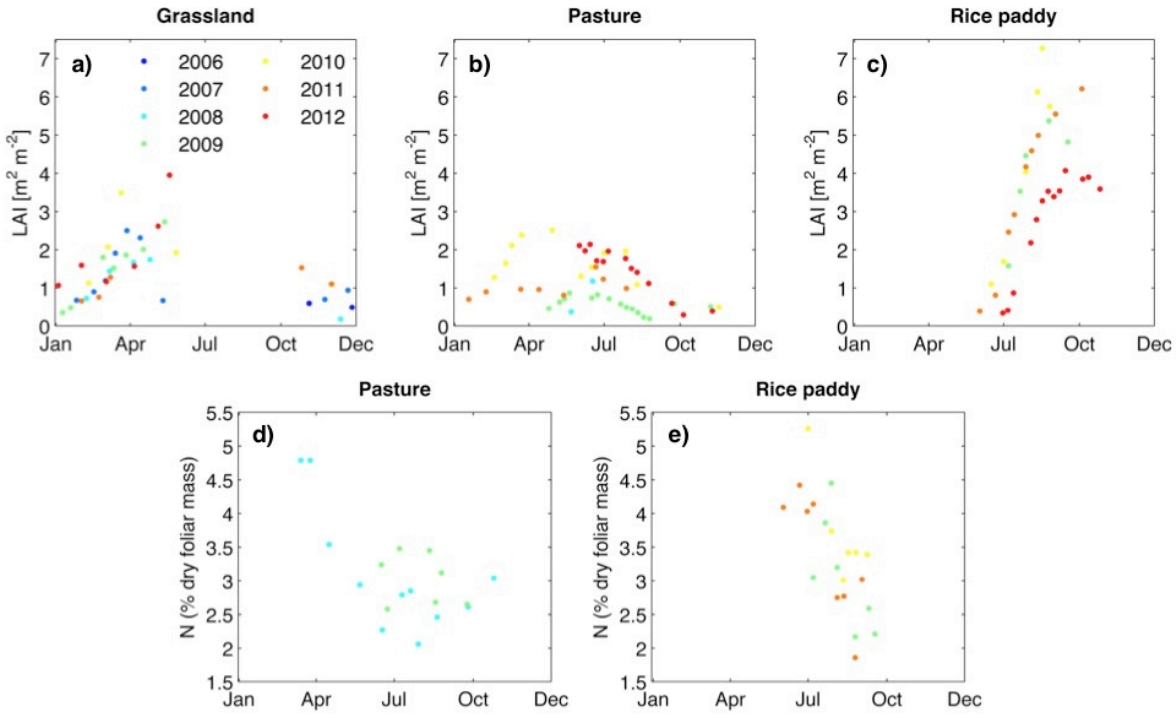

Figure 5.5 Leaf area index and foliar nitrogen time series used for correlation analysis. a-c) The patterns in leaf area index at the three sites paralleled patterns in GEP (Figure 5.4). The grassland and rice paddy both have very predictable growing seasons with moderate interannual variability in the leaf area index. The pasture site has more interannual variability in the peak of LAI during each year. **d-e)** Trends in foliar nitrogen at both the pasture and the rice paddy tend to be large upon plant emergence, and decrease throughout the growing season as plants mature.

5.4.3 Correlations between traditional spectral indices and GEP, LUE, and LAI

In order to determine whether the traditional reflectance indices NDVI, EVI, and PRI captured variations in ecosystem productivity across all three sites, I tested the correlations between these indices and GEP, LUE, and LAI (Figure 5.6). Across all three sites, NDVI has clear, consistent, and statistically significant relationships with GEP, LUE, and LAI (Figure 5.6a-c). Reflectance measurements of NDVI tend to saturate in structurally complex and highly photosynthetic ecosystems (Baret and Guyot 1991) and for the three ecosystems in this analysis there is a mild saturation effect as NDVI is best correlated with GEP and LAI through an exponential relationship that increases rapidly at high NDVI. The correlations between NDVI and GEP, LUE, and LAI are strongest for the grassland and rice paddy (Figure 5.6a,c), but are lower for the pepperweed pasture (Figure 5.6b). There is considerably more variability in the relationships between reflectance and ecosystem characteristics at the pasture site, likely due to both the higher spatial heterogeneity at the site, as the land surface at the pasture has patches of pepperweed, grass, and bare ground, as well as the complex phenology of the pepperweed plants. Because pepperweed makes a dense canopy of white flowers near June that can persist into September, this dampens the ability of a downward-looking reflectance sensor to measure changes in leaf physiology, which are mostly located below the white flower canopy (Sonnentag et al. 2011b). Thus, the response for the pasture site is generally noisier than the annual grassland and rice paddy, which are more spatially homogeneous with less complex phenologies.

EVI captures statistically significant trends in GEP, LUE, and LAI at the grassland site, in LUE and LAI at the rice paddy, and in only LAI at the pasture (Figure 5.6d-f). While the correlation between LAI and EVI is near that of the LAI-NDVI relationship, the statistical power of the relationship is lower across all three sites. Although EVI has outperformed NDVI in the prediction of GEP in needleleaf forests (Xiao et al. 2005) and in predicting leaf area index in recovering burnt tundra with background soil contamination (Rocha and Shaver 2009), in these simpler plant canopies the added complexity of EVI might introduce noise into the response signal. While previous work shows that although EVI has great utility for use in forests where NDVI saturates and in arid and semiarid ecosystems with high contamination from background reflectance, NDVI can capture variation at short-statured grassland sites with relatively simple plant canopies (Huete et al. 1997). However, the relationship between EVI and LAI does not demonstrate a saturation effect as NDVI does, since the slopes of the fits are linear rather than exponential (Figure 5.6f). This highlights the fact that although the fit between EVI and LAI has a slightly lower R^2 than that for NDVI, the performance might be more ideal for similar ecosystems with higher LAI.

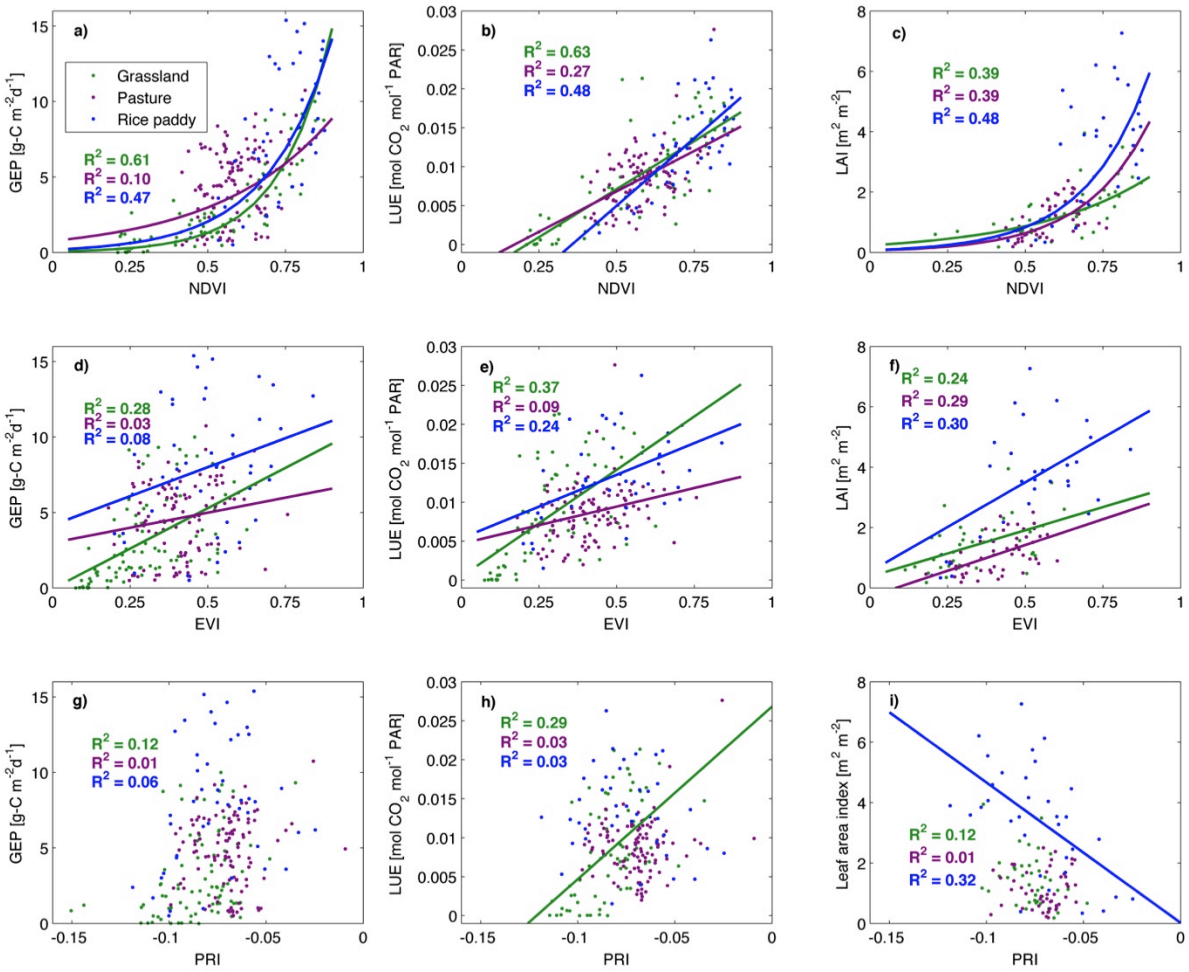

Figure 5.6 Ability of traditional reflectance indices to capture GEP, LUE, and LAI across the three sites. a-c) Across all three sites, the Normalized Difference Vegetation Index (NDVI) best captured the variation in all three variables connected with vegetation carbon fluxes, GEP, LUE, and LAI. NDVI shows only a small saturation effect at high rates of productivity, but this saturation is not limiting for the correlation fit likely due to the short-statured vegetation at all three sites that have very distinct growing seasons. **d-f)** The enhanced vegetation index (EVI) was consistently correlated with GEP, LUE, and LAI at the grassland site, but had no correlation with GEP at the pasture or rice paddy. EVI was able to capture some variability in LUE at the rice paddy site, and was a good predictor of LAI across all three sites. **g-i)** The photochemical reflectance index (PRI) was a relatively poor predictor of GEP across all three sites, but captured significant variability in LUE at the grassland. PRI is likely uncorrelated with LUE at the pasture and rice paddy since these sites are well watered and experience little canopy stress. PRI has a significant negative correlation with LAI at the rice paddy, but I suspect that this might be an artifact of the trend in foliar nitrogen content, which decreases from the seedling to mature plant stage.

PRI is uncorrelated with GEP across the three sites, but at the annual grassland PRI captures statistically significant variation in LUE, although there is no strong relationship between PRI and LUE at the pepperweed pasture or rice paddy (Figure

5.6g-h). PRI was developed as an index to capture variations in the xanthophyll cycle indicative of foliar nitrogen stress (Gamon et al. 1992) and both the rice paddy and pasture experience very little nitrogen limitation, as the rice paddy is fertilized and pepperweed plants accumulate high levels of nitrogen in their tissue (Runkle 2009). There is also a lack of drought stress at both the rice paddy and the pasture, where the pepperweed plants can tap the shallow water table, also possibly dampening the signal between PRI and LUE. Thus, PRI has utility in capturing LUE trends at the semi-arid grassland, but not at the pepperweed pasture and rice paddy. PRI has a significant negative correlation with LAI at the rice paddy (Figure 5.6i), however I suspect that this relationship might be an artifact of the relationship with rice N content, which is very high at the beginning of the growing season when the plants are seedlings, but decreases significantly throughout the season as the plants mature. PRI and LAI were uncorrelated at both the grassland and the pepperweed pasture.

5.4.4 Using the entire hyper-spectrum to search for new reflectance proxies for CO_2 fluxes

While some traditional reflectance indices well captured seasonal variability at some of the sites within years, I also used the full information content of the hyperspectral ground reflectance data to search for new indices that might be well-correlated with ecosystem productivity. To do this, I investigated the correlation between normalized difference reflectance indices constructed from pairs of wavelengths across the whole 400-900nm spectrum (Eqn. 5.1) and the gross and partitioned CO_2 fluxes, LAI, and N. Using a normalized index helps to account for illumination changes due to the change in the solar azimuth angle throughout the year.

$$\text{Normalized Index} = \frac{\text{Refl}_{\lambda 1} - \text{Refl}_{\lambda 2}}{\text{Refl}_{\lambda 1} + \text{Refl}_{\lambda 2}} \qquad \text{Equation 5.1}$$

I first tested the ability of spectral indices across the whole 400-900nm spectrum to capture variation in NEE at each of the sites (Figure 5.7). The correlation between surface reflectance indices and NEE depends on the ability of the reflectance properties at the surface to change in step with the net carbon fluxes of both GEP and R_{eco} at the sites, assuming a coupling between GEP and R_{eco}. Although this coupling is present to some extent at all sites, the pasture site shows particularly weaker correlation between reflectance indices and NEE due to the fact that a significant portion of R_{eco} at this site originates from soil organic matter decomposition (Hatala et al. 2012).

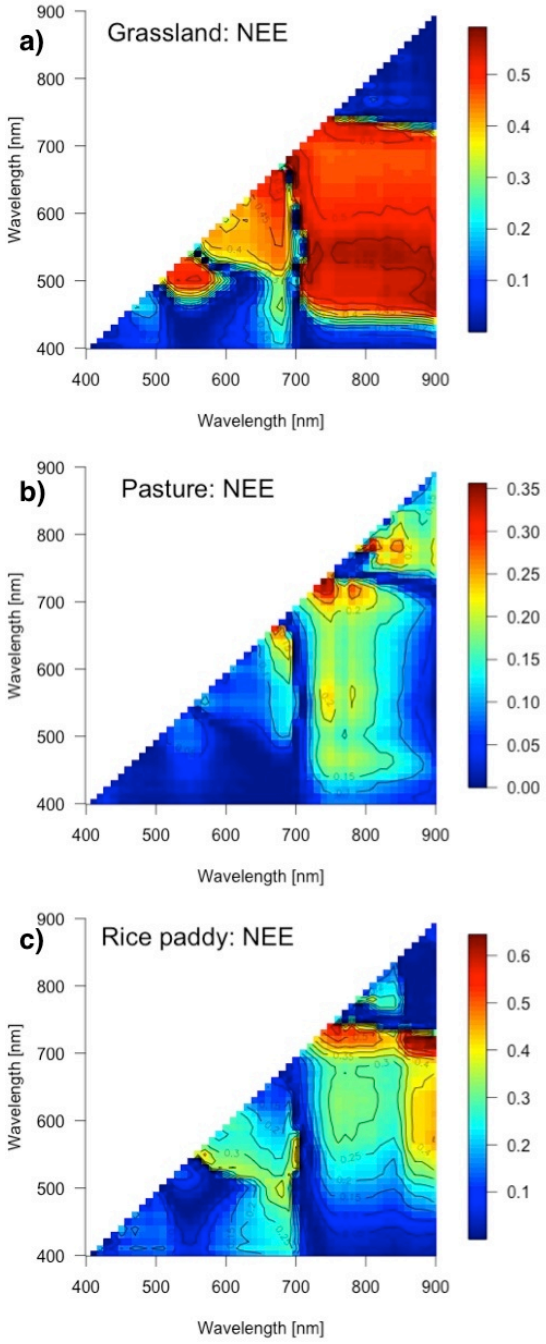

Figure 5.7 Contour plots for the correlation between reflectance indices from 400-900nm and net ecosystem exchange. These contour maps highlight correlation coefficients (r) between portions of the spectrum from 400-900nm for which normalized indices using two wavelengths (x and y axes) are correlated with the net CO_2 fluxes for that day measured at the grassland (n=81), the pasture (n=110), and the rice paddy (n=45). The pasture and rice paddy demonstrate clear regions of the spectral indices that are highly correlated with the net CO_2 fluxes. The correlation between reflectance metrics at the net CO_2 flux at the pasture is a bit lower, likely due to the white flowers of the pepperweed plant interfering with reflectance measurements and the decoupling between GEP and R_{eco} at the site, as decomposing soil carbon is a significant portion of R_{eco}.

The grassland site shows high correlation (r^2>0.55) with reflectance indices constructed between the green region (530nm) and the entire infrared region (700-900nm), indicating that patterns in NEE are strongly driven by the phenology of the grass during the growing season (Figure 5.7a). Across all three sites NEE was highly correlated (r^2>0.55 at the grassland and rice paddy, r^2>0.3 at the pasture) with indices between the near infrared (720nm) and the farther near infrared (780-850nm) regions. This pattern is likely driven by the 'blue shift' demonstrated in Figure 5.2, of the movement of the red edge of reflectance from 720nm to 700nm toward shorter wavelengths with plant senescence at the end of the growing seasons. For all three sites, NEE tended to demonstrate higher correlation with indices that utilized portions of the near infrared spectrum, indicating that both pigmentation of plant biochemical compounds in the visible region as well as canopy structure, which controls the dissipation of energy in the near-infrared region, are important variables for characterizing NEE.

I also tested the correlation between normalized difference reflectance indices across the 400-900nm range and the partitioned CO_2 fluxes, GEP and R_{eco} (Figure 5.8). Across all three sites, the highest correlation between a reflectance index and GEP occurred near the same wavelengths as NDVI, the red absorption (680-700nm) and near infrared reflectance (720-880nm) (Figure 5.8a,c,e). This corroborates the early evidence from Figure 5.5 that NDVI is well suited to capture photosynthetic patterns across the three field sites, to the extent that a better index does not exist across the 400-900nm range. However, again the correlation between NDVI and GEP was lower at the degraded pasture, likely due to the issues discussed in section 5.4.3, where spatial heterogeneity and pepperweed flowering phenology likely contribute noise to the reflectance signal.

Although the correlations between R_{eco} and the reflectance indices were weaker at all of the three sites compared with the correlations with GEP, there were still some significant correlations with R_{eco} at the three sites. R_{eco} at the grassland was highly correlated with a reflectance index constructed between the green (520nm) and red (600-700nm) reflectance, indicating high connectivity between the green grass canopy and R_{eco}. This highlights the fact that the phenology of the microbial and plant communities are totally synchronized at the grassland, where they are both active when soil moisture is abundant from the springtime rain (Figure 5.8b).

At the rice paddy, there was a moderate statistically significant correlation (r^2>0.3) for an index between the blue wavelength active for chlorophyll a (480nm) and green reflectance (550nm), indicating that R_{eco} at the rice paddy is also coupled with the rice growing season (Figure 5.8f). There is also a narrow-band index between the red

chlorophyll absorption range (650-680nm) and the very near infrared (700nm) at both the pasture (r^2>0.2) and the rice paddy (r^2>0.3) that is correlated with R_{eco}, again indicating a correspondence between plant productivity and R_{eco} linked through spectral reflectance (Figure 5.8d,f). While R_{eco} at the grassland demonstrates a high correlation with reflectance indices, the much lower correlation at the rice paddy and pasture is likely due to a larger contribution from heterotrophic respiration at these sites, which are located on peat soils that experience much higher rates of microbial decomposition.

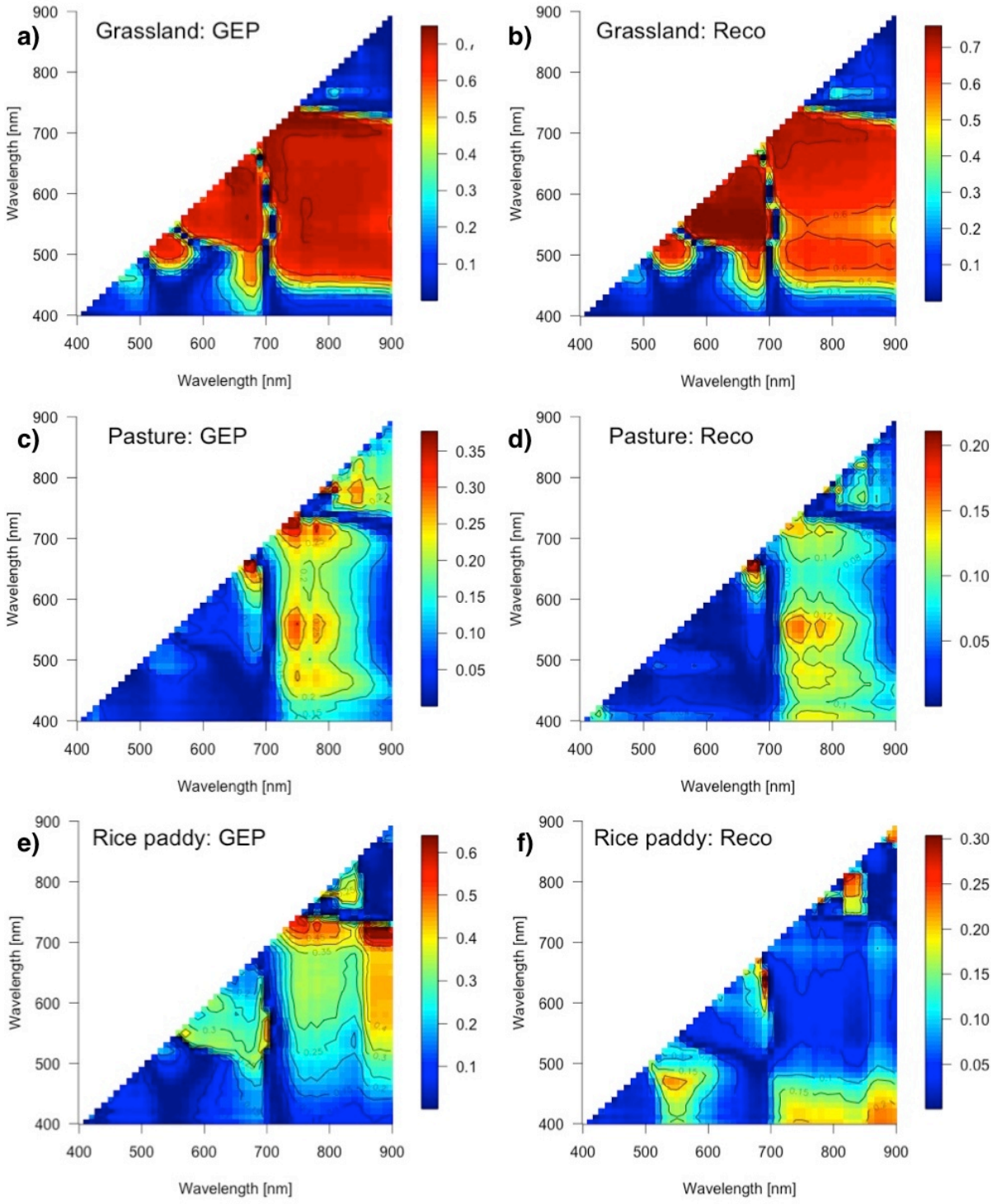

Figure 5.8 Contour plots for the correlation between reflectance indices from 400-900nm and partitioned CO_2 fluxes. These contour maps highlight correlation coefficients (r^2) between portions of the spectrum from 400-900nm for which normalized indices using two wavelengths (x and y axes) are correlated with the partitioned CO_2 fluxes, gross ecosystem productivity (GEP) and ecosystem respiration (R_{eco}) for that day measured at the grassland (n=81), the pasture (n=110), and the rice paddy (n=45). All three sites show a strong correlation between GEP and reflectance in the near infrared (720nm) and the

farther infrared (780-860nm), correlated with the 'blue shift' highlighted in Figure 5.2, which tracks the phenology of senescence at each site. The R_{eco} at both the grassland and rice paddy is very highly correlated with indices between the visible portions of the spectra driven by plant biochemistry and the infrared portion of the spectrum, indicating that plant biochemistry is strongly driving R_{eco}. There is only a very weak correlation between R_{eco} and spectral indices at the pasture, likely due to the large contribution of soil decomposition to the value of R_{eco} at this site.

5.4.5 Using the entire hyper-spectrum to search for new reflectance proxies for LAI and foliar nitrogen

I also investigated the correlation between paired normalized spectral indices across the entire 400-900nm and range and LAI and N, which are important driving variables for ecosystem productivity in many earth systems models (Bonan 1995). LAI estimates are currently generated from MODIS satellite spectral reflectance data by inverting a radiative transfer model with additional constraints by biome type, and LAI shows a strong and consistent relationship with MODIS NDVI (Knyazikhin et al. 1998, Myneni et al. 2002). In this analysis, LAI was significantly correlated with indices in the same range as NDVI and EVI at the pepperweed pasture (r^2>0.4) and rice paddy (r^2>0.65) sites (Figure 5.9b-c). At the pepperweed pasture there was also a high correlation between LAI and a normalized index between the green region at 550nm and the near infrared region (r^2>0.45).

Interestingly, LAI at the grassland site with not correlated with indices near the NDVI region, but instead with indices that paralleled those with high correlation to N (r^2>0.25), between the green and red portions of the spectrum (Figure 5.10 this paper, and Figure 10 Ryu et al. [2010]). One possible reason for the low correlation between LAI and NDVI at the grassland is that LAI is a long-term integrator of ecosystem productivity, so the hyperspectral reflectance captured at one timepoint and long-term LAI might be asynchronous, depending on sampling strategy. This result could also demonstrate bias in the LAI sampling methodology, since relatively few replicate destructive samples were collected the grassland relative to the other two sites, and wilting could have occurred between the time of clipping and the time of areal scanning in the lab.

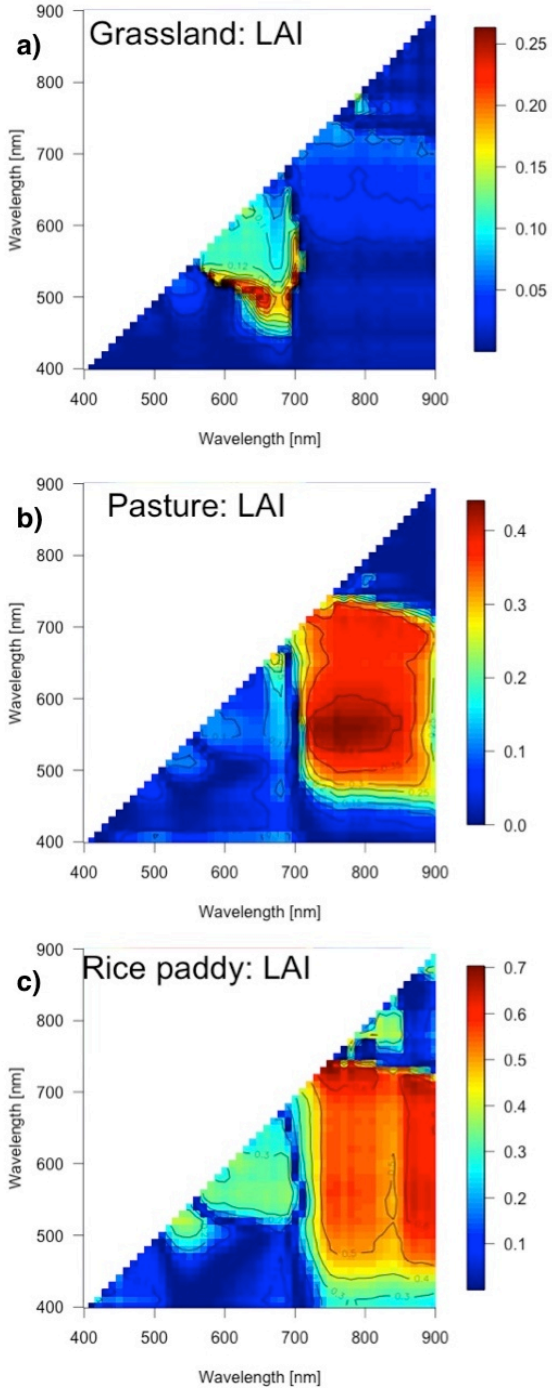

Figure 5.9 Contour plots for the correlation between reflectance indices from 400-900nm and leaf area index. All three sites showed relatively good agreement between normalized spectral reflection indices and leaf area index. **a)** Interestingly, the spectral reflectance indices that corresponded best with nitrogen for the pasture and rice paddy (Figure 5.10) matched leaf area index at the grassland site (n=39, r^2>0.3). This likely indicates a covariation between leaf nitrogen content and leaf area. **b)** At the pasture site, leaf area index was high correlated (n=49, r^2>0.5) was spectral indices between the red and near infrared regions, although slightly outside the range for NDVI and EVI calculations. **c)** The leaf area index at the rice paddy was very highly correlated with the same index used to calculate NDVI (n=33, r^2>0.65).

Canopy reflectance measurements have also been identified as a promising method for deriving canopy foliar nitrogen content (N). Reflectance from broad-band satellite platforms have demonstrated strong correlation between N and short-wave albedo (Ollinger et al. 2008), although recent work shows that additional considerations of canopy structure and light transmission are required when interpreting the relationship between albedo and N (Knyazikhin et al. 2013). Other hyperspectral indices with high correlation to N utilize reflectance in the farther infrared range between 900-2900nm (Kokaly 2001, Smith et al. 2002, Martin et al. 2008), which is beyond the range of the reflectance spectrometer used in this analysis. Although the data presented here are limited to the 400-900nm hyperspectral reflectance range, I nonetheless searched for normalized difference correlation indices for the study period that captured variation in N.

There was high and consistent correlation between N and a reflectance index between 500nm and 630nm at both the pasture ($r^2>0.6$) and the rice paddy ($r^2>0.45$) (Figure 5.10). The 500nm wavelength corresponds with green reflectance, and the 630nm wavelength is very near the red chlorophyll absorption wavelength. This index is likely correlated with N since these wavelengths are indicating a period when the canopy is very green due to high chlorophyll contents to support high rates of photosynthesis, so N is correspondingly high. The high correlation between N and a normalized index between 500nm and 620nm was also present and statistically significant in previously published work from the grassland site (Figure 10 in Ryu et al. [2010a], $r^2>0.7$, n=10). Although this is an empirical index that has yet to be tested in other environments, this high correlation indicates a promising avenue for future monitoring of general trends N at these three sites and similarly structured sites in the future.

Much previous work has been focused on locating reflectance bands correlated with N in crops to detect nitrogen stress and to accurately time fertilizer treatment. Previous work conducted identified a strong correlation between N content and a normalized index constructed from blue reflectance (440nm) and green reflectance (573nm) in winter wheat (Hansen and Schjoerring 2003), between blue reflectance (410nm) and red reflectance (710nm) in sorghum (Zhao et al. 2005), and between green reflectance (550nm) and red reflectance (710nm) in corn (Zhao et al. 2003). Although these bands are different from the most significant index between reflectance and N from this analysis, they follow the same biochemical principle of constructing an index between a chlorophyll absorption band and a green reflectance band. Results from a rice meta-analysis of hyperspectral reflectance and N content across many sites yielded

the conclusion that a normalized index between green reflectance (500-550nm) and yellow-orange reflectance (550-600nm) was the best fit index, similar to the conclusions of this work (Tian et al. 2011).

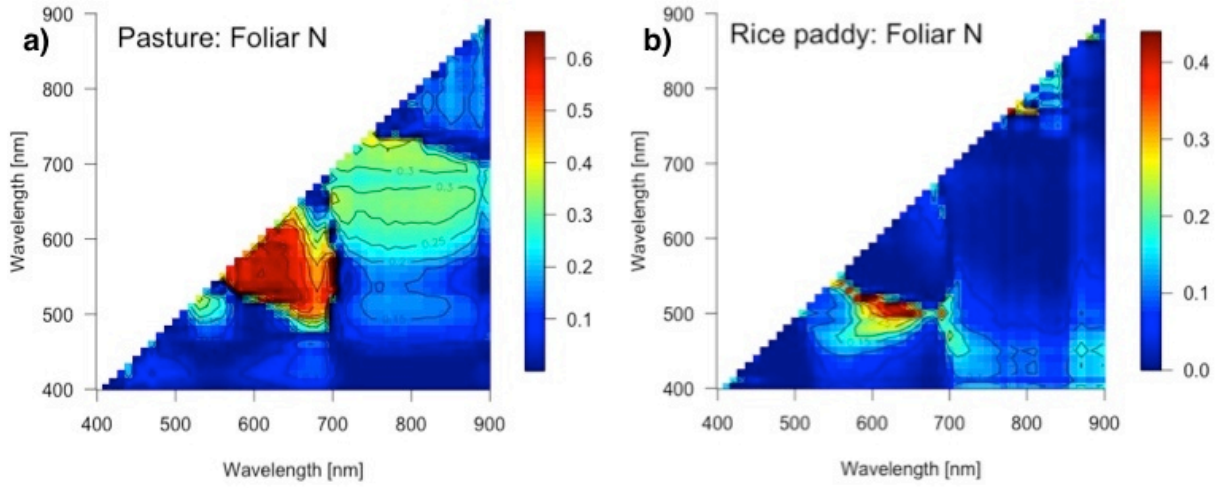

Figure 5.10 Contour plots for the correlation between reflectance indices from 400-900nm and foliar nitrogen content. These plots highlight a spectral reflectance region between 510nm (green) and 630nm (red) with high correlation (R^2>0.5) to percent nitrogen content of dry foliar biomass samples from the pasture site (n=19) and rice site (n=22). The percent nitrogen content is highly correlated with this portion of the spectrum likely due to the high peak in green reflectance and high absorption in the red chlorophyll region when nitrogen content is high and stimulating photosynthesis. A similar previously published figure that examined correlation between foliar N and reflectance indices at the pasture site revealed a high correlation in the same region (Figure 10 in Ryu et al., [2010a]).

5.5 Conclusions

At all three sites, aspects of the surface reflectance were correlated with both the net and partitioned ecosystem CO_2 fluxes, as well as LAI and N. The traditional remote sensing index NDVI was particularly skilled at capturing variation in canopy-scale ecosystem productivity, measured through GEP, LUE, and LAI across all sites. Although there were some reflectance indices that also showed some degree of correlation with GEP at the three sites, there was no reflectance metric that outperformed NDVI. This is likely due to the short stature and simplicity of the plant canopies at each of the three sites, although the more complex flowering phenology of the pepperweed at the pasture site likely contributed additional noise to the GEP and NDVI relationship.

One caveat to this analysis is that using reflectance measurements to measure net CO_2 fluxes or R_{eco} is necessarily indirect, since changes in leaf properties can directly correlate with changes in GEP, but only indirectly with root or microbial respiration. However, analyzing the correlations between reflectance indices and net carbon dioxide fluxes does yield insights into the coupling between plant and microbial productivity. Both net CO_2 fluxes and R_{eco} at the grassland site were highly correlated with surface reflectance, indicating a high degree of synchronization between microbial and plant communities during the short annual grassland growing season. At both the rice paddy and the degraded pasture sites the surface reflectance was less coupled with R_{eco} since there is significant soil organic matter decomposition year-round at this site.

Correlations between hyperspectral reflectance and foliar nitrogen content revealed a consistent pattern across all three sites, where N was highly correlated with a normalized reflectance index between 510nm and 620nm. The consistency of this relationship and corroborating with other results from rice paddies (Tian et al. 2011) yields promise for developing an N index that can be monitored in the field with inexpensive LED sensors (Ryu et al. 2010a). Further measurements of hyperspectral reflectance in ecosystems with a wider seasonal range of N content would yield valuable insight for the potential of this index to act as a rigorous proxy for foliar N. The collection of long-term near-surface reflectance datasets such as the one presented in this analysis are invaluable for developing a rigorous understanding of the seasonal and interannual changes in canopy reflectance and tracking how ecosystem productivity is translated into canopy reflectance.

References

Alewell, C., M. Schaub, and F. Conen. 2009. A method to detect soil carbon degradation during soil erosion. Biogeosciences **6**:2541-2547.

Allard, V., J. F. Soussana, R. Falcimagne, P. Berbigier, J. M. Bonnefond, E. Ceschia, P. D'Hour, C. Henault, P. Laville, C. Martin, and C. Pinares-Patino. 2007. The role of grazing management for the net biome productivity and greenhouse gas budget (CO2, N2O and CH4) of semi-natural grassland. Agriculture Ecosystems & Environment **121**:47-58.

Armentano, T. V. 1980. Drainage of organic soils as a factor in the world cabon-cycle. Bioscience **30**:825-830.

Baldocchi, D., M. Detto, O. Sonnentag, J. Verfaillie, Y. A. Teh, W. Silver, and N. M. Kelly. 2012. The challenges of measuring methane fluxes and concentrations over a peatland pasture. Agricultural and Forest Meteorology **153**:177-187.

Baldocchi, D. D., E. Falge, L. H. Gu, R. Olson, D. Hollinger, S. Running, P. Anthoni, C. Bernhofer, K. Davis, R. Evans, J. Fuentes, A. Goldstein, G. Katul, B. Law, X. H. Lee, Y. Malhi, T. Meyers, W. Munger, W. Oechel, K. T. P. U, K. Pilegaard, H. P. Schmid, R. Valentini, S. Verma, T. Vesala, K. Wilson, and S. Wofsy. 2001. FLUXNET: A new tool to study the temporal and spatial variability of ecosystem-scale carbon dioxide, water vapor, and energy flux densities. Bulletin of the American Meteorological Society **82**:2415-2434.

Baldocchi, D. D., B. B. Hicks, and T. P. Meyers. 1988. Measuring biosphere-atmosphere exchanges of biologically related gases with micrometeorological methods. Ecology **69**:1331-1340.

Baldocchi, D. D. and K. S. Rao. 1995. Intra-field variability of scalar flux densities across a transition between a desert and an irrigated potato field. Boundary-Layer Meteorology **76**:109-136.

Baldocchi, D. D., L. K. Xu, and N. Kiang. 2004. How plant functional-type, weather, seasonal drought, and soil physical properties alter water and energy fluxes of an oak-grass savanna and an annual grassland. Agricultural and Forest Meteorology **123**:13-39.

Baret, F. and G. Guyot. 1991. Potentials and limits of vegetation indexes for LAI and APAR assessment. Remote Sensing of Environment **35**:161-173.

Bauer, M. E. 1975. The role of remote sensing in determining the distribution and yield of crops. Advances in Agronomy **27**:271-304.

Bianchi, T. S. and M. A. Allison. 2009. Large-river delta-front estuaries as natural "recorders" of global environmental change. Proceedings of the National Academy of Sciences of the United States of America **106**:8085-8092.

Bohn, T. J. and D. P. Lettenmaier. 2010. Systematic biases in large-scale estimates of wetland methane emissions arising from water table formulations. Geophysical Research Letters **37**.

Bonan, G. B. 1995. Land atmosphere interactions for climate system models - Coupling biophysical, biogeochemical, and ecosystem dynamical processes Remote Sensing of Environment **51**:57-73.

Brinson, M. M., A. E. Lugo, and S. Brown. 1981. Primary productivity, decomposition and consumer activity in fresh water wetlands. Annual Review of Ecology and Systematics **12**:123-161.

Cai, Z. C., G. X. Xing, X. Y. Yan, H. Xu, H. Tsuruta, K. Yagi, and K. Minami. 1997. Methane and nitrous oxide emissions from rice paddy fields as affected by nitrogen fertilisers and water management. Plant and Soil **196**:7-14.

Campbell, C. S., J. L. Heilman, K. J. McInnes, L. T. Wilson, J. C. Medley, C. W. Wu, and D. R. Cobos. 2001. Diel and seasonal variation in CO2 flux of irrigated rice. Agricultural and Forest Meteorology **108**:15-27.

Canuel, E. A., E. J. Lerberg, R. M. Dickhut, S. A. Kuehl, T. S. Bianchi, and S. G. Wakeham. 2009. Changes in sediment and organic carbon accumulation in a highly-disturbed ecosystem: The Sacramento-San Joaquin River Delta (California, USA). Marine Pollution Bulletin **59**:154-163.

Chanton, J. P., C. S. Martens, C. A. Kelley, P. M. Crill, and W. J. Showers. 1992. Methane transport mechanisms and isotopic fractionation in emergent macrophytes of an Alaskan tundra lake. Journal of Geophysical Research-Atmospheres **97**:16681-16688.

Chanton, J. P., G. J. Whiting, N. E. Blair, C. W. Lindau, and P. K. Bollich. 1997. Methane emission from rice: Stable isotopes, diurnal variations, and CO2 exchange. Global Biogeochemical Cycles **11**:15-27.

Chapin, F. S., III, G. M. Woodwell, J. T. Randerson, E. B. Rastetter, G. M. Lovett, D. D. Baldocchi, D. A. Clark, M. E. Harmon, D. S. Schimel, R. Valentini, C. Wirth, J. D. Aber, J. J. Cole, M. L. Goulden, J. W. Harden, M. Heimann, R. W. Howarth, P. A. Matson, A. D. McGuire, J. M. Melillo, H. A. Mooney, J. C. Neff, R. A. Houghton, M. L. Pace, M. G. Ryan, S. W. Running, O. E. Sala, W. H. Schlesinger, and E. D. Schulze. 2006. Reconciling Carbon-Cycle Concepts, Terminology, and Methods. Ecosystems **9**:1041-1050.

Chasmer, L., N. Kljun, C. Hopkinson, S. Brown, T. Milne, K. Giroux, A. Barr, K. Devito, I. Creed, and R. Petrone. 2011. Characterizing vegetation structural and topographic characteristics sampled by eddy covariance within two mature aspen stands using lidar and a flux footprint model: Scaling to MODIS. Journal of Geophysical Research-Biogeosciences **116**.

Chen, Y. H., S. L. Bressler, and M. Z. Ding. 2006. Frequency decomposition of conditional Granger causality and application to multivariate neural field potential data. Journal of Neuroscience Methods **150**:228-237.

Cicerone, R. J., C. C. Delwiche, S. C. Tyler, and P. R. Zimmerman. 1992. Methane emissions from California rice paddies with varied treatments. Global Biogeochemical Cycles **6**:233-248.

Cicerone, R. J. and J. D. Shetter. 1981. Sources of atmospheric methane - measurements in rice paddies and a discussion. Journal of Geophysical Research-Oceans and Atmospheres **86**:7203-7209.

Cicerone, R. J., J. D. Shetter, and C. C. Delwiche. 1983. Seasonal-variation of methane flux from a California rice paddy. Journal of Geophysical Research-Oceans and Atmospheres **88**:1022-1024.

Colwell, J. E. 1974. Vegetation canopy reflectance. Remote Sensing of Environment **3**:175-183.

Conrad, R. 2007. Microbial ecology of methanogens and methanotrophs. Pages 1-63 *in* D. L. Sparks, editor. Advances in Agronomy.

Crooks, S. 2009. The impacts of sea level rise on tidal wetlands: Implications for carbon sequestration and estuarine management. Philip Williams & Associates for the Resources Legacy Fund, San Francisco, CA.

Dannenberg, S. and R. Conrad. 1999. Effect of rice plants on methane production and rhizospheric metabolism in paddy soil. Biogeochemistry **45**:53-71.

Daubechies, I. 1990. The wavelet transform, time-frequency localization and signal analysis. IEEE Transactions on Information Theory **36**:961-1005.

Denier van der Gon, H. A. C. and N. van Breemen. 1993. Diffusion-controlled transport of methane from soil to atmosphere as mediated by rice plants. Biogeochemistry **21**:177-190.

Detto, M., D. Baldocchi, and G. G. Katul. 2010. Scaling Properties of Biologically Active Scalar Concentration Fluctuations in the Atmospheric Surface Layer over a Managed Peatland. Boundary-Layer Meteorology **136**:407-430.

Detto, M. and G. G. Katul. 2007. Simplified expressions for adjusting higher-order turbulent statistics obtained from open path gas analyzers. Boundary-Layer Meteorology **122**:205-216.

Detto, M., N. Montaldo, J. D. Albertson, M. Mancini, and G. Katul. 2006. Soil moisture and vegetation controls on evapotranspiration in a heterogeneous Mediterranean ecosystem on Sardinia, Italy. Water Resources Research **42**:W08419.

Detto, M., J. Verfaillie, F. Anderson, L. Xu, and D. Baldocchi. 2011. Comparing laser-based open- and closed-path gas analyzers to measure methane fluxes using the eddy covariance method. Agricultural and Forest Meteorology **151**:1312-1324.

Deverel, S. J. and D. A. Leighton. 2010. Historic, Recent, and Future Subsidence, Sacramento-San Joaquin Delta, California, USA. San Francisco Estuary and Watershed Science **8**.

Dhamala, M., G. Rangarajan, and M. Ding. 2008. Estimating granger causality from fourier and wavelet transforms of time series data. Physical Review Letters **100**.

Dickerman, J. A. and R. G. Wetzel. 1985. Clonal Growth in Typha Latifolia: Population Dynamics and Demography of the Ramets. Journal of Ecology **73**:535-552.

Drexler, J. Z., F. E. Anderson, and R. L. Snyder. 2008. Evapotranspiration rates and crop coefficients for a restored marsh in the Sacramento-San Joaquin Delta, California, USA. Hydrological Processes **22**:725-735.

Drexler, J. Z., C. S. de Fontaine, and T. A. Brown. 2009a. Peat accretion histories during the past 6,000 years in the marshes of the Sacramento-San Joaquin Delta, CA, USA Estuaries and Coasts **32**:871-892.

Drexler, J. Z., C. S. de Fontaine, and S. J. Deverel. 2009b. The legacy of wetland drainage on the remaining peat in the Sacramento-San Joaquin Delta, California, USA Wetlands **29**:372-386.

Drexler, J. Z., C. S. De Fontaine, and D. L. Knifong. 2007. Age determination of the remaining peat in the Sacramento-San Joaquin Delta, California, USA. United States Geological Survey, Sacramento, CA.

Eugster, W., A. M. Moffat, E. Ceschia, M. Aubinet, C. Ammann, B. Osborne, P. A. Davis, P. Smith, C. Jacobs, E. Moors, V. Le Dantec, P. Beziat, M. Saunders, W. Jans, T. Gruenwald, C. Rebmann, W. L. Kutsch, R. Czerny, D. Janous, C. Moureaux, D. Dufranne, A. Carrara, V. Magliulo, P. Di Tommasi, J. E. Olesen, K. Schelde, A. Olioso, C. Bernhofer, P. Cellier, E. Larmanou, B. Loubet, M. Wattenbach, O. Marloie, M.-J. Sanz, H. Sogaard, and N. Buchmann. 2010. Management effects on European cropland respiration. Agriculture Ecosystems & Environment **139**:346-362.

Farrer, E. C. and D. E. Goldberg. 2009. Litter drives ecosystem and plant community changes in cattail invasion. Ecological Applications **19**:398-412.

Finnigan, J. 2000. Turbulence in plant canopies. Annual Review of Fluid Mechanics **32**:519-571.

Foley, J. A., R. DeFries, G. P. Asner, C. Barford, G. Bonan, S. R. Carpenter, F. S. Chapin, M. T. Coe, G. C. Daily, H. K. Gibbs, J. H. Helkowski, T. Holloway, E. A. Howard, C. J. Kucharik, C. Monfreda, J. A. Patz, I. C. Prentice, N. Ramankutty, and P. K. Snyder. 2005. Global consequences of land use. Science **309**:570-574.

Forster, P., V. Ramaswamy, P. Artaxo, T. Berntsen, R. A. Betts, D. W. Fahey, J. Haywood, J. Lean, D. C. Lowe, G. Myhre, J. Nganga, R. Prinn, G. Raga, M. Schulz, and R. Van Dorland. 2007. Changes in atmospheric constituents and in radiative forcing.*in* S. Solomon, D. Qin, M. Manning, Z. Chen, M. Marquis, K. B. Averyt, M. Tignor, and H. L. Miller, editors. Climate Change 2007: The Physical Science Basis. Contribution of Working Group I to the Fourth Assessment Report of the Intergovernmental Panel on Climate Change. Cambridge Univ. Press, New York.

Foti, R., M. del Jesus, A. Rinaldo, and I. Rodriguez-Iturbe. 2013. Signs of critical transition in the Everglades wetlands in response to climate and anthropogenic changes. Proceedings of the National Academy of Sciences **110**:6296-6300.

Gamon, J. A., C. Coburn, L. B. Flanagan, K. F. Huemmrich, C. Kiddle, G. A. Sanchez-Azofeifa, D. R. Thayer, L. Vescovo, D. Gianelle, D. A. Sims, A. F. Rahman, and G. Z. Pastorello. 2010. SpecNet revisited: bridging flux and remote sensing communities. Canadian Journal of Remote Sensing **36**:S376-S390.

Gamon, J. A., J. Penuelas, and C. B. Field. 1992. A narrow-waveband spectral index that tracks diurnal changes in photosynthetic efficiency Remote Sensing of Environment **41**:35-44.

Gamon, J. A., A. F. Rahman, J. L. Dungan, M. Schildhauer, and K. F. Huemmrich. 2006. Spectral Network (SpecNet) - What is it and why do we need it? Remote Sensing of Environment **103**:227-235.

Gamon, J. A., L. Serrano, and J. S. Surfus. 1997. The Photochemical Reflectance Index: An Optical Indicator of Photosynthetic Radiation Use Efficiency across Species, Functional Types, and Nutrient Levels. Oecologia **112**:492-501.

Geweke, J. 1982. Measurement of linear-dependence and feedback between multiple time-series. Journal of the American Statistical Association **77**:304-313.

Gilmanov, T. G., L. Aires, Z. Barcza, V. S. Baron, L. Belelli, J. Beringer, D. Billesbach, D. Bonal, J. Bradford, E. Ceschia, D. Cook, C. Corradi, A. Frank, D. Gianelle, C. Gimeno, T. Gruenwald, H. Guo, N. Hanan, L. Haszpra, J. Heilman, A. Jacobs, M. B. Jones, D. A. Johnson, G. Kiely, S. Li, V. Magliulo, E. Moors, Z. Nagy, M. Nasyrov, C. Owensby, K. Pinter, C. Pio, M. Reichstein, M. J. Sanz, R. Scott, J. F. Soussana, P. C. Stoy, T. Svejcar, Z. Tuba, and G. Zhou. 2010. Productivity, Respiration, and Light-Response Parameters of World Grassland and Agroecosystems Derived From Flux-Tower Measurements. Rangeland Ecology & Management **63**:16-39.

Goeckede, M., T. Foken, M. Aubinet, M. Aurela, J. Banza, C. Bernhofer, J. M. Bonnefond, Y. Brunet, A. Carrara, R. Clement, E. Dellwik, J. Elbers, W. Eugster, J. Fuhrer, A. Granier, T. Gruenwald, B. Heinesch, I. A. Janssens, A. Knohl, R. Koeble, T. Laurila, B. Longdoz, G. Manca, M. Marek, T. Markkanen, J. Mateus, G. Matteucci, M. Mauder, M. Migliavacca, S. Minerbi, J. Moncrieff, L. Montagnani, E. Moors, J. M. Ourcival, D. Papale, J. Pereira, K. Pilegaard, G. Pita, S. Rambal, C. Rebmann, A. Rodrigues, E. Rotenberg, M. J. Sanz, P. Sedlak, G. Seufert, L. Siebicke, J. F. Soussana, R. Valentini, T. Vesala, H. Verbeeck, and D. Yakir. 2008. Quality control of CarboEurope flux data - Part 1: Coupling footprint analyses with flux data quality assessment to evaluate sites in forest ecosystems. Biogeosciences **5**:433-450.

Goeckede, M., C. Rebmann, and T. Foken. 2004. A combination of quality assessment tools for eddy covariance measurements with footprint modelling for the characterisation of complex sites. Agricultural and Forest Meteorology **127**:175-188.

Goulden, M. L., M. Litvak, and S. D. Miller. 2007. Factors that control Typha marsh evapotranspiration. Aquatic Botany **86**:97-106.

Granger, C. W. J. 1969. Some recent development in a concept of causality. Journal of Econometrics **39**:199-211.

Grinsted, A., J. C. Moore, and S. Jevrejeva. 2004. Application of the cross wavelet transform and wavelet coherence to geophysical time series. Nonlinear Processes in Geophysics **11**:561-566.

Hagen, S. C., B. H. Braswell, E. Linder, S. Frolking, A. D. Richardson, and D. Y. Hollinger. 2006. Statistical uncertainty of eddy flux-based estimates of gross ecosystem carbon exchange at Howland Forest, Maine. Journal of Geophysical Research-Atmospheres **111**.

Han, G. H., H. Yoshikoshi, H. Nagai, T. Yamada, M. Saito, A. Miyata, and Y. Harazono. 2005. Concentration and carbon isotope profiles of CH4 in paddy rice canopy: Isotopic evidence for changes in CH4 emission pathways upon drainage. Chemical Geology **218**:25-40.

Hansen, P. M. and J. K. Schjoerring. 2003. Reflectance measurement of canopy biomass and nitrogen status in wheat crops using normalized difference vegetation indices and partial least squares regression. Remote Sensing of Environment **86**:542-553.

Harazono, Y., J. Kim, A. Miyata, T. Choi, J. I. Yun, and J. W. Kim. 1998. Measurement of energy budget components during the International Rice Experiment (IREX) in Japan. Hydrological Processes **12**:2081-2092.

Hatala, J. A., M. Detto, O. Sonnentag, S. J. Deverel, J. Verfaillie, and D. Baldocchi. 2012. Greenhouse gas (CO2, CH4, H2O) fluxes from drained and flooded agricultural peatlands in the Sacramento-San Joaquin Delta. Agriculture, Ecosystems & Environment **150**:1-18.

Hendriks, D. M. D., J. van Huissteden, and A. J. Dolman. 2010. Multi-technique assessment of spatial and temporal variability of methane fluxes in a peat meadow. Agricultural and Forest Meteorology **150**:757-774.

Hendriks, D. M. D., J. van Huissteden, A. J. Dolman, and M. K. van der Molen. 2007. The full greenhouse gas balance of an abandoned peat meadow. Biogeosciences **4**:411-424.

Herbst, M., T. Friborg, R. Ringgaard, and H. Soegaard. 2011. Interpreting the variations in atmospheric methane fluxes observed above a restored wetland. Agricultural and Forest Meteorology **151**:841-853.

Hlavackova-Schindler, K., M. Palus, M. Vejmelka, and J. Bhattacharya. 2007. Causality detection based on information-theoretic approaches in time series analysis. Physics Reports-Review Section of Physics Letters **441**:1-46.

Hoffman, G. J., E. V. Maas, T. L. Prichard, and J. L. Meyer. 1983. Salt tolerance of corn in the Sacramento-San Joaquin Delta of California. Irrigation Science **4**:31-44.

Holzapfel-Pschorn, A., R. Conrad, and W. Seiler. 1986. Effects of vegetation on the emission of methane from submerged paddy soil. Plant and Soil **92**:223-233.

Hosono, T. and I. Nouchi. 1997. The dependence of methane transport in rice plants on the root zone temperature. Plant and Soil **191**:233-240.

Hossain, M. and J. Narcisco. 2005. Global rice economy: Long-term perspectives.*in* A. Sarris, editor. Proceedings of the FAO Rice Conference 2004: Rice in global markets, Rome 12-13 February 2004. Food and Agriculture Organization of the United Nations, Rome, Italy.

Hsieh, C. I., G. Katul, and T. Chi. 2000. An approximate analytical model for footprint estimation of scaler fluxes in thermally stratified atmospheric flows. Advances in Water Resources **23**:765-772.

Huete, A. R., H. Q. Liu, K. Batchily, and W. van Leeuwen. 1997. A comparison of vegetation indices over a global set of TM images for EOS-MODIS. Remote Sensing of Environment **59**:440-451.

Huxman, T. E., K. A. Snyder, D. Tissue, A. J. Leffler, K. Ogle, W. T. Pockman, D. R. Sandquist, D. L. Potts, and S. Schwinning. 2004. Precipitation pulses and carbon fluxes in semiarid and arid ecosystems. Oecologia **141**:254-268.

Inoue, Y., J. Peñuelas, A. Miyata, and M. Mano. 2008. Normalized difference spectral indices for estimating photosynthetic efficiency and capacity at a canopy scale derived from hyperspectral and CO2 flux measurements in rice. Remote Sensing of Environment **112**:156-172.

Jans, W. W. P., C. M. J. Jacobs, B. Kruijt, J. A. Elbers, S. Barendse, and E. J. Moors. 2010. Carbon exchange of a maize (Zea mays L.) crop: Influence of phenology. Agriculture, Ecosystems & Environment **139**:316-324.

Jauhiainen, J., S. Limin, H. Silvennoinen, and H. Vasander. 2008. Carbon dioxide and methane fluxes in drained tropical peat before and after hydrological restoration. Ecology **89**:3503-3514.

Jiang, Z., A. R. Huete, K. Didan, and T. Miura. 2008. Development of a two-band enhanced vegetation index without a blue band. Remote Sensing of Environment **112**:3833-3845.

Jonckheere, I., K. Nackaerts, B. Muys, J. van Aardt, and P. Coppin. 2006. A fractal dimension-based modelling approach for studying the effect of leaf distribution on LAI retrieval in forest canopies. Ecological Modelling **197**:179-195.

Kaimal, J. C. and J. E. Gaynor. 1991. Another look at sonic thermometry. Boundary-Layer Meteorology **56**:401-410.

Katul, G., C. T. Lai, K. Schafer, B. Vidakovic, J. Albertson, D. Ellsworth, and R. Oren. 2001. Multiscale analysis of vegetation surface fluxes: from seconds to years. Advances in Water Resources **24**:1119-1132.

Kimura, M., J. Murase, and Y. H. Lu. 2004. Carbon cycling in rice field ecosystems in the context of input, decomposition and translocation of organic materials and the fates of their end products (CO2 and CH4). Soil Biology & Biochemistry **36**:1399-1416.

King, R. S., C. J. Richardson, D. L. Urban, and E. A. Romanowicz. 2004. Spatial Dependency of Vegetation–Environment Linkages in an Anthropogenically Influenced Wetland Ecosystem. Ecosystems **7**:75-97.

Knyazikhin, Y., J. V. Martonchik, R. B. Myneni, D. J. Diner, and S. W. Running. 1998. Synergistic algorithm for estimating vegetation canopy leaf area index and fraction of absorbed photosynthetically active radiation from MODIS and MISR data. Journal of Geophysical Research-Atmospheres **103**:32257-32275.

Knyazikhin, Y., M. A. Schull, P. Stenberg, M. Mõttus, M. Rautiainen, Y. Yang, A. Marshak, P. Latorre Carmona, R. K. Kaufmann, P. Lewis, M. I. Disney, V. Vanderbilt, A. B. Davis, F. Baret, S. Jacquemoud, A. Lyapustin, and R. B. Myneni. 2013. Hyperspectral remote sensing of foliar nitrogen content. Proceedings of the National Academy of Sciences **110**:E185–E192.

Kochendorfer, J., E. G. Castillo, E. Haas, W. C. Oechel, and K. T. Paw U. 2011. Net ecosystem exchange, evapotranspiration and canopy conductance in a riparian forest. Agricultural and Forest Meteorology **151**:544-553.

Kokaly, R. F. 2001. Investigating a physical basis for spectroscopic estimates of leaf nitrogen concentration. Remote Sensing of Environment **75**:153-161.

Kriegler, F. J., W. A. Malila, R. F. Nalepka, and W. Richardson. 1969. Preprocessing transformations and their effects on multispectral recognition. Proceedings of the Sixth International Symposium on Remote Sensing of Environment:97-131.

Kruger, M., P. Frenzel, and R. Conrad. 2001. Microbial processes influencing methane emission from rice fields. Global Change Biology **7**:49-63.

Krummel, J. R., R. H. Gardner, G. Sugihara, R. V. Oneill, and P. R. Coleman. 1987. Landscape patterns in a disturbed environment Oikos **48**:321-324.

Kuzyakov, Y., J. K. Friedel, and K. Stahr. 2000. Review of mechanisms and quantification of priming effects. Soil Biology & Biochemistry **32**:1485-1498.

Laanbroek, H. J. 2009. Methane emission from natural wetlands: interplay between emergent macrophytes and soil microbial processes. A mini-review. Annals of Botany **105**:141-153.

Li, C. 2005. Modeling impacts of farming management alternatives on CO2, CH4, and N2O emissions: A case study for water management of rice agriculture of China. Global Biogeochemical Cycles **19**.

Liu, H. Q. and A. Huete. 1995. A feedback based modification of the NDVI to minimize canopy background and atmospheric noise. Ieee Transactions on Geoscience and Remote Sensing **33**:814-814.

Lloyd, J. and J. A. Taylor. 1994. On the temperature-dependence of soil respiration. Functional Ecology **8**:315-323.

Lourence, F. J. and W. O. Pruitt. 1971. Energy balance and water use of rice grown in the Central Valley of California. Agronomy Journal **63**:827-&.

Lund, J., E. Hanak, W. Fleenor, R. Howitt, J. Mount, and P. Moyle. 2007. Envisioning futures for the Sacramento-San Joaquin Delta. Public Policy Institute of California, San Francisco, CA.

Ma, S. Y., D. D. Baldocchi, L. K. Xu, and T. Hehn. 2007. Inter-annual variability in carbon dioxide exchange of an oak/grass savanna and open grassland in California. Agricultural and Forest Meteorology **147**:157-171.

Mandelbrot, B. 1983. The Fractal Geometry of Nature. W. H. Freeman and Company, New York, NY.

Martin, M. E., L. C. Plourde, S. V. Ollinger, M. L. Smith, and B. E. McNeil. 2008. A generalizable method for remote sensing of canopy nitrogen across a wide range of forest ecosystems. Remote Sensing of Environment **112**:3511-3519.

Masani. 1966. Recent trends in multivariate prediction theory. Pages 351-382 *in* P. R. Kirishnaiah, editor. Multivariate Analysis. Academic Press, New York.

Massman, W. J. and X. Lee. 2002. Eddy covariance flux corrections and uncertainties in long-term studies of carbon and energy exchanges. Agricultural and Forest Meteorology **113**:121-144.

McDermitt, D., G. Burba, L. Xu, T. Anderson, A. Komissarov, B. Riensche, J. Schedlbauer, G. Starr, D. Zona, W. Oechel, S. Oberbauer, and S. Hastings. 2010. A new low-power, open-path instrument for measuring methane flux by eddy covariance. Applied Physics B **102**:391-405.

McMillan, A. M. S., M. L. Goulden, and S. C. Tyler. 2007. Stoichiometry of CH4 and CO2 flux in a California rice paddy. J. Geophys. Res. **112**:G01008.

Megonigal, J. P., M. E. Hines, and P. T. Visscher. 2003. Anaerobic metabolism: Linkages to trace gases and aerobic processes. Pages 319-424 *in* W. H. Schlesinger, editor. Biogeochemistry. Elsevier, New York, NY.

Miller, R. L., M. Fram, R. Fujii, and G. Wheeler. 2008. Subsidence reversal in a re-established wetland in the Sacramento-San Joaquin Delta, California, USA. San Francisco Estuary and Watershed Science **6**.

Miller, R. L. and R. Fujii. 2010. Plant community, primary productivity, and environmental conditions following wetland re-establishment in the Sacramento-San Joaquin Delta, California. Wetlands Ecology and Management **18**:1-16.

Miller, R. L., L. Hastings, and R. Fujii. 2000. Hydrologic treatments affect gaseous carbon loss from organic soils, Twitchell Island, California, October 1995 - December 1997. U. S. Geological Survey Water Resources Investigations Report 00-4042.

Milne, B. T. 1992. Spatial aggregation and neutral models in fractal landscapes. American Naturalist **139**:32-57.

Minoda, T. and M. Kimura. 1994. Contribution of photosynthesized carbon to the methane emitted from paddy fields. Geophysical Research Letters **21**:2007-2010.

Minoda, T., M. Kimura, and E. Wada. 1996. Photosynthates as dominant source of CH4 and CO2 in soil water and CH4 emitted to the atmosphere from paddy fields. Journal of Geophysical Research-Atmospheres **101**:21091-21097.

Miyata, A., R. Leuning, O. T. Denmead, J. Kim, and Y. Harazono. 2000. Carbon dioxide and methane fluxes from an intermittently flooded paddy field. Agricultural and Forest Meteorology **102**:287-303.

Molini, A., G. G. Katul, and A. Porporato. 2010. Causality across rainfall time scales revealed by continuous wavelet transforms. Journal of Geophysical Research-Atmospheres **115**.

Montero, E. 2005. Renyi dimensions analysis of soil particle-size distributions. Ecological Modelling **182**:305-315.

Moorcroft, P. R., G. C. Hurtt, and S. W. Pacala. 2001. A method for scaling vegetation dynamics: The ecosystem demography model (ED). Ecological Monographs **71**:557-585.

Mount, J. and R. Twiss. 2005. Subsidence, sea level rise, and seismicity in the Sacramento-San Joaquin Delta. San Francisco Estuary & Watershed Science **3**:Article 5.

Myneni, R. B., S. Hoffman, Y. Knyazikhin, J. L. Privette, J. Glassy, Y. Tian, Y. Wang, X. Song, Y. Zhang, G. R. Smith, A. Lotsch, M. Friedl, J. T. Morisette, P. Votava, R. R. Nemani, and S. W. Running. 2002. Global products of vegetation leaf area and fraction absorbed PAR from year one of MODIS data. Remote Sensing of Environment **83**:214-231.

Neubauer, S. C., K. Givler, S. K. Valentine, and J. P. Megonigal. 2005. Seasonal patterns and plant-mediated controls of subsurface wetland biogeochemistry. Ecology **86**:3334-3344.

Nieveen, J. P., D. I. Campbell, L. A. Schipper, and I. J. Blair. 2005. Carbon exchange of grazed pasture on a drained peat soil. Global Change Biology **11**:607-618.

Nouchi, I., S. Mariko, and K. Aoki. 1990. Mechanism of methane transport from the rhizosphere to the atmosphere through rice plants. Plant Physiology **94**:59-66.

Ollinger, S. V., A. D. Richardson, M. E. Martin, D. Y. Hollinger, S. E. Frolking, P. B. Reich, L. C. Plourde, G. G. Katul, J. W. Munger, R. Oren, M.-L. Smith, K. T. Paw U, P. V. Bolstad, B. D. Cook, M. C. Day, T. A. Martin, R. K. Monson, and H. P. Schmid. 2008. Canopy nitrogen, carbon assimilation, and albedo in temperate and boreal forests: Functional relations and potential climate feedbacks. Proceedings of the National Academy of Sciences **105**:19336-19341.

Papale, D., M. Reichstein, M. Aubinet, E. Canfora, C. Bernhofer, W. Kutsch, B. Longdoz, S. Rambal, R. Valentini, T. Vesala, and D. Yakir. 2006. Towards a standardized processing of Net Ecosystem Exchange measured with eddy covariance technique: algorithms and uncertainty estimation. Biogeosciences **3**:571-583.

Papale, D. and A. Valentini. 2003. A new assessment of European forests carbon exchanges by eddy fluxes and artificial neural network spatialization. Global Change Biology **9**:525-535.

Parmentier, F. J. W., J. van Huissteden, M. K. van der Molen, G. Schaepman-Strub, S. A. Karsanaev, T. C. Maximov, and A. J. Dolman. 2012. Spatial and temporal dynamics in eddy covariance observations of methane fluxes at a tundra site in northeastern Siberia (vol 116, G03016, 2011). Journal of Geophysical Research-Biogeosciences **117**.

Penman, H. L. 1948. Natural evaporation from open water, bare soil and grass. Proceedings of the Royal Society of London Series a-Mathematical and Physical Sciences **193**:120-&.

Pielke, R. A., G. Marland, R. A. Betts, T. N. Chase, J. L. Eastman, J. O. Niles, D. D. S. Niyogi, and S. W. Running. 2002. The influence of land-use change and landscape dynamics on the climate system: relevance to climate-change policy beyond the radiative effect of greenhouse gases. Philosophical Transactions of the Royal Society of London Series a-Mathematical Physical and Engineering Sciences **360**:1705-1719.

Pruitt, W. O., F. J. Lourence, and Oettinge.Sv. 1972. Water use by crops as affected by climate and plant factors. California Agriculture **26**:10-&.

Ramankutty, N., A. T. Evan, C. Monfreda, and J. A. Foley. 2008. Farming the planet: 1. Geographic distribution of global agricultural lands in the year 2000. Global Biogeochem. Cycles **22**:GB1003.

Reichstein, M., E. Falge, D. Baldocchi, D. Papale, M. Aubinet, P. Berbigier, C. Bernhofer, N. Buchmann, T. Gilmanov, A. Granier, T. Grunwald, K. Havrankova, H. Ilvesniemi, D. Janous, A. Knohl, T. Laurila, A. Lohila, D. Loustau, G. Matteucci, T. Meyers, F. Miglietta, J. M. Ourcival, J. Pumpanen, S. Rambal, E. Rotenberg, M. Sanz, J. Tenhunen, G. Seufert, F. Vaccari, T. Vesala, D. Yakir, and R. Valentini. 2005. On the separation of net ecosystem exchange into assimilation and ecosystem respiration: review and improved algorithm. Global Change Biology **11**:1424-1439.

Rocha, A. V. and M. L. Goulden. 2008. Large interannual CO(2) and energy exchange variability in a freshwater marsh under consistent environmental conditions. Journal of Geophysical Research-Biogeosciences **113**.

Rocha, A. V. and M. L. Goulden. 2009. Why is marsh productivity so high? New insights from eddy covariance and biomass measurements in a Typha marsh. Agricultural and Forest Meteorology **149**:159-168.

Rocha, A. V. and G. R. Shaver. 2009. Advantages of a two band EVI calculated from solar and photosynthetically active radiation fluxes. Agricultural and Forest Meteorology **149**:1560-1563.

Rock, B. N., T. Hoshizaki, and J. R. Miller. 1988. Comparison of in situ and airborne spectral measurements of the blue shift associated with forest decline. Remote Sensing of Environment **24**:109-127.

Rojstaczer, S. and S. J. Deverel. 1993. Time-dependence in atmospheric carbon inputs from drainage of organic soils. Geophysical Research Letters **20**:1383-1386.

Rojstaczer, S. and S. J. Deverel. 1995. Land subsidence in drained histosols and highly organic mineral soils of California. Soil Science Society of America Journal **59**:1162-1167.

Rouse, J. W., R. H. Haas, J. A. Schell, and D. W. Deering. 1973. Monitoring vegetation systems in the Great Plains with ERTS. Pages 309-317 *in* 3rd ERTS Symposium. NASA SP-351 I.

Runkle, B. R. K. 2009. Plant water use and growth in response to soil salinity in irrigated agriculture. University of California - Berkeley, Berkeley, CA.

Running, S. W., D. D. Baldocchi, D. P. Turner, S. T. Gower, P. S. Bakwin, and K. A. Hibbard. 1999. A global terrestrial monitoring network integrating tower fluxes,

flask sampling, ecosystem modeling and EOS satellite data. Remote Sensing of Environment **70**:108-127.

Ryu, Y., D. D. Baldocchi, S. Ma, and T. Hehn. 2008. Interannual variability of evapotranspiration and energy exchange over an annual grassland in California. Journal of Geophysical Research-Atmospheres **113**.

Ryu, Y., D. D. Baldocchi, J. Verfaillie, S. Ma, M. Falk, I. Ruiz-Mercado, T. Hehn, and O. Sonnentag. 2010a. Testing the performance of a novel spectral reflectance sensor, built with light emitting diodes (LEDs), to monitor ecosystem metabolism, structure and function. Agricultural and Forest Meteorology **150**:1597-1606.

Ryu, Y., T. Nilson, H. Kobayashi, O. Sonnentag, B. E. Law, and D. D. Baldocchi. 2010b. On the correct estimation of effective leaf area index: Does it reveal information on clumping effects? Agricultural and Forest Meteorology **150**:463-472.

Saito, M., A. Miyata, H. Nagai, and T. Yamada. 2005. Seasonal variation of carbon dioxide exchange in rice paddy field in Japan. Agricultural and Forest Meteorology **135**:93-109.

Sass, R. L., J. A. Andrews, A. Ding, and F. M. Fisher. 2002. Spatial and temporal variability in methane emissions from rice paddies: Implications for assessing regional methane budgets. Nutrient Cycling in Agroecosystems **64**:3-7.

Schimel, J. P. 1995. Plant transport and methane production as controls on methane flux from Arctic wet meadow tundra. Biogeochemistry **28**:183-200.

Schotanus, P., F. T. M. Nieuwstadt, and H. A. R. Debruin. 1983. Temperature measurement with a sonic anemometer and its application to heat and moisture fluxes. Boundary-Layer Meteorology **26**:81-93.

Schrier-Uijl, A. P., P. S. Kroon, A. Hensen, P. A. Leffelaar, F. Berendse, and E. M. Veenendaal. 2010. Comparison of chamber and eddy covariance-based CO2 and CH4 emission estimates in a heterogeneous grass ecosystem on peat. Agricultural and Forest Meteorology **150**:825-831.

Schutz, H., A. Holzapfelpschorn, R. Conrad, H. Rennenberg, and W. Seiler. 1989a. A 3-year continuous record on the influence of daytime, season, and fertilizer treatment on methane emission rates from an Italian rice paddy. Journal of Geophysical Research-Atmospheres **94**:16405-16416.

Schutz, H., W. Seiler, and R. Conrad. 1989b. Processes involved in formation and emission of methane in rice paddies. Biogeochemistry **7**:33-53.

Schwarzenegger, A., P. Isenberg, M. Florian, R. Frank, T. McKernan, S. McPeak, W. Reilly, R. Seed. 2008. Delta Vision Strategic Plan. State of California Resources Agency, Sacramento.

Shaw, S. L., F. M. Mitloehner, W. Jackson, E. J. Depeters, J. G. Fadel, P. H. Robinson, R. Holzinger, and A. H. Goldstein. 2007. Volatile organic compound emissions from dairy cows and their waste as measured by proton-transfer-reaction mass spectrometry. Environmental Science & Technology **41**:1310-1316.

Shlemon, R. J. and E. L. Begg. 1975. Late Quaternary evolution of the Sacramento-San Joaquin Delta, California. Quaternary Studies **13**:259-266.

Shuttleworth, W. J. 2007. Putting the 'vap' into evaporation. Hydrology and Earth System Sciences **11**:210-244.

Smith, M.-L., S. V. Ollinger, M. E. Martin, J. D. Aber, R. A. Hallett, and C. L. Goodale. 2002. Direct estimation of aboveground forest productivity through hyperspectral remote sensing of canopy nitrogen. Ecological Applications **12**:1286-1302.

Smith, P., D. Martino, Z. Cai, D. Gwary, H. Janzen, P. Kumar, B. McCarl, S. Ogle, F. O'Mara, C. Rice, B. Scholes, and O. Sirotenko. 2007. Agriculture.*in* B. Metz, O. R. Davidson, P. R. Bosch, R. Dave, and L. A. Meyer, editors. Climate Change 2007: Mitigation. Contribution of Working Group III to the Fourth Assessment Report of the Intergovernmental Panel on Climate Change. Cambridge University Press, Cambridge, UK and New York, NY.

Sonnentag, O., M. Detto, B. R. K. Runkle, Y. A. Teh, W. L. Silver, M. Kelly, and D. D. Baldocchi. 2011a. Carbon dioxide exchange of a pepperweed (Lepidium latifoliumL.) infestation: How do flowering and mowing affect canopy photosynthesis and autotrophic respiration? Journal of Geophysical Research **116**.

Sonnentag, O., M. Detto, R. Vargas, Y. Ryu, B. R. K. Runkle, M. Kelly, and D. D. Baldocchi. 2011b. Tracking the structural and functional development of a perennial pepperweed (Lepidium latifolium L.) infestation using a multi-year archive of webcam imagery and eddy covariance measurements. Agricultural and Forest Meteorology **151**:916-926.

Soussana, J. F., V. Allard, K. Pilegaard, P. Ambus, C. Amman, C. Campbell, E. Ceschia, J. Clifton-Brown, S. Czobel, R. Domingues, C. Flechard, J. Fuhrer, A. Hensen, L. Horvath, M. Jones, G. Kasper, C. Martin, Z. Nagy, A. Neftel, A. Raschi, S. Baronti, R. M. Rees, U. Skiba, P. Stefani, G. Manca, M. Sutton, Z. Tubaf, and R. Valentini. 2007. Full accounting of the greenhouse gas (CO2, N2O, CH4) budget of nine European grassland sites. Agriculture Ecosystems & Environment **121**:121-134.

Syvitski, J. P. M., A. J. Kettner, I. Overeem, E. W. H. Hutton, M. T. Hannon, G. R. Brakenridge, J. Day, C. Vorosmarty, Y. Saito, L. Giosan, and R. J. Nicholls. 2009. Sinking deltas due to human activities. Nature Geoscience **2**:681-686.

Teh, Y. A., W. L. Silver, and M. E. Conrad. 2005. Oxygen effects on methane production and oxidation in humid tropical forest soils. Global Change Biology **11**:1283-1297.

Teh, Y. A., W. L. Silver, O. Sonnentag, M. Detto, M. Kelly, and D. D. Baldocchi. 2011. Large Greenhouse Gas Emissions from a Temperate Peatland Pasture. Ecosystems **14**:311-325.

Tews, J., U. Brose, V. Grimm, K. Tielbörger, M. C. Wichmann, M. Schwager, and F. Jeltsch. 2004. Animal species diversity driven by habitat heterogeneity/diversity: the importance of keystone structures. Journal of Biogeography **31**:79-92.

Thompson, J. 1957. The settlement geography of the Sacramento-San Joaquin Delta, California. Stanford University, Palo Alto.

Tian, Y. C., X. Yao, J. Yang, W. X. Cao, D. B. Hannaway, and Y. Zhu. 2011. Assessing newly developed and published vegetation indices for estimating rice leaf nitrogen concentration with ground- and space-based hyperspectral reflectance. Field Crops Research **120**:299-310.

Torrence, C. and G. P. Compo. 1998. A practical guide to wavelet analysis. Bulletin of the American Meteorological Society **79**:61-78.

Tyler, S. C., R. S. Bilek, R. L. Sass, and F. M. Fisher. 1997. Methane oxidation and pathways of production in a Texas paddy field deduced from measurements of flux, delta C-13, and delta D of CH4. Global Biogeochemical Cycles **11**:323-348.

Uchijima, Z. 1976. Maize and Rice.*in* J. Monteith, editor. Vegetation and the Atmosphere. Academic Press Inc., New York, NY.

Ustin, S. L., D. A. Roberts, J. A. Gamon, G. P. Asner, and R. O. Green. 2004. Using Imaging Spectroscopy to Study Ecosystem Processes and Properties. Bioscience **54**:523-534.

van Noordwijk, M. and R. Mulia. 2002. Functional branch analysis as tool for fractal scaling above- and belowground trees for their additive and non-additive properties. Ecological Modelling **149**:41-51.

Varadharajan, C., R. Hermosillo, and H. F. Hemond. 2010. A low-cost automated trap to measure bubbling gas fluxes. Limnology and Oceanography-Methods **8**:363-375.

Vargas, R., M. Detto, D. D. Baldocchi, and M. F. Allen. 2010. Multiscale analysis of temporal variability of soil CO(2) production as influenced by weather and vegetation. Global Change Biology **16**:1589-1605.

Waddington, J. M., M. Strack, and M. J. Greenwood. 2010. Toward restoring the net carbon sink function of degraded peatlands: Short-term response in CO2 exchange to ecosystem-scale restoration. Journal of Geophysical Research-Biogeosciences **115**.

Walter, K. M., J. P. Chanton, F. S. Chapin, E. A. G. Schuur, and S. A. Zimov. 2008. Methane production and bubble emissions from arctic lakes: Isotopic implications for source pathways and ages. Journal of Geophysical Research-Biogeosciences **113**.

Webb, E. K., G. I. Pearman, and R. Leuning. 1980. Correction of flux measurements for density effects due to heat and water-vapor transfer. Quarterly Journal of the Royal Meteorological Society **106**:85-100.

Weir, W. W. 1950. Subsidence of peat lands of the Sacramento-San Joaquin Delta, California. Hilgardia **20**:37-56.

Whiting, G. J. and J. P. Chanton. 1993. Primary production control of methane emission from wetlands. Nature **364**:794-795.

Wilson, G. T. 1972. Factorization of matrical spectral densities. Siam Journal on Applied Mathematics **23**:420-426.

Wilson, K., A. Goldstein, E. Falge, M. Aubinet, D. Baldocchi, P. Berbigier, C. Bernhofer, R. Ceulemans, H. Dolman, C. Field, A. Grelle, A. Ibrom, B. E. Law, A. Kowalski, T. Meyers, J. Moncrieff, R. Monson, W. Oechel, J. Tenhunen, R. Valentini, and S.

Verma. 2002. Energy balance closure at FLUXNET sites. Agricultural and Forest Meteorology **113**:223-243.

With, K. A., R. H. Gardner, and M. G. Turner. 1997. Landscape connectivity and population distributions in heterogeneous environments. Oikos **78**:151-169.

Worrall, F., M. J. Bell, and A. Bhogal. 2010. Assessing the probability of carbon and greenhouse gas benefit from the management of peat soils. Science of the Total Environment **408**:2657-2666.

Xiao, X. M., Q. Y. Zhang, D. Hollinger, J. Aber, and B. Moore. 2005. Modeling gross primary production of an evergreen needleleaf forest using modis and climate data. Ecological Applications **15**:954-969.

Xu, L. K., D. D. Baldocchi, and J. W. Tang. 2004. How soil moisture, rain pulses, and growth alter the response of ecosystem respiration to temperature. Global Biogeochemical Cycles **18**.

Yavitt, J. B. and A. K. Knapp. 1995. Methane emission to the atmosphere through emergent cattail (Typha latifolia L) plants Tellus Series B-Chemical and Physical Meteorology **47**:521-534.

Zhao, D., K. Raja Reddy, V. G. Kakani, J. J. Read, and G. A. Carter. 2003. Corn (Zea mays L.) growth, leaf pigment concentration, photosynthesis and leaf hyperspectral reflectance properties as affected by nitrogen supply. Plant and Soil **257**:205-218.

Zhao, D., K. R. Reddy, V. G. Kakani, and V. R. Reddy. 2005. Nitrogen deficiency effects on plant growth, leaf photosynthesis, and hyperspectral reflectance properties of sorghum. European Journal of Agronomy **22**:391-403.